SOME PHENOMENA PRODUCED BY POSITIVE ION BOMBARDMENT OF METAL SURFACES AT MEDIUM ENERGIES

A thesis presented for the
Degree of Doctor of Philosophy

by

E.R. CAWTHRON

Research School of Physical Sciences
The Australian National University
Canberra, A.C.T.
Australia

December, 1969

ACKNOWLEDGEMENTS

This thesis describes some aspects of the experimental work carried out by the Physics of Ionized Gases Unit at the Research School of Physical Sciences, Australian National University, during its lifetime, 1965 - 1969. During this period the author worked as a member of a fairly closely knit team comprising Emeritus Professor Sir Mark Oliphant, K.B.E., F.R.S., as Head of the Unit, Mr. D.L. Cotterell as Senior Technical Officer and himself as Research Assistant.

Generally speaking, Sir Mark Oliphant was responsible for most of the detailed design work for the experimental apparatus, Mr. Cotterell for the construction and maintenance of the latter, and the author for the actual taking of the scientific data and the control of the experimental apparatus while in operation. However, such division is only a rough guide, as the Unit at all times functioned as a team with its members sharing responsibilities and discussing and exchanging ideas at every opportunity.

Much of the interpretation of the experimental data given in this thesis is the author's own and Sir Mark Oliphant may not necessarily be in agreement with all of it. However, the writer is indebted to Sir Mark Oliphant for many hours of detailed and profitable discussion during the preparation of this thesis.

Summing up, then, the author wishes to express his deep gratitude to Sir Mark Oliphant and to Mr. Cotterell for several years of very enjoyable and profitable team work, and he hopes that they will regard this thesis, in part, as a culmination of their own labours. The author also wishes to thank the Unit Secretary, Miss M. Mackie, for typing this thesis and for arranging the numerous diagrams in an ordered and presentable manner.

INTRODUCTION

The last decade and a half has witnessed an enormous growth in the field of experimental atomic physics after a period of comparative neglect from 1935 to 1955. The slowing down of research in the field over this period can be partly attributed to the concentration on the more glamorous field of nuclear physics, with its greater apparent technological and commercial dividends. The mounting cost of nuclear research, however, led many research groups to re-direct some attention to the lower (and consequently cheaper) energy range below 500 keV, where atomic, rather than nuclear, processes become physically significant in many inter-particle reactions. It was quickly realized that an understanding of atomic interactions was a necessity for explaining many natural terrestrial phenomena such as atmospheric discharges and ionization, and also for the understanding - if only in a qualitative sense - of secondary emission processes, plasma generation and confinement, etc.

Atomic phenomena are often categorized as collective or non-collective, the former involving the simultaneous interaction of many particles, whereas the latter involves a small finite number, usually two. However, the interaction of electrons or ions with metal surfaces cannot be unambiguously placed in either category and this lack of a well defined physical interpretation largely accounts for the generally poor state of theory in dealing with these phenomena. This contrasts with the relatively well developed theories of binary gas collisions (purely non-collective) and plasma physics (purely collective). During the course of this dissertation the experimental observations will be used to indicate the probable physical processes involved and some simple theoretical models discussed in the light of such results.

When a beam of particles collides with a solid surface, a variety of physical phenomena may occur, depending on the energy of the incident particles, their nature, and on the nature and condition of the surface. In the 5 - 50 keV

energy range these phenomena include scattering of the incident particles, sputtering of the target atoms, channelling into the target lattice and the emission of electrons and photons through several possible processes. The interactions may involve also changes in both energy and charge state. It is the task of the experimentalist to unambiguously:

(a) Separate the various secondary processes from each other.

(b) Investigate the individual secondary processes.

Unfortunately much of the published data up to very recently does not conform to one or both of these requirements.

The present work deals with the emission or scattering of particles, ions, atoms and electrons from polycrystalline and semicrystalline surfaces under ion bombardment in the 5 - 50 keV range. Parameters investigated include total emissions, 'real' and 'apparent' of these particles and their charge and energy distributions for various ion target combinations. Reference is also made to current measurements being made in these laboratories of the angular distributions of the scattered particles. For convenience the presentation and discussion of results for electrons and ions will be separated.

E. R. Cawthron.

CONTENTS

	Page No.
ACKNOWLEDGEMENTS ...	i
INTRODUCTION ...	ii
CHAPTER I	
THEORETICAL BASIS FOR EXPERIMENTAL WORK	
1-1 Energy Losses and Scattering of Ions in Solids ...	1
1-2 Discussion of Interaction Between Ions and Solids from the Point of View of Interpretation of Experimental Data ...	7
A. Scattering of light ions (protons) by solid media ...	7
B. Scattering of heavy ions (argon ions) by solid media ...	15
1-3 The Sputtering of Solid Media by Ions ...	19
1-4 Secondary (Kinetic) Emission of Electrons from Solid Media under Ion Bombardment ...	22
1-5 Conclusion ...	28
CHAPTER II	
MEASUREMENTS OF TOTAL SCATTERING OF IONS AND EMISSION OF ELECTRONS	
2-1 Preliminary Observations ...	29
A. Experimental arrangement and discussion ...	29
B. Preliminary observations made on the apparent secondary electron coefficient, γ' ...	35
C. Preliminary observations made on the ion scattering coefficient, R ...	47
2-2 Systematic Observations on the Emission Coefficients ...	55
A. Apparatus for measuring the real secondary electron coefficient, γ ...	55
B. Results for systematic measurements on the secondary emission coefficient, γ ...	58
C. Results for systematic measurements on the apparent ion scattering coefficient, R ...	72
CHAPTER III	
ENERGY DISTRIBUTION MEASUREMENTS I: ANALYSING SYSTEM AND ENERGY SPECTRA FOR ELECTRONS	
3-1 Energy Analysing System ...	82
A. Description ...	82
B. Testing of analyser ...	84

Page No.

3-2 Experimental Results on Electron Energy Distributions ... 87

CHAPTER IV

ENERGY DISTRIBUTION MEASUREMENTS II: ENERGY SPECTRA FOR POSITIVE AND NEGATIVE SCATTERED IONS

4-1 Experimental Considerations ... 96

4-2 The Spectra of Light Ions. Experimental Results and Discussion ... 99

4-3 The Spectra of Heavy Ions ... 119

A. Results ... 119

B. Discussion ... 125

APPENDIX I

ASPECTS OF THE APPARATUS

A. Beam Generation and Focussing ... 136

B. The Vacuum System ... 143

APPENDIX II

ANGULAR MEASUREMENTS OF ELECTRON AND ION EMISSION

A. The Dependence of the Total Emission Coefficients, γ' and R upon the Angle of Incidence ... 148

B. Variation in the Shape of the Energy Distributions of Scattered Ions with the Angle of Incidence and the Angle of Scattering ... 151

C. The Angular Distributions of Secondary Electrons ... 157

APPENDIX III

CALIBRATION FACTOR OF SPHERICAL ANALYSER EMPLOYED IN CHAPTERS III AND IV ... 159

REFERENCES ... 161

CHAPTER I

THEORETICAL BASIS FOR EXPERIMENTAL WORK

1-1 Energy Losses and Scattering of Ions in Solids

When an atom of mass M strikes an electron, then the maximum transferred energy is:

$$T_m = \frac{4Mm_e}{(M + m_e)^2} E_o \simeq \frac{4m_e}{M} E_o , \tag{1.1}$$

where E_o is the incident particle energy and m_e is the electronic mass.

Thus the energy transfer is much less efficient than when the masses are equal for then $T_m = E_o$.

The transfer of the energy to the outer electrons of an atom will only excite them if $T_m \sim E_{excitation}$, where $E_{excitation}$ is the energy sufficient to excite them to higher levels in the struck atom. Thus, as $E_{excitation}$ is of the order of several electron volts, excitation occurs when

$$E_o \gtrsim \frac{M}{m_e} eV \simeq 2A \text{ keV}, \tag{1.2}$$

where A is the atomic mass number of the incident ion. Thus a hydrogen atom need only have an energy of 1 keV to excite electrons to higher levels in the atom, while argon atoms must have energies of the order of 40 keV.

We can approach this phenomenon alternatively by noting that the kinetic energy of an outer electron in an atom is of the order of the ionization energy for removal of the electrons, i.e., for ionization under impact by atoms with mass M, we can write:

$$T_m = \frac{4m_e}{M} E_o \sim E_{ionization} \sim \frac{1}{2} m_e v_e^2 , \tag{1.3}$$

where v_e is the orbital electron velocity. Writing $E_o = \frac{1}{2} Mv_o^2$, where v_o is the incident particle velocity, this gives, at the threshhold for ionization,

$$v_e \sim 2v_o . \tag{1.4}$$

Such direct ionization processes in general, will be negligible when

$$\frac{v_o}{v_e} \lesssim \frac{1}{2} \quad \text{or} \quad E_o < 3\frac{M}{m_e}\ \text{eV} \sim 6A\ \text{keV}\,, \tag{1.5}$$

(taking the energy of an electron of velocity v_e to be 13.5 eV). This is very similar to the criterion above for excitation, the other inelastic process.

Bohr[1] assumed that for $v_o \sim v_e$ we can consider the collisions between the ions and electrons to be free and uninfluenced by the electron binding forces: then the maximum energy transfer to an electron is exactly T_m. He assumed that excitation of the electrons only becomes negligible when:

$$\frac{v_o}{v_e} \lesssim \frac{1}{20} \quad \text{or} \quad E_o < 0.03\frac{M}{m_e}\ \text{eV} \sim 0.06A\ \text{keV}\,. \tag{1.6}$$

The energy threshold is thus only 1% of that calculated above for the bound electron.

A more realistic criterion to accept is that of Seitz[2] whose analysis shows that ionization becomes unimportant when:

$$E_o \lesssim E_c = \frac{1}{16}\frac{M}{m_e} W_i \qquad \text{for metals}\,, \tag{1.7}$$

$$E_o \lesssim \frac{1}{8}\frac{M}{m_e} E_g \qquad \text{for insulators}\,, \tag{1.8}$$

where W_i and E_g are respectively the fermi energy of the free electrons in the metal and the optical width of the forbidden gap in the insulator. Seitz considered the higher bound states for which the ionization energy E_i will be lower than for the innermost electrons: for Cu (1.7) gives:

$$E_o \lesssim \frac{1}{2}\frac{M}{m_e}\ \text{eV} \sim A\ \text{keV}\,, \tag{1.9}$$

and for Ag

$$E_o \lesssim \frac{1}{3}\frac{M}{m_e}\ \text{eV} \sim \frac{2}{3}A\ \text{keV}\,. \tag{1.10}$$

Thus his results are similar to those obtained by the simple analysis given previously. This is considerably greater than the Bohr criterion (1.6) for all metals.

While Bohr's criterion predicts that inelastic energy losses predominate down to much lower energies than predicted by Seitz's criterion, both involve a rather arbitrary threshhold below which inelastic losses are assumed negligible and each predicts that this increases linearly with mass number A. Seitz's criterion takes into account electron binding for the higher states, as well as for the lowest state and thus probably gives a more reasonable estimate of the limiting ion energy below which excitational and ionization losses are relatively unimportant.

The most serious attempt to consider theoretically the interaction between slow ions, e.g., ions for which $\frac{v_o}{v_e} \lesssim 1$ or $E_o \lesssim 3A$, and matter has been made by Lindhard et al.[3] The mutual penetration of the electron clouds of atoms colliding at not too low energies (i.e., provided $E \gtrsim 100$ eV) should be appreciable and many electrons of the atoms will partake in the interaction. Thus Lindhard et al. used the statistical Thomas-Fermi model of the atom to evolve the following expressions for the cross sections S_n, S_e for decelerating, low velocity ions in a solid:

$$S_n = 3.6\, e^2 a_o \frac{Z_1 Z_2}{\left(Z_1^{2/3} + Z_2^{2/3}\right)^{\frac{1}{2}}} \frac{M_1}{M_1 + M_2} \tag{1.11}$$

$$S_e = 25\, e^2 a_o \frac{Z_1^{5/6} Z_2}{\left(Z_1^{2/3} + Z_2^{2/3}\right)^{\frac{3}{2}}} \frac{v_o}{v_H} \,. \tag{1.12}$$

Z_1, Z_2 are the atomic numbers of the incident and target particles respectively. S_n is the "nuclear" cross section for deceleration by interaction with lattice atoms, while S_e is the "electronic" cross section for deceleration by the inelastic processes of electron excitation and ionization.

The expression (1.11) is similar to one used by Bohr[1], who first

introduced the assumption that S_n is nearly constant over a considerable velocity interval at lower velocities, and used arguments of the Thomas-Fermi type to give a comprehensive description. If effects such as polarization of the medium by the incident particle are ignored, the elastic collision between it and a lattice atom can be described by a Coulomb potential of the nuclei, screened by their electron clouds, i.e., by a potential of the form:

$$V(r) = \frac{Z_1 Z_2}{r} e^2 \phi(\frac{r}{a}) , \qquad (1.13)$$

where $\phi(\frac{r}{a})$ is the screening function and a the screening length. Various authors have estimated the form of $\phi(\frac{r}{a})$ from the electron density distribution of the neutral atoms. Bohr assumed an exponential screening function,

$$\phi(\frac{r}{a}) = e^{-r/a} , \qquad (1.14)$$

with $a = a_H(Z_1^{2/3} + Z_2^{2/3})^{-\frac{1}{2}}$ and $a_H = 5.3 \times 10^{-9}$ cm. The Bohr potential gives too small values at large distances, r, and a more accurate form for the function is:

$$\phi(\frac{r}{a}) = \Psi(\frac{r}{a}) - C_2 \frac{a}{r} , \qquad (1.15)$$

where C_2 is a constant and $\Psi(\frac{r}{a})$ is the Thomas-Fermi function which is non-analytical, but the values of which were tabulated by Gombas[4]. Neilsen[5] found that the Thomas-Fermi potential could be approximated to at low particle energies by the mathematically simple $\frac{1}{r}$-type screening, so that:

$$V_{TF}(r) \simeq k \frac{Z_1 Z_2 e^2}{r^2} a , \quad a = a_o \frac{0.88}{\left(Z_1^{2/3} + Z_2^{2/3}\right)^{\frac{1}{2}}} , \qquad (1.16)$$

where k is a constant.

Thus S_n, the nuclear stopping cross section, is given by the expression (1.11) above, which is independent of the velocity, and is similar to the expression given by the simple Bohr theory ($e^{-r/a} \sim a/r$, when $r > a$, i.e.,

at low velocities). While the correct Thomas-Fermi screening function is more realistic, equation (1.11) lends itself to simple calculations and is a relatively good approximation to the former at lower velocities.

The expression (1.12) for S_e is also an approximation, but is sufficiently accurate for simple calculations, provided

$$\frac{v_o}{v_e} < Z_1^{2/3} \quad \text{or} \quad E_o \lesssim 27\, A\, Z_1^{4/3}\ \text{keV}\ , \tag{1.17}$$

considering electrons in the lowest (Bohr) orbit only. Thus (1.12) is valid for protons with energy $E_o \lesssim 27$ keV, while for A^+ ions, it is valid up to $\sim$ 60,000 keV! It has consequently been used with confidence to interpret experimental results obtained in the present work.

Equation (1.12) predicts that S_e is proportional to the velocity, as one might expect from simple physical considerations. (At low velocities the energy loss - see below - would be proportional to velocity for an atom moving through an electron gas of constant density[6] and (1.12) is essentially a smoothed function over all electron orbits).

At higher energies $\left(\frac{v_o}{v_e} >> Z_1\right)$ the Bethe[7] stopping formula

$$S_e = \frac{4\pi Z_1^2 Z_2 e^4}{m_e v_o^2} \ln\left(\frac{2m_e v_o^2}{I}\right) \tag{1.18}$$

is applicable, where I is the mean excitation energy. As (1.18) is nearly a v_o^{-2} dependence, S_e must pass through a maximum at $\frac{v_e}{v_o} \simeq Z_1^{2/3}$, below which the linearity approximation (1.12) is valid.

Figure 1.1 illustrates, qualitatively the variation in elastic and inelastic stopping cross sections with $\frac{v_o}{v_e}$ over a wide velocity range. There are no wholly satisfactory theories to predict the actual stopping cross sections over the entire velocity range.

The total stopping cross section S_T, of an ion in a medium is the sum of the elastic (or "nuclear") stopping cross section and the inelastic

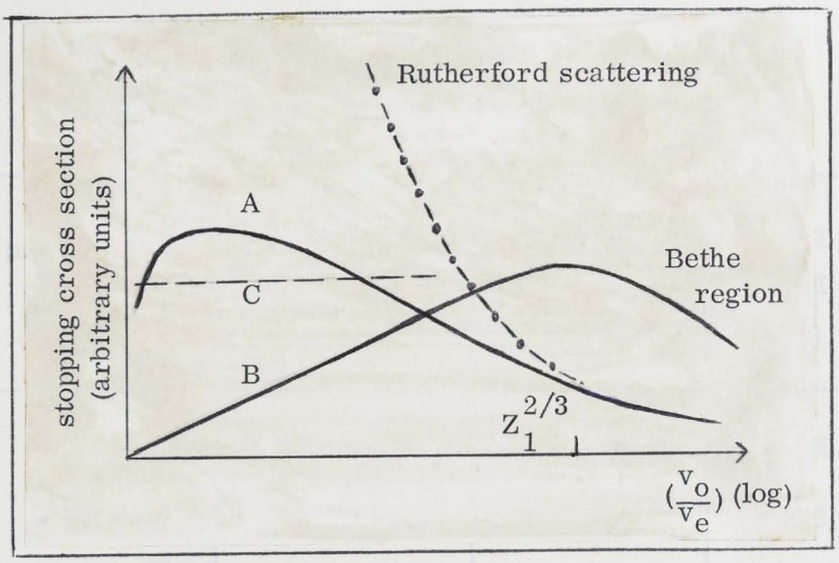

Figure 1.1

Stopping cross sections for elastic nuclear collisions (A) and electronic collisions (B). C assumes r^{-2} potential for elastic collisions.

(or "electronic") stopping cross section

$$S_T = S_n + S_e \,. \tag{1.19}$$

This is permissible as other stopping processes, such as nuclear reactions, have negligible cross sections at low and medium energies.

The rates of energy loss to the medium by the individual processes are directly related to the stopping cross sections, i.e.:

$$L_n = \left(\frac{dE}{dx}\right)_n = nS_n \tag{1.20}$$

$$L_e = \left(\frac{dE}{dx}\right)_e = nS_e \,, \tag{1.21}$$

where n is the concentration of target atoms (scattering centres).

From (1.11) and (1.12):

$$\begin{aligned} \frac{S_n}{S_e} &= 0.14\, Z_1^{1/6} (Z_1^{2/3} + Z_2^{2/3}) \frac{M_1}{M_1 + M_2} \frac{v_H}{v_o} \\ &= 0.14\, Z_1^{1/6} (Z_1^{2/3} + Z_2^{2/3}) \frac{M_1}{M_1 + M_2} \sqrt{\frac{27}{E_o} A} \,, \end{aligned} \tag{1.22}$$

where E_o is in keV. For a 10 keV ion beam incident on a Pt target, we can now construct the following table using (1.19) and (1.22).

TABLE 1.1

Incident Ion	$\frac{S_n}{S_e}$	$\frac{S_n}{S_T}$ %	$\frac{S_e}{S_T}$ %
H^+	0.021	2	98
He^+	0.18	15	85
N^+	1.7	63	37
A^+	7.9	89	11

1-2 Discussion of Interaction between Ions and Solids from the Point of View of Interpretation of Experimental Data

A. Scattering of light ions (protons) by solid media

We see from Table 1.1 that a 10 keV proton penetrating a metal (or solid medium in general) loses nearly all of its energy in inelastic collisions with orbital electrons of the metal. Yet equation (1.1) tells us that, in each individual collision, the maximum energy transferred, T_m, is very small and so the proton is effectively undeviated from its path by inelastic collisions. It will penetrate into the metal to some mean depth, determined by its energy, where it may suffer a large angle elastic collision with an atom and be "back-scattered" out of the metal. Because the mass ratio of the target atom to the proton mass is $>> 1$, the energy loss in the elastic collision events is small compared to that lost in inelastic collisions over a discrete path length, and the elastic collision serves only to deflect the proton from its original direction.

From equation (1.21) we can obtain the energy of the proton at any path length, x within the solid. Writing (1.21) in the form:

$$\left(\frac{dE}{dx}\right)_e = KE^{\frac{1}{2}}, \qquad (1.23)$$

where

$$K = 25\, e^2 a_o \frac{Z_1^{5/6} Z_2}{\left(Z_1^{2/3} + Z_2^{2/3}\right)^{3/2}} n \cdot \frac{v_o}{v_H} \cdot \frac{1}{\sqrt{E_o}}$$

(v_H is the electron velocity in the lowest Bohr orbit), we have

$$E(x) = \left(\sqrt{E_o} - \frac{1}{2} Kx\right)^2 . \tag{1.24}$$

The "one deflection model" is useful for considering the back-scattering of light ions by metals: the incident proton is assumed to suffer only a single large angle elastic collision with a target atom before it emerges from the target in the back-scattered direction. The classical conservation laws give, for an elastic collision between a projectile of mass M_1, energy E_o and a stationary target atom, mass M_2:

$$\frac{E_1}{E_o} = \frac{1}{(1+\mu)^2} \left(\cos\theta_1 \pm \sqrt{\mu^2 - \sin^2\theta_1}\right)^2 \tag{1.25}$$

$$\frac{E_2}{E_o} = \frac{4\mu}{(1+\mu)^2} \cos^2\theta_2 , \tag{1.26}$$

where $\mu = \frac{M_2}{M_1}$ and θ_1, θ_2 are the respective scattering angles in the laboratory system. E_1 and E_2 are the particle energies after the collision.

In our case, μ will always exceed or equal unity (i.e., $\mu > \sin\theta_1$), so that only the positive sign is applicable on the right hand side of equation (1.25) - i.e., E_1 is not a doubled valued function of θ_1. θ_1 can also take all values $0 - \pi$, so that:

$$\theta_1 < \pi , \tag{1.27}$$

for $M_2 > M_1$, i.e., for $\mu > 1$.

We can denote the energy of the incident particle after the collision as:

$$E_1 = R^2 E_o \tag{1.28}$$

where

$$R = \frac{\cos\theta_1 + \sqrt{\mu^2 - \sin^2\theta_1}}{1+\mu} \quad . \tag{1.29}$$

If E_o is the energy of the proton incident on the target, then it will, in general, lose some energy via inelastic processes before undergoing a large angle elastic collision. Figure 1.2 illustrates the incident ion path AC and the scattered ion path CB. Denoting the energy of the proton at C by E_c then, from (1.24) and (1.28):

$$E_c = \left(\sqrt{E_o} - \frac{1}{2}Kx_c\right)^2 \tag{1.30}$$

$$E_s = \left(\sqrt{E_c R^2} - \frac{1}{2}Kx_c \cos\phi \sec(\theta_1 + \phi)\right)^2 , \tag{1.31}$$

where x_c is the length of the incident ion path AC, θ_1 is the scattering angle and ϕ is the angle of incidence of the incident ion upon the target surface. E_s is the emergent particle energy.

From (1.30) and (1.31) we can obtain x_c as:

$$x_c = \frac{2(R\sqrt{E_o} - \sqrt{E_s})}{K(R - \cos\phi \sec(\theta_1 + \phi))} \quad . \tag{1.32}$$

Equations (1.30) and (1.31) assume a continuous inelastic energy loss along the paths AC and CB respectively.

For protons μ is usually very high compared to cos θ or sin θ, so that $R \sim 1$, giving:

$$x_c \simeq \frac{2(\sqrt{E_o} - \sqrt{E_s})}{K(1 - \cos\phi \sec(\theta_1 + \phi))} \quad . \tag{1.33}$$

The emergent protons will have an energy distribution with a maximum at some energy $E_m < E_o$, the loss being practically entirely due to inelastic losses. For a symmetrical or shapely peaked distribution, we can speak roughly of the "average" penetration path length defined by:

$$\bar{x}_c = \frac{2(\sqrt{E_o} - \sqrt{E_m})}{K(1 - \cos\phi \sec(\theta_1 + \phi))} \tag{1.34}$$

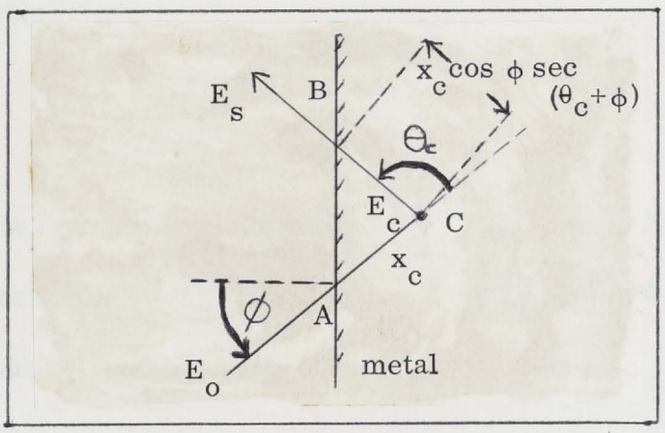

Figure 1.2

The path of a light ion in a metal.
Back scattering occurs at C.

Clearly the smaller E_m, the longer is the mean penetration path and the mean penetration depth below the surface.

$$\bar{x}_d = \bar{x}_c \cos\phi \ . \tag{1.35}$$

The probability of an elastic collision at a penetration path length x_c is:

$$dq = n\,\sigma(E_c, \theta)\, d\omega\, dx \tag{1.36}$$

where $\sigma(E_c, \theta)$ is the differential scattering cross section derived from the appropriate interaction potential.

Referring to Figure 1.2, let $q(x_c)$ denote the probability that an incident particle is NOT scattered in travelling a distance x_c and $q(x_1)$ the probability that the particle deflected at $x = x_c$ reaches the surface without a further deflection. Then the probability of the particle emerging from the surface is:

$$dP = q(x_c)\, q(x_1)\, dq = q(x_c + x_1)dq\,, \tag{1.37}$$

or from (1.36):

$$dP = q(x_c + x_1)\, n\, \sigma(E_c, \theta)\, d\omega\, dx\,. \tag{1.38}$$

We can write

$$dP = \frac{dN}{N_o}\, d\omega\,, \tag{1.39}$$

where N_o is the number of incident particles/cm^2 and dN the number of incident particles which are scattered through an angle θ in a layer dx at $x = x_c$. Thus from (1.38) and (1.39):

$$\begin{aligned} dN d\omega &= N_o\, dP \\ &= N_o\, q(x_c + x_1)\, n\, \sigma(E_c, \theta)\, d\omega\, dx\,. \end{aligned} \tag{1.40}$$

Now $q(x_c + x_1)$ is assumed to be equal to 1 in the "single deflection model" and we can write $dN = dN(E_s)$, to indicate that the emergent particles which have been scattered through an angle of θ in a layer dx at $x = x_c$, have energies E_s (Figure 1.36). Then, using (1.31) and (1.33), we can write:

$$dN(E_s)\, d\omega\, dE_s = n\sigma\left(\left\{\frac{\sqrt{E_s} - \sqrt{E_o}\cos\phi\,\sec(\theta+\phi)}{R - \cos\phi\,\sec(\theta+\phi)}\right\}^2, \theta\right)\frac{n\, d\omega\, dE_s}{K E_s^{\frac{1}{2}}(R - \cos\phi\,\sec(\theta+\phi))} \tag{1.41}$$

and so the total number of back-scattered ions, N_{TE}, with energy > E is:

$$N_{TE} = \int_{\frac{\pi}{2}}^{\pi}\int_{E}^{E_o} n\sigma\left(\left\{\frac{\sqrt{E_s} - \sqrt{E_o}\cos\phi\,\sec(\theta+\phi)}{R - \cos\phi\,\sec(\theta+\phi)}\right\}^2, \theta\right) \frac{n\, d\theta\, dE_s}{K E_s^{\frac{1}{2}}(R - \cos\phi\,\sec(\theta+\phi))} \tag{1.42}$$

Thus the form of the energy spectrum of the scattered ions provides us with means of estimating

(1) The form of the scattering cross section σ, and hence the true interaction potential at various incident ion energies.

(2) The mean depth of penetration of the ions from (1.34).

(3) The general validity of the expressions (1.11) and (1.12) for the elastic and inelastic cross sections, i.e., whether elastic or inelastic scattering predominate at various incident ion energies.

McCracken and Freeman[8] tried a variety of forms for σ in (1.42) and compared the calculated number of back-scattered deuterons and protons with experimental observation. For light ions on metals, useful analytical expressions can be obtained by assuming simple Rutherford back-scattering (see Figure 1.1).

In the 10 - 30 keV region for light ions, we are on the threshhold of validity for the Lindhard-Scharff equations (1.11) and (1.12), but the screening is sufficiently small for the screened coulomb scattering to be approximated to by Rutherford scattering.

Using the Rutherford scattering cross section, (1.42) becomes:

$$N_{TE} = -1.42\, f(z)\, I(\theta)\, E_o^{-3/2}, \qquad (1.43)$$

where E is in keV and $f(z) = Z_1^{5/6} Z_2 (Z_1^{2/3} + Z_2^{2/3})^{3/2} \simeq Z_2^2$ if $Z_1 << Z_2$ and $I(\theta)$ is an integral which has been evaluated numerically and is plotted in Figure 1.3a as a function of E for several R values. (Remember that N_{TE} is the number of back-scattered ions with energy exceeding E.) Figure 1.3b shows the number of back-scattered protons with E = 1 keV, for various targets, calculated from (1.43).

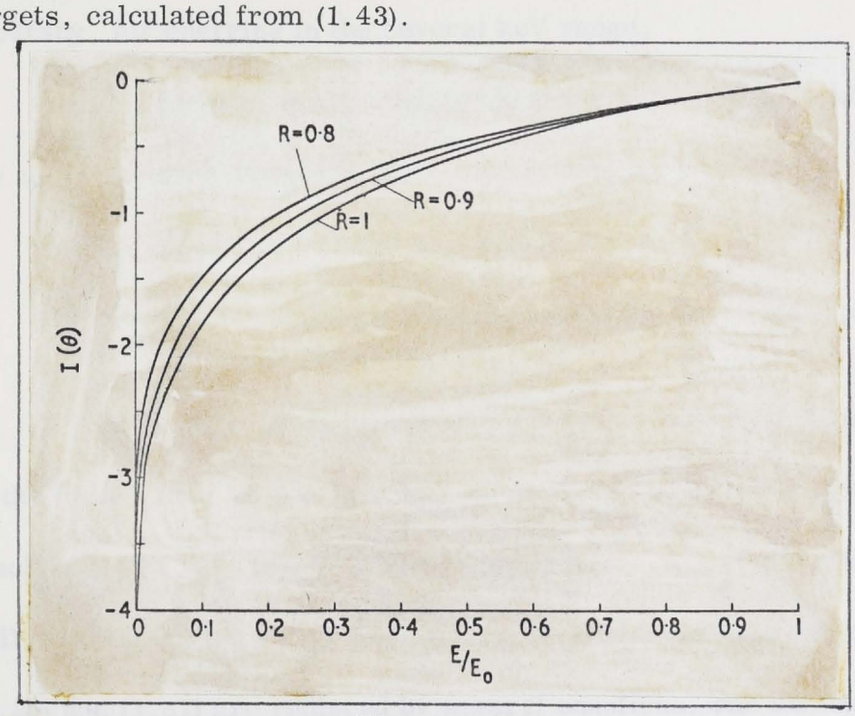

Figure 1.3a

Integral $I(\theta)$ as a function of energy for different energy losses in the scattering collision.

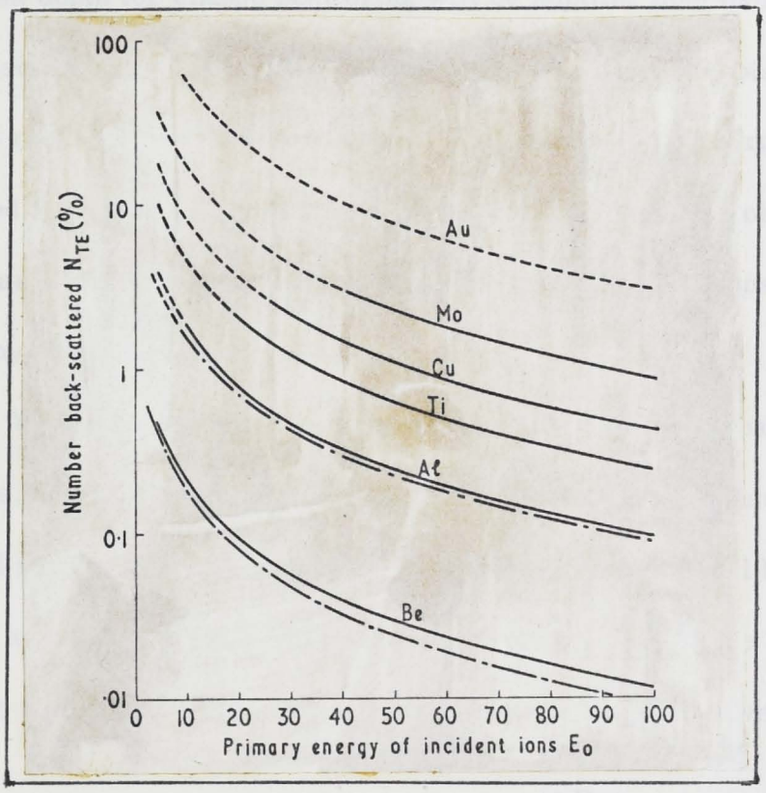

Figure 1.3b

Number of ions back-scattered with an energy greater than 1 keV assuming Rutherford scattering.

——— Uncorrected for energy loss in scattering collision
— - — - Corrected for energy loss in scattering collision
-------- Effect of screening greater than 10%.

For heavy targets such as platinum the screening is not negligible and so the results for N_{TE} from (1.43) are only qualitative. In Chapter IV, we will see that (1.43) does predict the observed changes in N_{TE} with E_o, to considerable accuracy, for energies in the several keV range.

Two considerations which complicate any experimental verification of the above theoretical results must now be considered:

(1) The effects of multiple scattering events.

(2) The effects of charge changing events as the incident particle moves through the solid.

While multiple elastic scattering events may make some contribution to the total scattering for large Z_2 targets, we would not expect them to have much effect on the shape of the energy spectra. Nearly all of the energy loss will still be by inelastic processes between the elastic scattering events and (1.30) and (1.31) are replaced by several equations, one for each elastic event.

The mean depth for elastic scattering will be smaller than indicated by (1.34) and the scattering cross section will be greater. The attempts of several Russian researchers[9] to attribute the broadening of the energy spectra of scattered light ions (H^+ and He^+) from metals, to multiple collisions is not tenable as Table 1-1 shows that at medium energies, light ions lose most energy by inelastic processes.

While the above discussion refers to the spectra of back-scattered particles, forward-scattered protons (e.g., protons which pass through a thin foil) will show the effects of multiple collisions, as there will be a high probability of an emergent proton having suffered many small angle scattering events - the mean square deflection at some point x in the target is given by:

$$\langle\theta^2\rangle = 2\pi n_o Z_2^2 e^4 Z_1^2 \frac{x}{E_o^2} \ell n \frac{a E_o}{Z_2 e^2} , \qquad (1.44)$$

assuming Rutherford scattering for simplicity[10]. For $x \sim 100 - 400$ Å and $E_o \sim 7 - 35$ keV, the average deflection is only $\sim 5^o$. Multiple collisions will decrease the effective path length as particles scattered in the forward direction have a greater probability of escaping from the foil and so the mean energy of the forward-scattered particles will be increased relative to the back-scattered particles[11].

We shall now discuss the charge exchange processes accompanying scattering in solids. The charge of the emergent particle will be entirely unrelated to the charge of the incident particle for, when $\frac{v_o}{v_e} \sim 1$, the outer electrons will be stripped off with a finite probability and the actual ionic charge will oscillate about a most probable value which is dependent upon the ion energy - a steady state charge distribution is attained which is dependent upon the relative values of the charge exchange cross sections.

For protons on solid targets the emergent particles are predominantly neutral (H^o atoms) at energies $\lesssim 3 - 7$ keV, as the slow moving particle will quickly capture an electron from the solid. Moreover, there will be considerable

numbers of these neutrals as the scattering cross sections (Rutherford or screened coulomb) increase sharply at these energies. This will be confirmed in the present work and several other researchers have made similar observations[12, 13]. At higher incident proton energies, the captive cross section falls rapidly and at ~ 30 keV most back-scattered particles will emerge as protons. The total scattering, however, will be less than at small energies, because of the smaller scattering cross section. The formation of H^- ions, also reported in the present work, is not so easy to visualize, as it depends upon the interaction between several charge changing cross sections. However, from the work on charge changing events of protons in gases[14], we would expect the flux of emerging H^- ions to peak at around several keV and this is verified by the present investigations. Also, ions emerging as H^- would, on the average, have spent more time in the lattice and so the mean penetration depth $\bar{x}_c$ will be greater than for emergent protons at a given incident particle energy.

The cross section σ in (1.42) must be multiplied by $\frac{\sigma_{01}}{\sigma_{01} + \sigma_{10} + \sigma_{0\bar{1}} + \sigma_{\bar{1}0}}$, where σ_{ik} are the charge changing cross sections at the beam energy considered, to obtain the number of back-scattered protons alone. The double charge transfer cross sections $\sigma_{\bar{1}1}$ and $\sigma_{1\bar{1}}$ can be assumed negligible compared to the others.

B. Scattering of Heavy Ions (Argon Ions) by Solid Media

The velocity of an A^+ ion is only of the order of 15% that of a proton at the same energy and Table 1-1 indicates that only ~10% of its energy is expended in electronic inelastic processes in a solid medium, at several keV energies. For A^+ we have $\frac{v_o}{v_e} = \frac{1}{2}$, when $E_o \approx 6A$ keV = 240 keV from (1.5) and so, even according to the Bohr criterion (1.6), we would expect interaction with electrons to be small.

An A^+ ion at 10 keV will have a high probability of capturing an electron from the target, both by virtue of its low (relative to v_e) velocity, and its high ionization potential. Thus the particle is in the neutral state for most of the time it moves through the lattice, and most of the scattered particles will be

neutral A^o atoms. Those A^+ atoms which are scattered will either be incident particles scattered from the first few atomic layers before they have been neutralized, or scattered A^o atoms from deeper layers, which have lost electrons again, probably near or at the surface.

As M_1 is now much more than for a proton, the energy loss factor R (equation (1.29)) is much more at a given scattering angle. Not only is the probability of an elastic collision with a lattice atom greatly enhanced, but the elastic energy loss in each such collision is greatly increased.

The scattered A^+ and A^o particles will have distinctly different energy distributions, as the latter originate from events deeper in the metal and so will be much broader, in the same way as the H^- spectra will be broader than the H^+ spectra. The A^+ spectra will, however, bear little resemblance to the H^+ spectra, as in the former case we observe particles which have lost DISCRETE amounts of energy in a FINITE number of two-body collisions. A consideration of the equations (1.25) and (1.26) shows that at a given angle of incidence θ_1, we will observe not only particles scattered from single events but some particles which have undergone two, three or even more collisions in such a way that the algebraic sum of the individual angles, ν_i equals θ_1. The energy of the multiply-scattered particle is given by:

$$E_n = \sum_{i=1}^{n} \frac{\cos \nu_i + \sqrt{\mu^2 - \sin^2 \nu_i}}{(1+\mu)^2} E_i - 1, \quad \theta_1 = \sum_{i=1}^{n} \nu_i , \qquad (1.45)$$

for n multiple collisions.

Multiply-scattered ions will have a HIGHER average energy than singly-scattered ions, neglecting inelastic energy loss, as a simple calculation shows. For A^+ on Pt, then for a single scattering event through $\theta = \pi/2$, R^2 (equation 1.28) is 0.67, while for two consecutive events with $\nu_1 = \nu_2 = \pi/4$, R^2 is $0.88 \times 0.88 = 0.77$. The small angle collisions are "softer" in the sense that they have larger impact parameters than the large angle ($\pi/2$ in this case) collision.

The elastic peak in most heavy ion spectra also has a broad low energy tail, especially for N^+, O^+ and C^+. So far, we have discussed proton and argon ion spectra as representative of the two main groups of spectra considered in this report. However, Table 1-1 shows that a 10 keV N^+ ion loses $\sim 40\%$ of its energy in travelling unit length by electronic inelastic processes, so some inelastic broadening is not surprising.

Several theoreticians[15] have pointed out that inelastic processes, other than direct excitation and ionization (which are important provided $v_o \gtrsim v_e$), can play an important role in collisions between heavy ions, in view of the considerable overlap of the electron shells. The colliding atoms at intermediate energies spend sufficient time in close proximity for a quasi-molecule to be formed. This complex structure will have a continuously varying set of energy levels, due to the relative motion of the nuclei and a statistical model is necessary to determine the distribution of the electrons over the changing energy levels. Firsov[15], using the Thomas-Fermi model of the atom, argued that the electrons will be excited by the relative kinetic energy of the atoms and the outer electrons will be auto-ionized by this energy which is quite large in comparison with the energy required for a single direct ionization.

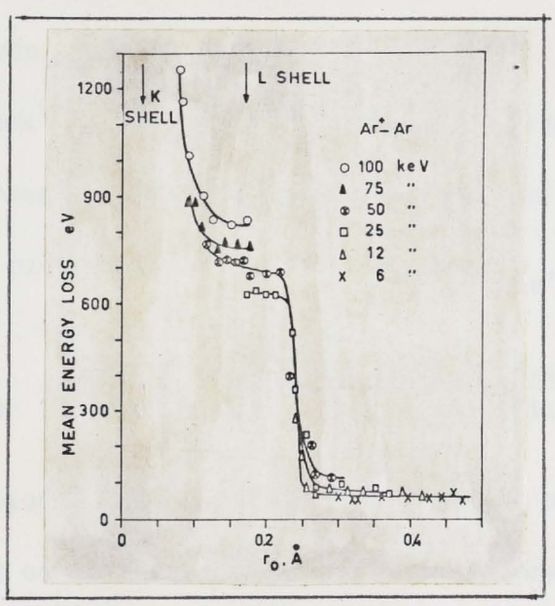

Figure 1.4

The mean energy loss as a function of the distance of closest approach measured for collisions between Ar^+ ions of various primary energies, and Ar atoms. The radii of the K and L shells of a single Ar atom are indicated by the arrows. r_o is calculated for the Bohr potential[16].

Figure 1.4 shows the mean energy loss $\overline{Q}$ as a function of the distance of closest approach for A^+ ions on A atoms at various energies, as observed by Morgan and Everhart[16]. At a given energy the degree of interpenetration depends on the scattering angle: one sees that at 6 keV, $\overline{Q}$ is small, only ~ 50 eV for all angles, but for 50 keV incident ions, $\overline{Q}$ can reach close to a kilovolt at large θ (small r_o). The mean energy loss $\overline{Q}$ can be calculated from the expressions given by Snoek and Kistemaker[17a]:

$$\frac{\overline{Q}}{E_o} = \frac{2}{\mu}\sqrt{\frac{E_1}{E_o}}\cos\theta_1 - \left(\frac{1-\mu}{\mu}\right) - \frac{1+\mu}{\mu}\frac{E_1}{E_o} \qquad (1.46)$$

$$\frac{\overline{Q}}{E_o} = 2\sqrt{\frac{\mu E_2}{E_o}}\cos\theta_2 - (1+A)\frac{E_2}{E_o} \quad . \qquad (1.47)$$

The effect of auto-ionization processes (inelastic energy losses in single collisions) will be to shift the elastic peak towards lower energies by an amount $\overline{Q}$ and also to broaden it by an amount by which the actual values of Q spread around the mean value $\overline{Q}$. Although considerable interpenetration of the electron clouds of the colliding particles will occur for all two-body collisions down to very low energies, $\overline{Q}$ apparently becomes significant only for nuclear separations of $\sim \frac{1}{5}$ Å or less.

Russek[16] showed that at sufficiently high penetrations, the auto-ionization process will give rise to multiply charged ions and he calculated the ionization probabilities for n-fold ionization, P_n, defined by:

$$P_n = \frac{\text{number of ions with charge n scattered}}{\text{total number of scattered particles}} \quad . \qquad (1.48)$$

Russek found good agreement with the experiments of Everhart et al., on gaseous phase collisions and scattering of heavy ions from solid surfaces can also be expected to result in multiply charged ions under the appropriate conditions.

1-3 The Sputtering of Solid Media by Ions

In discussing our experimental data, we will need to bear in mind several basic facts about sputtering, in order to confirm, or otherwise, the presence of this phenomenon in our results.

Considering equation (1.26) we see that the energy, E_2 of the struck target atom after the collision is quite small for all except small scattering angles θ_2, which are not usually observed experimentally in back-scattering experiments.

Consider an experiment where the displaced target particles are collected at $\frac{\pi}{2}$ to the incident beam direction and over a cone of vertex 2β.

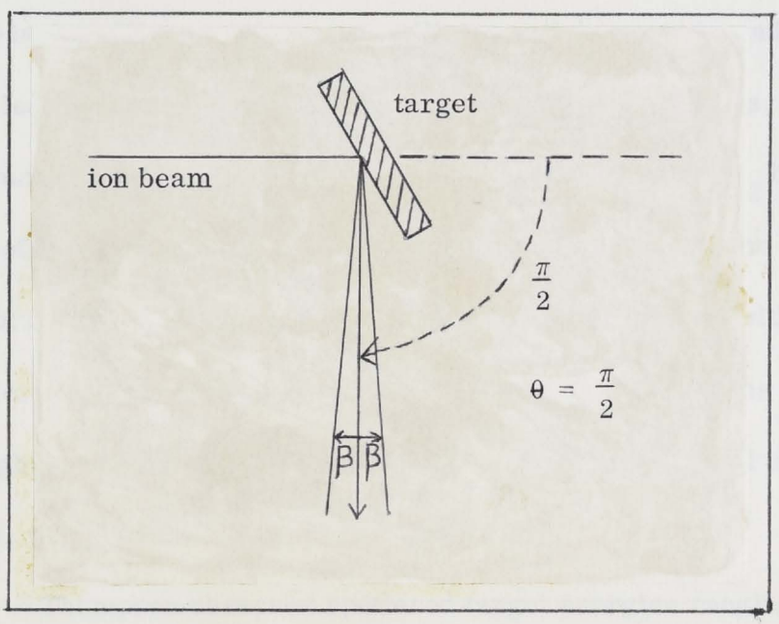

Figure 1.5

Target geometry relative to incident beam and collector

Then from (1.26):

$$0 \leq E_2 \leq E_o W_{12} \sin^2 \beta , \tag{1.49}$$

where

$$W_{12} = \frac{4\mu}{(1+\mu)^2} . \tag{1.50}$$

If $\beta = 3.7^o$, as in the present observations, then:

$$0 \leq E_2 \leq 0.004\, E_o\, W_{12} \,. \tag{1.51}$$

For protons on platinum the right hand side is only $\sim 10^{-4}\, E_o$, or 2 eV for a 20 keV energy incident beam! For A^+ it is $\sim 0.002\, E_o$, or 20 eV for a 10 keV energy incident beam. On the basis of these estimates, no sputtered target particles would be observed for proton bombardment of platinum, as E_2 is less than the displacement energy of the lattice atoms from their sites (~ 10 eV).

Thompson et al.,[17] have discussed the sputtering mechanism in considerable detail. In the so-called random cascade model each of the primary recoils generates a collision cascade in which energy is distributed by a series of two-body collisions, the mean collision path being independent of E_2. This would lead to a $\frac{1}{E_2^2}$ dependence down to very small energies, for the energy spectrum. However, the atoms are not free and so when E_2 becomes of the order of the displacement (or binding energy) at ~ 10 eV, the displaced atom will not escape from the lattice and the interaction will be with the lattice as a whole. Thus the energy distribution of the sputtered atoms peaks at 1-10 eV, although there will be sputtered particles with energies well above this (see below), and drop to zero at lower energies.

Thompson observed sputtered target energies ranging from 10^{-2} eV to 10^4 eV for 45 keV - A^+ on Cu. Considering the random cascade model in simplified terms, we have after n two-body collisions:

$$0 \leq E_{2n} \leq E_o\, W_{12}\, W_{23} \ldots\ldots W_{n,n+1}\, \frac{\cos^{2n}(\pi - 2\beta)}{n} \,, \tag{1.52}$$

or, as $n \longrightarrow \infty$,

$$0 \leq E_{2n} \leq E_o\, W_{12} \,, \tag{1.53}$$

assuming $W_{23} = W_{34} = \ldots\ldots = W_{n,n+1} = 1$, i.e., that all atoms in the cascade are identical. Thus for 10 keV, A^o on Pt, the sputtered metal particles can have energies as high as ~ 5.5 keV, much higher than the

maximum calculated for a single simple collision (equation (1.49)), with $\theta_2 = \frac{\pi}{2}$. The mean energy, however, will be far less than this maximum (see below).

The yield of particles sputtered as ions is only a very small fraction of the total sputtering yield and indeed Bradley et al.,[18] estimated from their data, that the ratio of sputtered Pt^+ to sputtered Pt atoms, for noble-ion bombardment, was only $\sim 10^{-3}$ over a wide range of experimental conditions and in fact, Fogel[19] points out that where sputtered ions exceed more than about $\sim 1\%$ of sputtered atoms, they are mainly sputtered from oxides or other impurities on the metal surface. The fact that so few sputtered particles are charged is a consequence of their small (< 200 eV) mean energies. In general the probability that an ion captures an electron from a medium or at a surface increases as its velocity decreases and so only relatively few higher velocity sputtered ions will escape neutralization. Even so, their mean energies will not exceed a few hundred eV.

Several workers have measured the variation of the sputtering yield with energy[20] and all found a variation of the form shown in Figure 1.6 for A^+ on Cu. All energy-yield curves have a well defined "back" section AB.

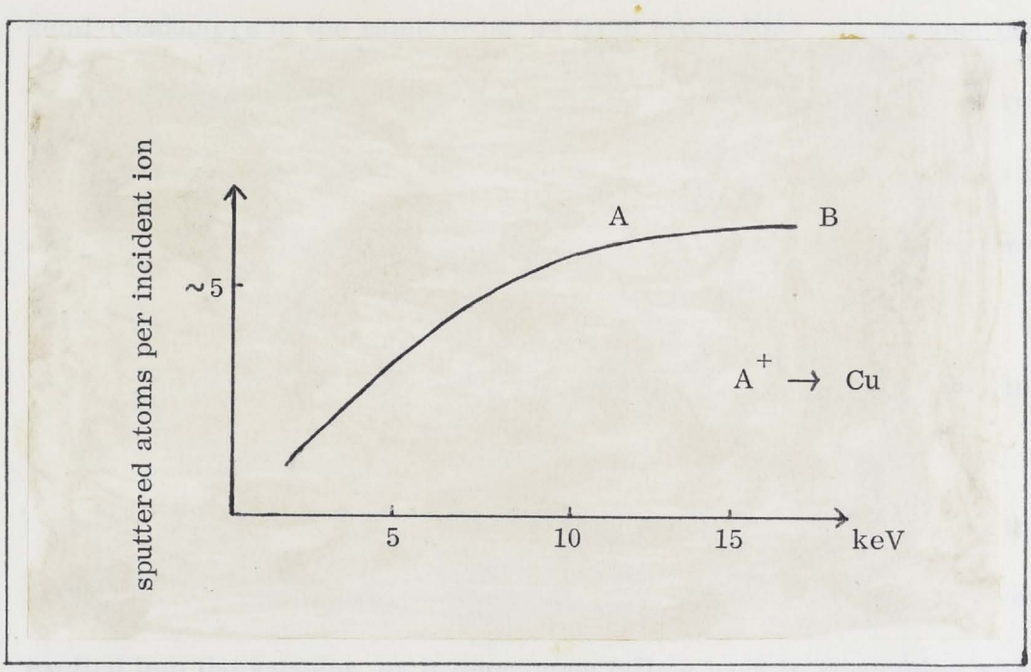

Figure 1.6

Variation of sputtering yield with energy as observed by several workers.

Also the experimental evidence is that the sputtering yield and the value of the mean energy of the sputtered particles depends upon the number of electrons dn in the outermost "d" shell[21]. Thus inert gas bombardment of Ni gives much the same sputtering yield and values for $\overline{E}$ as Pt (dn = 8, 9 respectively) while Ta (dn = 3) and Mo (dn = 5) will have smaller yields, but larger values for $\overline{E}$.

1-4 Secondary (Kinetic) Emission of Electrons from Solid Media Under Ion Bombardment

In section 1-2 we saw that there occurs considerable interpenetration of the electron clouds of particles colliding at not too low energies and that many electrons consequently take part in the collision. Also in section 1-1, we saw that the cross section for decelerating a particle by interaction with electrons increases linearly with particle velocity up to $\sim 27\ A\ Z_1^{4/3}$ (equation (1.17)). Some of the electrons involved in these processes are given sufficient energy to escape from the solid and this process is termed kinetic ejection.

It is now generally accepted that kinetic ejection results from the ionization of lattice atoms by the incident particles. The ejected electrons originate from bound states, as indicated experimentally by their maximum energies (Chapter III) and the presence of kinetic ejection from insulators and semi-conductors of the same order as from conductors. (A distinct process, termed potential emission, involves the transfer of potential energy from the incident ion to a conduction band electron leading to electron emission by an Auger process. It is not a kinetic process involving inelastic collisions and ionization.)

From a theoretical standpoint, the principal problem is how to calculate the energy lost by an ion in the inelastic process. The energy, δE, transferred to the electrons, must be sufficient to raise them across the forbidden band into the conduction band. The excited electron may be directly excited into the vacuum, or it may, upon falling back to recombine with a positive hole, excite another conduction band electron via an Auger process,

causing the latter to be emitted. Figure 1.7 illustrates these emission processes.

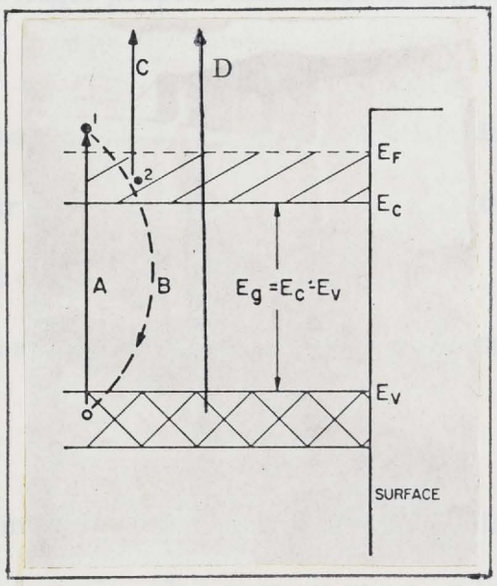

Figure 1.7

Most probable ejection modes for electron kinetic ejection

A: Ionization of inner shells by incident particle.
Excitation of electron 1 to conduction band.
B: Hole-electron recombination.
C: Auger emission of conduction electron 2.
D: Direct excitation of valence electron to continuum.

The most successful theory for the medium energy range is that of Parilis and Kishinevski[22]. They considered the energy transfer to excited electrons to be along the lines described by Firsov[15]: Figure 1.8 illustrates the kinetic energy exchange by the electrons during a fast ion-target collision.

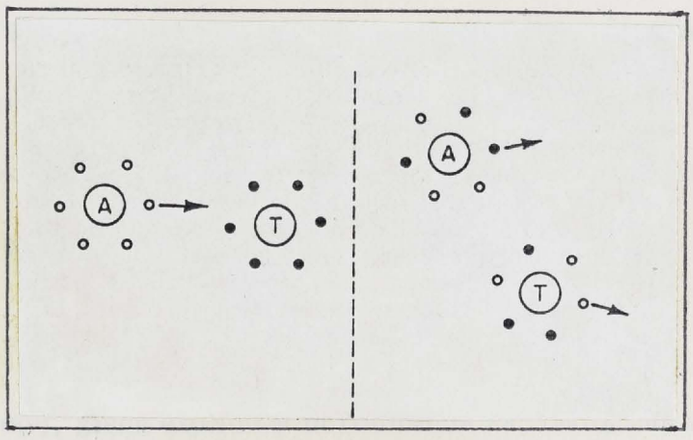

Figure 1.8

Illustration of Kinetic energy exchange by electrons during a collision between a fast ion and target atom.

This heating of the electron clouds, by virtue of their assimilation of the translational motion of the nuclei enables δE and hence the cross section

$\sigma(v)$ of the ionization process to be calculated. The excitation process is assumed to be the Auger process illustrated in Figure 1.7 and not direct excitation.

The mathematics of their treatment is too involved to reproduce here and only their main concepts and results are stated for later comparison with experimental data.

Parilis and Kishinevski expressed $\gamma(v)$ in the form:

$$\gamma(v) = N\sigma^*(v)\lambda w, \tag{1.54}$$

where N is the number of lattice atoms per cm^3, λ is the mean free path for the electrons in the target, $\sigma^*(v)$ is the "effective" ionization cross section (see below) and w is the probability of the Auger electron ejection process, i.e., of the excited electron escaping from the surface. w can be approximated to by the empirical formula:

$$w = 0.016\,(\delta - 2\phi), \tag{1.55}$$

where δ is the "hole depth" and ϕ the work function. The excited electrons formed at a depth x below the surface will be partly absorbed in travelling or "diffusing" to the surface and an $e^{-\frac{x}{\lambda}}$ absorption probability was assumed in calculating $\sigma^*(v)$.

The "effective" cross section in (1.54) is not simply $\sigma(v)$, the cross section for ionization of a lattice atom by the incident ion at velocity v, as the incident ion will be retarded before it reaches the average depth for electron excitation. Thus Parilis and Kishinevski wrote:

$$\sigma^*(v) = \sigma(v) - \Delta\sigma(v) \tag{1.56a}$$

where $\Delta\sigma(v)$, given explicitly in reference 22, takes this retardation into consideration. The actual decrease in velocity with depth x was assumed to follow the simple law:

$$v^2 - v_x^2 = kx, \tag{1.56}$$

where k is a constant and v_x the velocity at depth x, i.e., the energy loss

per unit length was assumed constant as in the expression for S_n (1.11). At higher velocities S_e (1.12) starts to become significant and so (1.56) is inaccurate. From Table 1-1, $S_e >> S_n$ for protons at 10 keV and we would not expect the Parilis-Kishinevski theory to be valid in this case, unless the assumption (1.56) was modified to account for losses due to collisions with individual electrons as well as with lattice atoms. Parilis and Kishinevski did, indeed, rather arbitrarily, restrict the range of validity of their theory to $\frac{1}{4} < \frac{Z_1}{Z_2} < 4$.

The ion will continue to produce electrons until, at some depth $x = x_s$, its energy has fallen to the "threshhold" value for the ionization process. At low velocities, at depth $x = x_s$, the kx term in (1.56) becomes appreciable relative to the squared incident velocity and so the $\Delta\sigma(v)$ factor in (1.56a) is important. At high velocities the energy loss by the ion in penetrating to a depth x is small relative to the incident energy and so the $\Delta\sigma(v)$ factor is less significant.

We can now enumerate the main trends predicted by the above theory for comparison with our experimental data in Chapter II.

(i) At very low velocities the ionization cross section will be too small to lead to electron ejection from the solid.

(ii) At velocities at or slightly above the threshhold v_{min}, the $\Delta\sigma(v)$ term in (1.56) is important and

$$\gamma \propto v^2 - \left(\frac{3}{2} v_{min}\right)^2, \tag{1.57}$$

i.e., there is a v^2 dependence for the emission.

(iii) At velocities > $2v_{min}$

$$\gamma \propto v \tan^{-1}\{0.6_{\bullet}10^{-7}(v - v_m)\} \rightarrow c(v - v_{min}), \tag{1.58}$$

i.e., γ approaches a linear velocity dependence, the velocity being measured above the threshhold. The value of v_{min} obtained by extrapolation of the linear portion back to $\sigma(v) = 0$, is given by:

$$v_{min} = 1.05 \times 10^7 \text{ cm/sec} \tag{1.59}$$

for all target-ion combinations.

(iv) At very high velocities x_s is so great that not all electrons formed in the deeper layers can escape. Thus γ ceases to increase with

velocity but saturates and eventually decreases. However, the maximum occurs at velocities well above those attained in the present investigations, even for the lighter ions.

(v) There is no dependence of γ upon the ionic charge.

(vi) The dependence of γ upon Z_1, Z_2 is given by,

$$\left(\frac{Z_1 + Z_2}{Z_1^{\frac{1}{2}} + Z_2^{\frac{1}{2}}} \right)^2 .$$

For lighter ions equation (1.56) must be modified to take electronic loss processes into account and Parilis and Kishinevski showed in a later paper[23] that the governing function for light ions is:

$$(Z_1^{\frac{1}{2}} + Z_2^{\frac{1}{2}})(Z_1^{1/6} + Z_2^{1/6})^3 .$$

(vii) All impact-ionization theories predict that γ varies with the angle of incidence α in accordance with:

$$\gamma = \gamma_N \sec \alpha , \qquad (1.60)$$

where γ_N is the emission at normal incidence. This is expected as the probability of formation of electrons is a function of the actual distance traversed which, at a given depth, is proportional to sec α.

The comparison of the above predictions with experimental observation will indicate that electron kinetic ejection is a consequence of release of bound electrons by impact-ionization. No other interaction hypothesis can explain the observed behaviour so well qualitatively, although the Parilis and Kishinevski theory is not quantitatively precise, especially for light ion bombardment.

The hypothesis that kinetic ejection results from the transfer of energy to free or loosely bound electrons is not supported by the presence of considerable numbers of secondary electrons well above the maximum expected for a simple two-body collision (see Chapter III). A modified form of this hypothesis, however, was advanced by Izmailov[24] who argued that the kinetic emission is a result of ejection of free conduction electrons by transient fields produced by the collision between the incident and target atoms. His theory predicts that $\gamma \propto \frac{E_o}{M_1}$ at low energies and that the maximum energy of the emitted electrons depends upon the work function ϕ and the Fermi energy E_f,

through an expression of the form:

$$E_{e\,max} = E_f \left(0.132 + 0.251 \frac{\phi}{E_f} + 0.119 \left(\frac{\phi}{E_f}\right)^2 + \ldots\ldots\right). \quad (1.61)$$

Von Roos[25] assumed that the lattice atoms behave as a gas and that the incident ions have a distribution function influenced solely by elastic collisions between them and the "free" lattice atoms. From section 1-1, it is clear that for light ions at medium energies, ionization events will mainly determine the distribution function, even accepting the dubious assumption of a "gas" of lattice atoms which behaves like a classical gas. Von Roos also assumed that all secondary electrons formed actually escape from the metal, i.e., that x_s is so small that the absorption factor $e^{-\frac{x}{\lambda}}$ is negligible: this also limits the possible validity of his theory to very low velocities and targets of high atomic number. His theory predicts that for 1 - 10 keV, heavy ions on metals:

$$\gamma \propto \mu\left(1 + \frac{1}{\mu}\right)^4 \quad \text{at constant incident ion energy}$$

$$\gamma \propto \mu^3\left(1 + \frac{1}{\mu}\right)^4 \quad \text{at constant incident beam velocity}, \quad (1.62)$$

where

$$\mu = \frac{M_2}{M_1}.$$

High energy theories form a distinct category and although the basic hypothesis - impact ionization - is similar to that of the most successful low energy theories, the details of the calculations and the assumptions are quite different. At high energies x_s is very large and most secondaries originate from smaller distances below the target than this. Also, the electronic loss cross section S_e (equation (1.12)) becomes appreciable relative to the elastic loss cross section S_n (equation (1.11)).

The Bohr-Bethe theory (equation (1.18)) must be employed at these higher energies and the two main treatments of the problems are those given

by Sternglass[26] and Ghosh and Khare[27]. Further details will not be given here, as they lie outside the energy range of this work.

1-5 Conclusion

In this Chapter, we have discussed, in a semi-descriptive fashion, the theoretical basis for the mass of experimental work to be presented in the next three chapters and in the Appendix. This will enable us to interpret the observed data in terms of the fundamental physical processes involved and thus extract maximum information from such data. The present chapter has, of necessity, covered a broad range of medium energy phenomena produced by ion bombardment of metal surfaces and all such phenomena will be referred to in the course of subsequent discussions. Certain phenomena such as potential secondary electron emission have not been discussed in detail, but where such phenomena do affect the data and its interpretation, they are referred to in the accompanying discussion.

For more thorough discussions of all individual topics or phenomena, the reader is referred to the listed references (pp. 161 - 163).

CHAPTER II

MEASUREMENTS OF TOTAL SCATTERING OF IONS AND EMISSION OF ELECTRONS

2-1 Preliminary Observations

A. Experimental arrangement and discussion

The preliminary work consisted of observations made on the total secondary ion and electron emission, from an incandescent platinum target, under hydrogen ion bombardment (H_1^+, H_2^+, H_3^+) at pressures of 2 - 5 x 10^{-8} mm and incident ion energies of 5 - 50 keV.

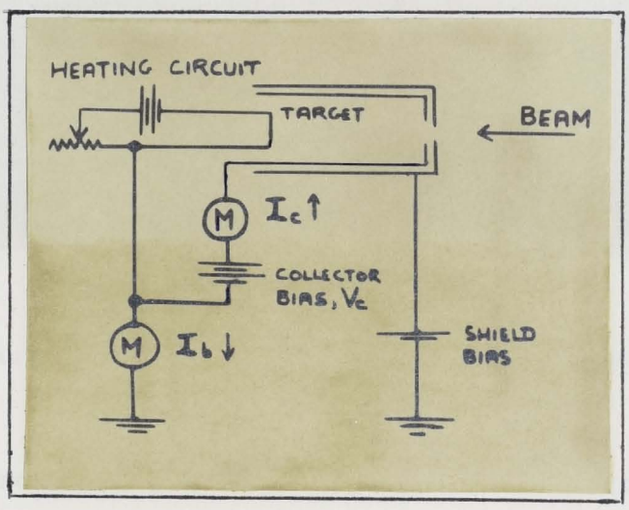

Figure 2.1

Electrode system and measuring circuit employed for preliminary observations on ion and electron emission.

The measuring apparatus employed is shown in Figure 2.1. The target is normal to the incident beam and is enclosed by a collecting electrode at potential V_c respect to it. The collector is, in turn, enclosed by a shield electrode to repel any secondary electrons from beam defining apertures further down the system (see Appendix). The shield aperture is also slightly smaller than the collector aperture, to ensure that no incident beam particles strike the collector.

As V_c, the collector bias, is varied, the collector current, I_c, is measured and the incident beam current, I_b, is monitored. Phillips meters

model PM 2401 were sufficiently sensitive to be employed in these measurements as the incident beam current was always in excess of 0.25 microamps during experimental runs.

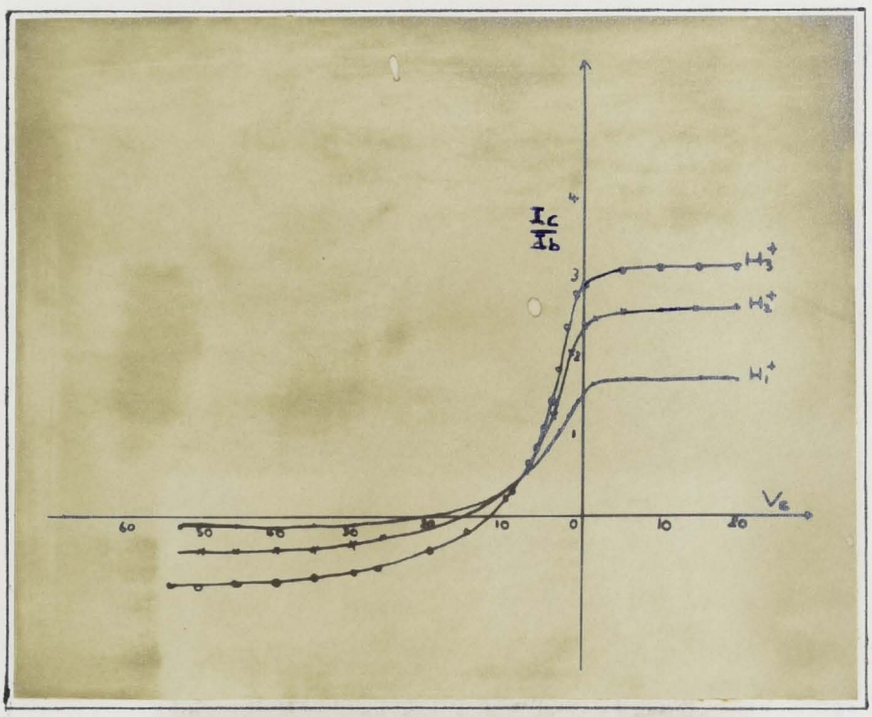

Figure 2.2

Typical variation for normalized collector current as a function of collector bias.

Figure 2.2 shows the characteristics for the normalized collector current plotted against the collector bias. It can be seen that for V_c values greater than about 5 volts and less than - 40 volts, the co-ordinate saturates and we can define the quantities,

$$\gamma' = \frac{I_c}{I_b} , \qquad \text{for } V_c > + 5 \tag{2.1}$$

$$R = \frac{I_c}{I_b} , \qquad \text{for } V_c < - 40 . \tag{2.2}$$

In order to ascertain what γ' and R actually represent physically, we must analyse the various components of the measured currents I_c and I_b. Table 2.1 indicates the constituents of the net 'collector' and 'beam' currents for some arbitrary collector voltage. In this table, the constituents are

grouped into primary, secondary and tertiary components: the primary component consists of the current of incoming particles, the secondary components are those originating from the target and the tertiary components are those originating from the collector. Higher sequence components are neglected, as their contributions are estimated to be less than the experimental error.

TABLE 2.1

	Primary	Secondary (+)	Secondary (-)	Tertiary (+)	Tertiary (-)
I_c		i_2^{i+} i_s^{i+} i_x^{i+} i_{th}^{i}	i_2^{i-} i_s^{i-} i_x^{i-} i_2^{e} i_{th}^{e}		i_{3e}^{e} i_{3i}^{e} i_{3m}^{e} i_{3s}^{e}
I_b	i_1^{+} i_{bc}	i_{be}	$i_{bi}^{\pm}$		

i_1^{i} = primary ion current striking target.

i_2^{i+} = reflected positive ion current from target.

i_2^{i-} = reflected negative ion current from target.

i_s^{i+} = sputtered positive ion current from target.

i_s^{i-} = sputtered negative ion current from target.

i_x^{i+} = positive ion current from impurities on the target surface.

i_x^{i-} = negative ion current from impurities on the target surface.

i_{th}^{i} = current of thermally desorbed ions (predominantly positive).

i_2^{e} = current of secondary electrons from target.

i^e_{th} = current of thermally emitted electrons from target.

i^e_{3e} = tertiary current arising from secondary electrons striking the collector.

i^e_{3i} = tertiary current arising from reflected ions striking the collector.

i^e_{3m} = tertiary current arising from incident particles reflected as neutral atoms from the target and striking the collector.

i^e_{3s} = tertiary current arising from sputtered particles striking the collector.

i_{bc} = incident beam current striking the collector.

i_{be} = current of secondary electrons escaping from the collector chamber.

i_{bi} = current of reflected ions (net) escaping from the collector chamber.

In this designation, the superscript i refers to ion currents and the superscript e to electron currents. Assuming a clean surface, so that $i^{i+}_x = i^{i-}_x = 0$ and that i_{bc}, i_{be} and i_{bi} are negligible, due to correct electrode design, we see that:

$$\frac{I_c}{I_b} = \frac{(i^{i+}_2 - i^{i-}_2) + (i^{i+}_s - i^{i}_s) + i^{i}_{th} - i^{e}_{th} - i^{e}_2 + (i^{e}_{3e} + i^{e}_{3i} + i^{e}_{3m} + i^{e}_{3s})}{i^{i}_1} \quad . \quad (2.3)$$

The sputtered particles from the target will have maximum energies not exceeding several tens of electron volts, and so will not release appreciable numbers of tertiary electrons from the collector, except by potential ejection. The latter will be usually quite small compared to the number released by kinetic ejection by the much more energetic reflected incident particles, which will have maximum energies in the kiloelectron volt range for these experiments.

The secondary electrons from the target will have mean energies in the vicinity of several electron volts and maximum energies not exceeding a few tens of electron volts. The proportion of high energy electrons is very small, however, as our later results will show. A retarding potential of 30 - 40 volts is ample to return nearly all secondary electrons to the target, and also, of course,

the thermally emitted electrons, which have energies of only a few tenths of an electron volts. It will also return any sputtered negative ions to the target, but will be insufficient to retard the particles reflected as negative ions. We can thus write, for the experimentally observed quantity 'R':

$$R = \frac{(i_2^{i+} - i_2^{i-}) + i_{th}^{i} + (i_{3i}^{e} + i_{3m}^{e} + i_{3s}^{e}) + i_s^{i+}}{i_1^{i}} , \qquad (2.4)$$

and, using similar arguments, write for γ' :

$$\gamma' = \frac{-(i_2^{i+} - i^{i-}) + i_{th}^{e} + i_s^{i-} + i_2^{e}}{i_1^{i}} . \qquad (2.5)$$

By adjusting the target temperature the thermal contributions i_{th}^{i} and i_{th}^{e} can be reduced to zero while still maintaining the target at a sufficient temperature to ensure cleanliness.

The SECONDARY ELECTRON EMISSION COEFFICIENT γ is defined as the number of electrons released from the target by each incident particle. Thus:

$$\gamma = \frac{i_2^{e}}{i_1^{i}} . \qquad (2.6)$$

The ION REFLECTION COEFFICIENT is defined as the fraction of the incident ions which are reflected from the target in a specified charge state. Thus:

$$\left.\begin{aligned} \rho_+ &= \frac{i_2^{i+}}{i_1^{i}} \\ \rho_- &= \frac{i_2^{i-}}{i_1^{i}} \\ \rho_m &= \frac{i_2^{im}}{i_1^{i}} \end{aligned}\right\} . \qquad (2.7)$$

In the last expression "i_2^{im}" is the "current" of neutral atoms reflected from the target.

The SPUTTERING COEFFICIENT is defined as the number of target particles in a specified charge state sputtered from the target by each incident beam particle. Thus:

$$\left.\begin{aligned} s_+ &= \frac{i_s^{i^+}}{i_1^i} \\ s_- &= \frac{i_s^{i^-}}{i_1^i} \\ s_m &= \frac{i_s^{im}}{i_1^i} \end{aligned}\right) \qquad (2.8)$$

We can now write:

$$R = (\rho_+ - \rho_-) + s_+ + \gamma_c , \qquad (2.9)$$

$$\gamma' = -(\rho_+ - \rho_-) + s_- + \gamma , \qquad (2.10)$$

where

$$\gamma_c = \frac{i_{3i}^e + i_{3m}^e + i_{3s}^e}{i_1^i} .$$

Writing

$$\gamma_c = \frac{i_{3i}^{e^+}}{i_2^{i^+}} \cdot \frac{i_2^{i^+}}{i_1^i} + \frac{i_{3i}^{e^-}}{i_2^{i^+}} \cdot \frac{i_2^{i^+}}{i_1^i} + \frac{i_{3s}^e}{i_s^{i^+} + i_s^{i^-}} \cdot \frac{i_s^{i^+} + i_s^{i^-}}{i_1^i} + \frac{i_{3m}^e}{i_{2m}^i} \cdot \frac{i_{2m}^i}{i_1^i} \qquad (2.11)$$

$$= \gamma_+ \rho_+ + \gamma_- \rho_- + \gamma_s (s_+ + s_-) + \gamma_m \rho_m ,$$

where γ_+, γ_-, γ_s, γ_m are the electron emission coefficients for the collector, we have

$$\gamma_c = \gamma_c'(\rho_+ + \rho_- + \rho_m) + \gamma_s(s_+ + s_-), \qquad (2.12)$$

assuming that the reflected particles all have the same energy distributions, so that

$$\gamma_+ \simeq \gamma_- \simeq \gamma_m \simeq \gamma_c' . \qquad (2.13)$$

We shall see later that the last assumption is not strictly true, but it is sufficiently accurate for the purposes of this discussion.

It can be seen that the measurement of the individual coefficients is

somewhat more involved than the simple observation of the quantities R and γ' in a simple 'collector' type electrode system. The quantity γ' is a tolerable approximation to the actual coefficient γ for many applications and the majority of researchers have tacitly assumed that $\gamma' = \gamma$, seeing that the other quantities in equation (2.10) are at least an order of magnitude smaller over the 5 - 50 keV energy range. On the other hand, R is a rather ambiguous quantity involving several terms of the same magnitude and it cannot be taken even as an approximate measure of any single coefficient.

In part 2 of this chapter, an attempt is made to investigate these matters in more detail and we shall now, for the sake of completeness, consider some experimental observations made on the quantities γ' and R, bearing in mind their correct definitions given above.

B. Preliminary observations made on the apparent secondary electron coefficient, γ'

A fresh target placed in the vacuum system exhibited an apparent temperature coefficient for emission of secondary electrons. This is a consequence of the desorption of contaminants from the metal surface upon heating, and is not an effect intrinsic to the metal itself. Figure 2.3 shows how γ' apparently drops by as much as 25% when the contaminated surface is moderately heated (to a dull red heat estimated to be $\sim 200^{o}$C).

Also shown is the sharp increase in the background pressure as the surroundings are heated, indicating a general contamination in the measuring chamber. Figure 2.4 indicates how γ' for Pt changes with time, as the target is suddenly heated to the moderate temperature given above and then, after several minutes, made cold again. For these observations, the pressure in the chamber, with the target cold, was about 10^{-7} mm, giving a mono-layer formation time of about 10 seconds from the background gas. As γ' continues to increase for up to several minutes after the 'hot-to-cold' point in Figure 2.4, the principal contamination must arise from a minor component of the background gas, possibly hydrocarbons.

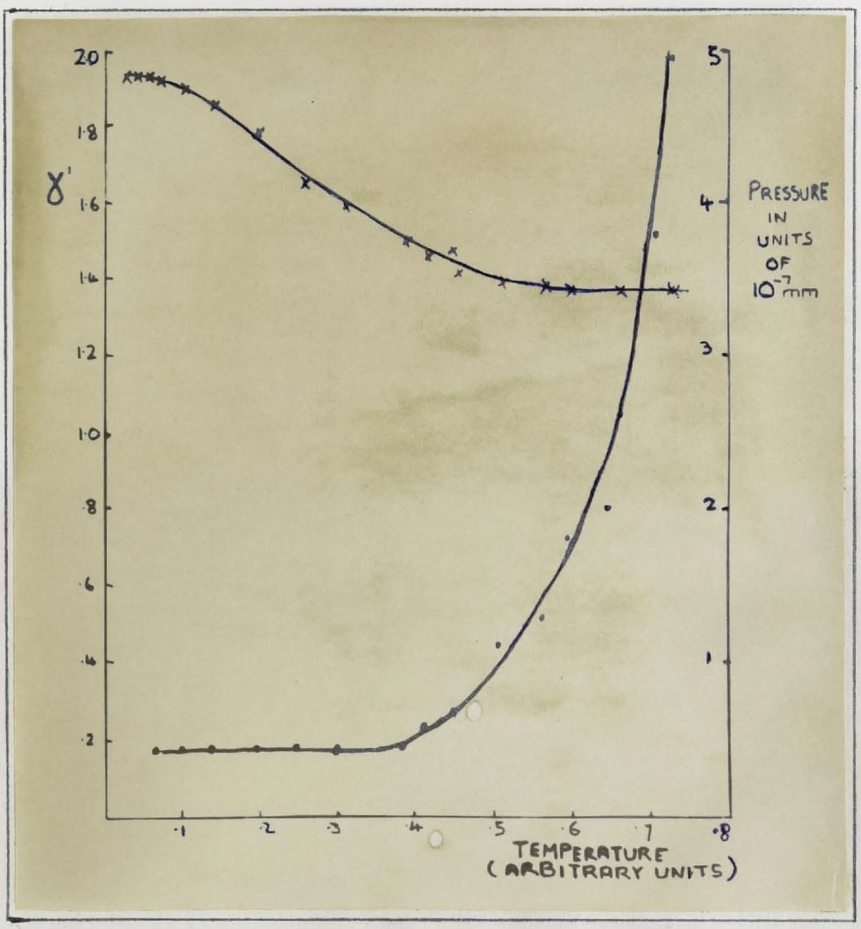

Figure 2.3

Effect of moderate heating upon the electron emission from a contaminated Pt surface.

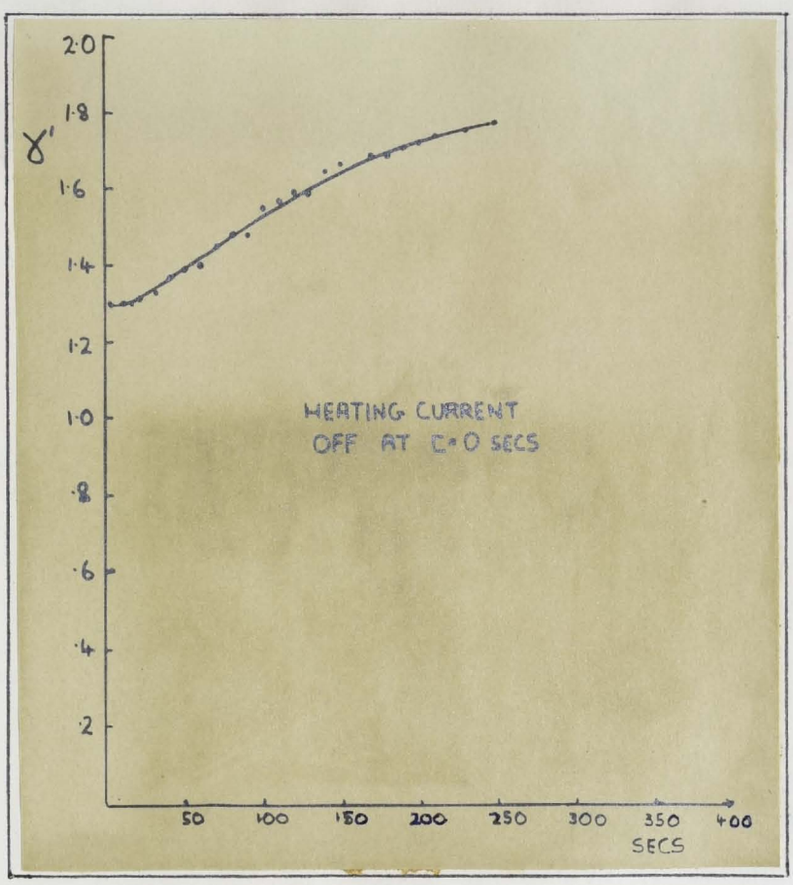

Figure 2.4

Effect of temperature reduction upon the electron emission from a contaminated Pt surface.

Figure 2.5 shows how the coefficient γ' apparently decreases with increase in the incident beam intensity from approximately 1 μ-amp/mm to 4 μ-amp/mm, for H_1^+ on a contaminated Pt surface at room temperature. The decrease is clearly due to the 'cleaning up' effect of the beam on the surface and not to any intrinsic cause. On the same figure is drawn in the observed variation for a hot ($\sim 220^{\circ}$ C) surface, showing that the 'cleaning up' effect is much reduced.

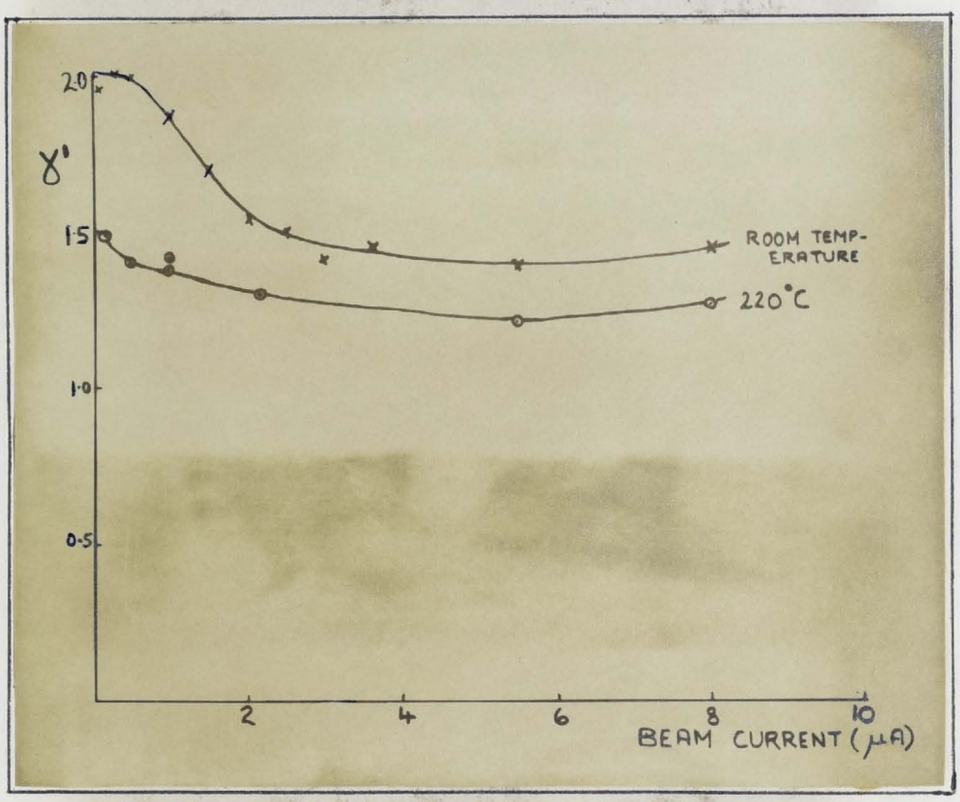

Figure 2.5

Effect of beam intensity upon the electron emission from a contaminated Pt surface.

From just these few results, one can appreciate the necessity for carefully controlled experimental conditions for observing emissions from surfaces. It serves little purpose to take measurements under an arbitrary set of experimental conditions and one of two approaches is required to obtain physically meaningful results in this field. One may:

(1) Closely monitor all variables in the system such as pressure, target temperature, beam current intensity, composition of background gas, etc., while varying one of these variables in a carefully controlled manner, or

(2) Take measurements only from an atomically clean target by operating at sufficiently low pressures or high target

temperatures, or a combination of both, to prevent any build up of contamination or gas on the surface during the course of the experiment.

The bulk of measurements in the present report are of the latter type. To obtain clean operating conditions the target was baked at a red heat for several days and then flashed at a bright white heat, close to its melting point, for about a minute. The latter flashing time was limited by the thermal stress on the metal-to-glass seals supporting the target. (Details of the detector chamber and target etc., are given later - section 2-2 A).

While the target was baking, the external walls of the detection chamber were heated with an electric hand torch. For the measurements of the total scattering, as described in this chapter, no attempt was made to bake the entire detection chamber uniformly to a high temperature. Nevertheless the background pressure in the chamber fell to $\sim 10^{-8}$ after the target was baked for a few days, even with the latter at red heat. Under working conditions with the beam incident on the target, the pressure in the detection chamber increased by about 100 per cent to $\sim 2 - 3 \times 10^{-8}$. (Pressures here are in millimetres of mercury.)

The properties of a properly cleaned surface were drastically different from those of a contaminated surface. There was now no detectable temperature coefficient for γ' over the entire temperature range from room temperature up to a white heat. This certainly indicated that the surface was free of volatile contaminants and absorbed residual gases for the duration of the experiment, although the presence of non-volatile contaminants such as carbides, nitrides, etc., could not be ruled out, on the basis of these observations alone. The energy distributions for the secondary electrons, however, did seem to change slightly with temperature as the retardation characteristics for a stainless steel target at two differing temperatures (corresponding to about 800° C and 1000° C) indicated in Figure 2.6. The higher temperature characteristic has a greater proportion of high energy electrons, although the situation is somewhat confused by the presence of positive ions from the target at the higher retarding voltages.

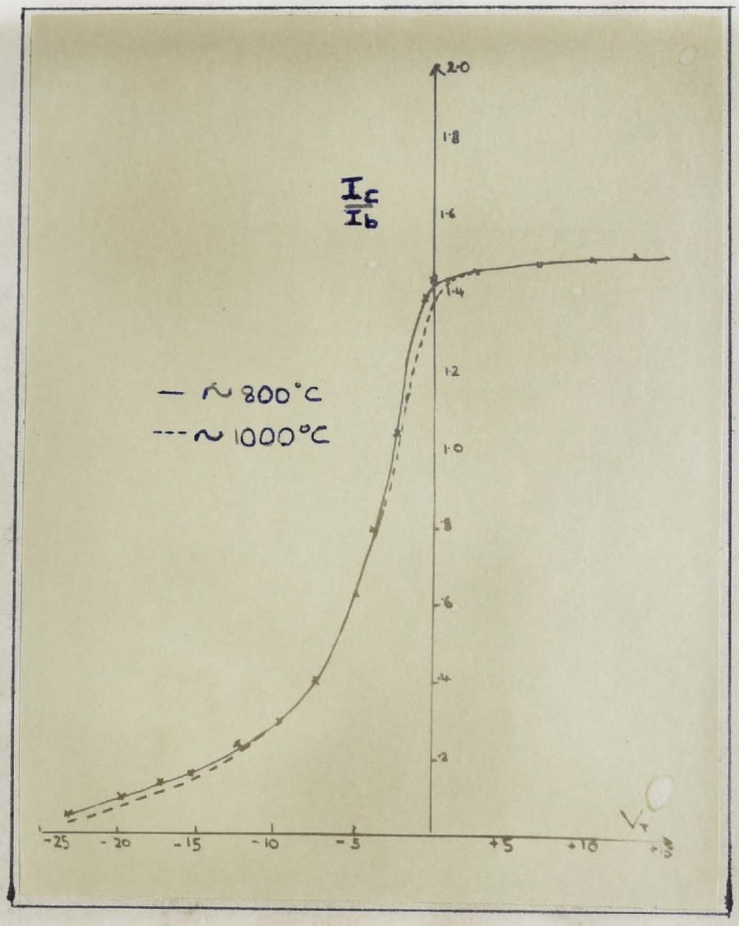

Figure 2.6

Retardation characteristics for a clean stainless steel target at two temperatures.

For a clean surface there is no apparent change of γ' with beam intensity for H_1^+ over the range 0 to 4 μ-amp/mm^2, although γ' for H_3^+ does decrease slightly (by about 6%) as the beam intensity increases from very small values up to .2 μ-amp/mm^2 (Figure 2.7). It is difficult to understand this decrease in terms of a 'cleaning up' phenomenon, as there is no indication of it for H_1^+, and it may be somehow involved with the beam composition. All measurements of γ' for H_3^+ were done in the range of beam intensities where the coefficient was independent of beam intensity.

All observations on a 'clean' surface were usually performed with the target at red heat, or shortly after cooling it to room temperature. The target upon cooling to room temperature, was found to adsorb residual gas from the chamber and thus became contaminated after several minutes, even with a background pressure of 2 - 3 x 10^{-8} mm. This is clearly shown in Figure 2.8,

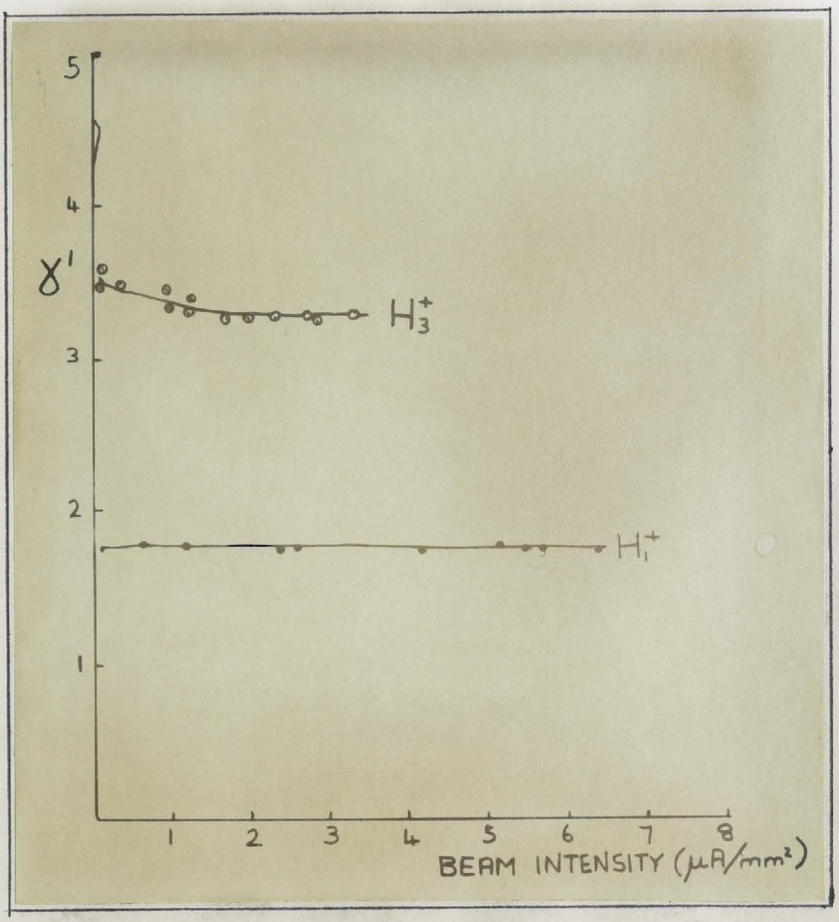

Figure 2.7

Effect of beam intensity upon the electron emission from a clean Pt surface.

where γ' is plotted against the time in seconds after the beam is switched on for both a red hot and a cold (for five minutes) Pt target. The emission for the cold target is consistently slightly higher than for the hot target. Figure 2.8, however, shows a much more interesting effect. In both bases the observed emission actually drops by $\sim 6\%$ initially, reaching a minimum about 4 - 6 seconds after the beam is turned on. These observations were taken with the aid of a double beam oscilloscope where the traces for both the total currents to the target and collector were recorded on photographic plate. Figure 2.9 sketches the experimental arrangement and some typical traces are shown in Figure 2.10.

The traces in Figure 2.10 are for a 10 keV proton beam incident on a stainless steel target at red heat. The sweep frequency of the oscilloscope was 2 sec/cm and, as the oscillograph indicates, the beam was incident for

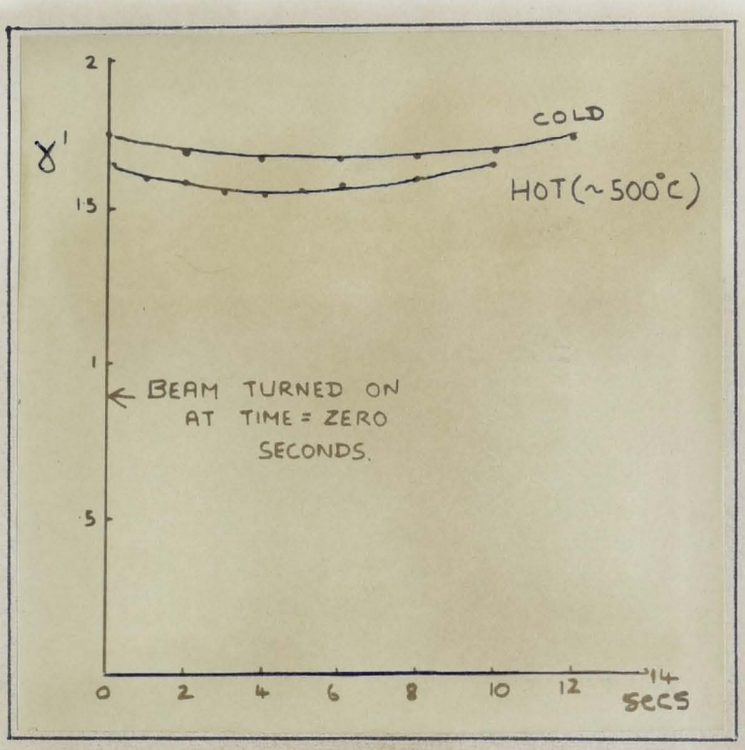

Figure 2.8

Change of emission with time after a proton beam strikes a Pt target at 30 keV.

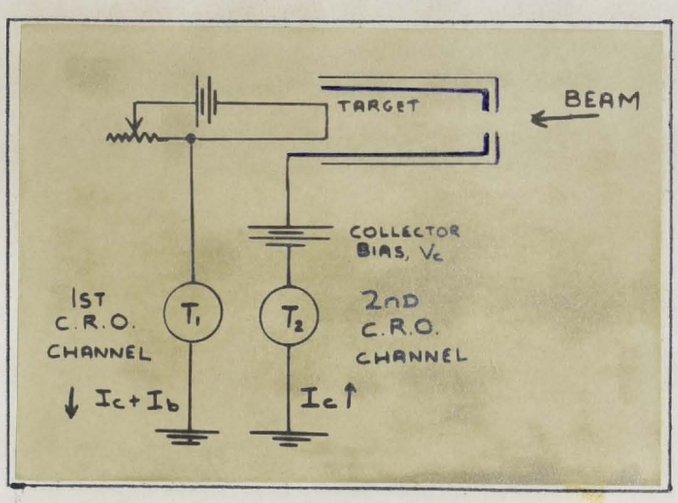

Figure 2.9

Electrode system and measuring circuit for observations employing the double beam oscilloscope.

approximately 15 seconds on the target. As the amplification factors for each beam were the same, we have:

$$\frac{d_c}{d_t} = \frac{I_c}{I_c + I_b} \qquad (2.14)$$

and thus,

$$\gamma = \frac{I_c}{I_b} = \frac{d_c}{d_t - d_c} \quad , \tag{2.15}$$

where d_c and d_t are the deflections in scale graduations, due to the collector and target currents respectively.

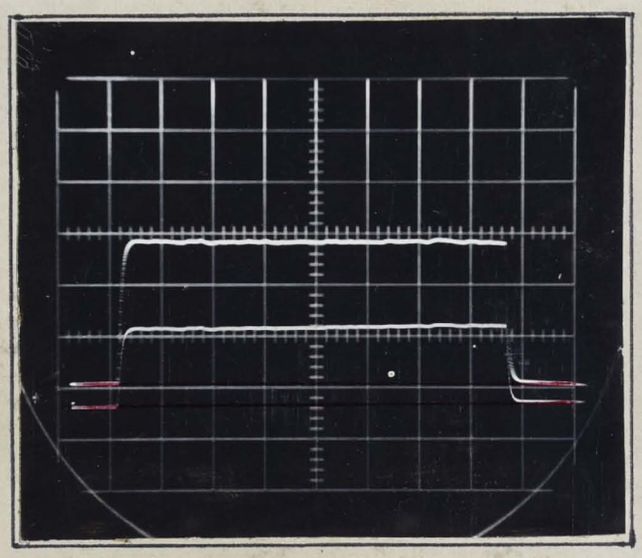

Figure 2.10

Traces for electron emission from a stainless steel target bombarded by 10 keV protons.

Figure 2.11 shows the variation in γ' over the first fifteen seconds after the beam strikes the target, for both 10 keV and 45 keV incident proton energies. (The 10 keV variation was plotted from the oscillograph in Figure 2.10). As with a platinum target, there is an initial drop in the coefficient with a minimum 5 seconds after the beam strikes the target. The percentage decrease is only about 3% in this case however.

It is difficult to explain this effect and it is nowhere referred to in the current literature. At higher pressures (exceeding $\sim 10^{-6}$ mm) there is no sign of it and there are apparently two pre-requisites necessary for detecting it:

(1) A very good vacuum and clean surface (free from gross contamination, although not necessarily of some adsorbed gases, as indicated in Figure 2.8).

(2) A current measuring instrument with a rapid response time to accurately record the currents over the first few seconds after the beam 'comes on'.

The deflections d_c and d_b were carefully measured using a movable magnifying lens attached to a graduated vernier scale. From Figure 2.11, we see that the coefficient steadies out to a constant value after 12 - 15 seconds as expected for a hot (clean) metal surface.

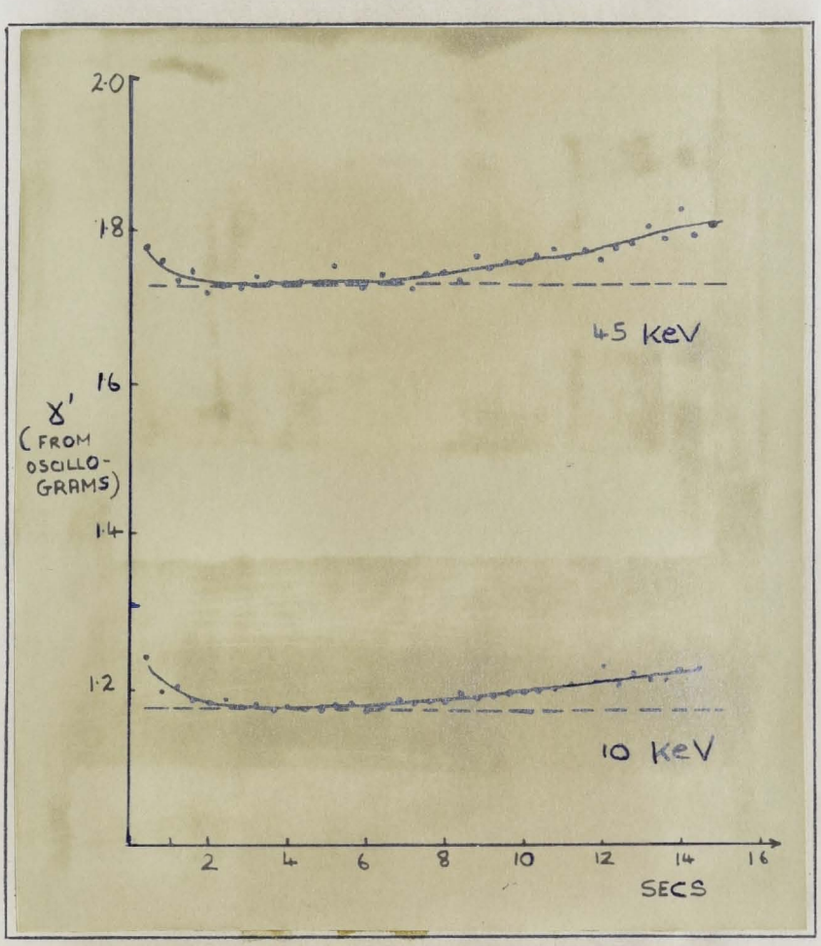

Figure 2.11

Change of emission with time after beam strikes target for proton bombardment of a stainless steel target at two energies.

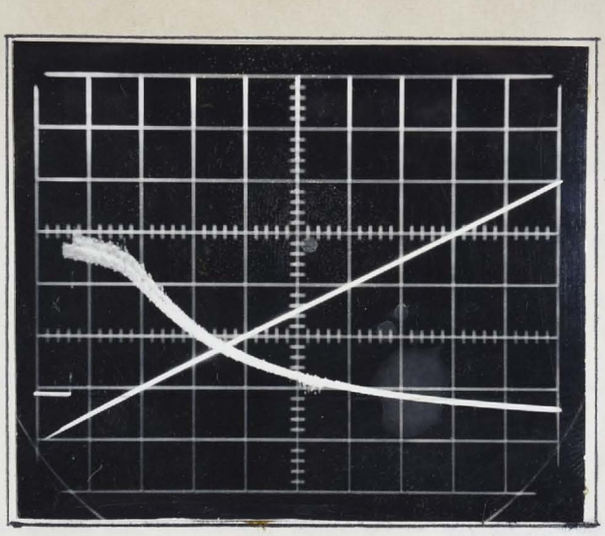

Figure 2.12

Traces for electron retardation characteristics for a hot and cold Pt surface. Proton bombardment at 30 keV.

Figure 2.12 shows electron retardation characteristics taken on both a hot and a cold surface. The linear trace represents the target bias which was swept uniformly from - 2.5 to + 27.5 volts (utilizing the sawtooth output from the CRO). Here the resolution of the traces was not sufficient to reveal any difference between the 'hot' and 'cold' traces at the higher retardation voltages, but adsorbed gases on the cold surface (as revealed by the larger apparent value for γ') may compensate for any real temperature effect. The collector current is applied about a second after the collector trace begins in order to obtain a well defined null line. The characteristics cross the axis at about + 22 volts, due to positive ions.

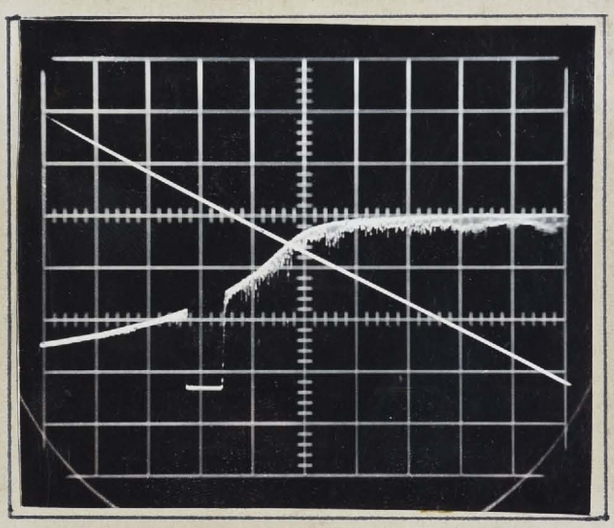

Figure 2.13

Trace showing typical voltage-current characteristic for a cold Pt surface. Proton bombardment at 30 keV.

Figure 2.13 shows a typical voltage-current characteristic, also for a Pt surface (cold). The great advantage of this method of measurement is that a characteristic can be recorded in a matter of seconds, rather than the hour or so required by conventional current measuring methods involving meters. Over the short time required to perform the experiment with an oscilloscope, the incident beam can be assumed to remain constant, so that a point-by-point normalization is not necessary. In recording the trace in Figure 2.13, the sawtooth output from the CRO was applied to the collector in series with a bias voltage to shift the zero field point to near the centre of the trace. The beam

is turned off for about a second during the recording of the trace, in order to obtain the null line. (The target trace in Figure 2.13 does, of course, contain a contribution from the incident beam as well as the collector current.)

Returning now to work performed with the meter circuit shown in Figure 2.1, we plot, in Figures 2.14 and 2.15, the variation in γ' with the total incident beam energy for platinum and stainless steel targets, over the energy range 4 - 50 keV. Variations for all the hydrogen ion species, H^+, H_2^+ and H_3^+ are shown. The continuous curves are for clean surfaces (that is, they conform to the criteria discussed above for surface cleanliness) while, for purposes of comparison, results for a partially contaminated platinum target are also included in Figure 2.14 (dotted curve).

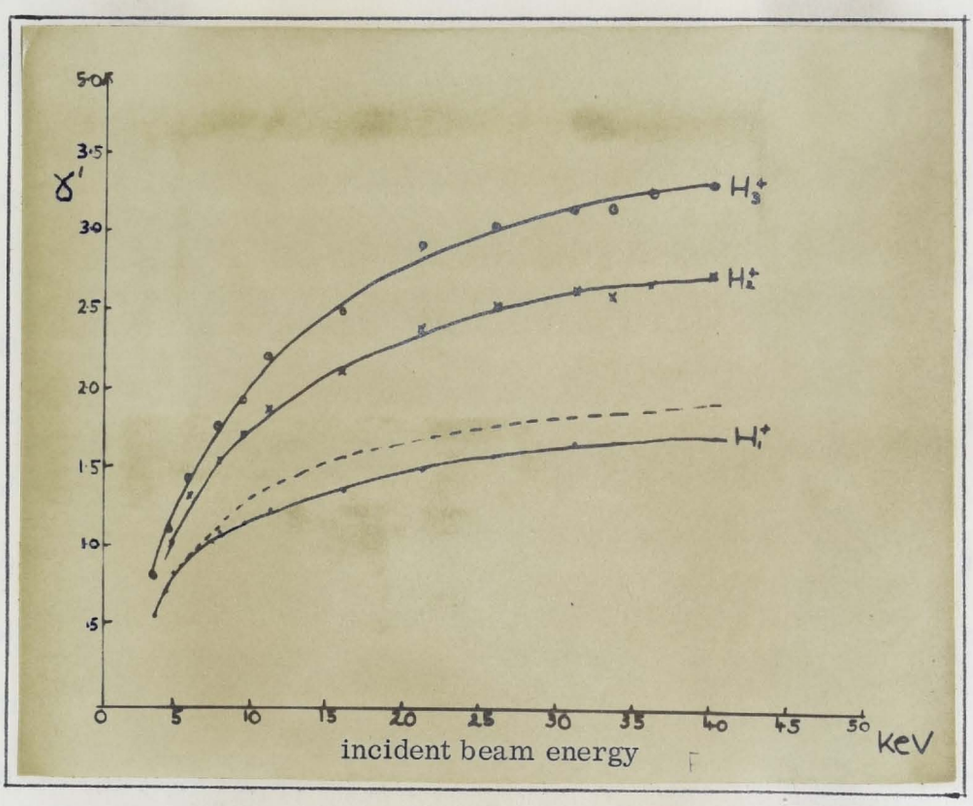

Figure 2.14

Variation of γ' with incident beam energy for a Pt target, 4 - 40 keV. Result on contaminated target shown dotted.

The variation of γ' with E, the incident beam energy, has been investigated by numerous researchers over the medium energy range in recent years, for a wide range of targets and incident beam species. The clean targets have $\gamma'(E)$ functions, which vary $\sim$ as $\sqrt{E}$ for energies less

than 20 - 25 keV, but tend to level off to a shallow maximum at energies well above the range of the present experiments. The coefficient γ' can be considered as the sum of potential and kinetic contributions, so that,

$$\gamma' = \gamma'_{kin} + \gamma'_{pot} . \qquad (2.16)$$

These processes, which are quite distinct, are discussed in some detail in the first chapter. Potential emission of electrons is, to a first approximation, independent of energy and usually predominates up to about a kilovolt after which kinetic emission commences and increases rapidly. At energies exceeding several keV, the kinetic emission exceeds potential emission by at least an order of magnitude. The threshhold energies for kinetic emission are too low to reach with the apparatus employed in this work, but extrapolation of the curves in Figures 2.14 and 2.15 would seem to indicate a value of $\sim$ 1 keV.

The values of the coefficient increase in the ion order H_1^+, H_2^+, H_3^+ at all incident beam energies and the figures would imply a convergence near the threshhold for kinetic emission. At the moment, there is little experimental data available on the detailed behaviour of γ' for light ions at near-threshhold energies, and so the properties of γ'_{kin} cannot be entirely separated from those of γ'. Still, it can be deduced from Figures 2.14 and 2.15 that the curves for the three ion species on each target, can be made to fall closely together by plotting the emission per particle against the energy per particle. This confirms the observations made by many researchers that the molecular ions dissociate upon striking the surface, into atomic components, which behave as individual particles. Thus, for example, a H_2^+ ion at 20 keV, dissociates into the two components H_1^+ and H^o at the surface, each with an energy very close to 10 keV. As the total emission from both particles is about twice that observed for H_1^+ alone at 10 keV, the inference is that the singly charged and neutral particles have the same, or nearly the same, electron emission coefficients.

Figure 2.14 for platinum, shows that a contaminated surface gives a higher emission over the energy range, the divergence increasing with incident beam energy. The beam intensity employed in taking these curves was only of the order of 0.05 μ-amp/mm^2 and, as Figure 2.5 indicates, this is well below that required to clean the surface by bombardment cleaning. As we have pointed out, surface cleanliness was assured in these experiments, by working at low pressures and generally high surface temperatures, and not by beam bombardment. Indeed, a too intense beam had the undesirable effect of raising the background pressure in the measurement chamber several-fold. (At a pressure of 10^{-8} mm, there are 3.3×10^{11} particles/litre, while a microamp beam conveys $\sim 10^{13}$ particles/sec. into the measuring chamber, which has an estimated volume of about 12 litres).

C. Preliminary observations made on the ion scattering coefficient, R

Accompanying the above measurements on the apparent secondary electron coefficient γ', the following observations were made on the ion scattering coefficient, R. We saw in section 2-1 A of this chapter, that R is an ambiguous quantity defined from equation (2.9), but it is worth while to investigate it in some detail as a supplement to our work on the energy distributions of the scattered ions, to be reported in Chapter IV, and also because it has been measured by many researchers with somewhat inconsistent results.

The electrode arrangement is that shown in Figure 2.1. The collector bias was made sufficiently negative to give a constant value for the normalized collector current, $\frac{I_c}{I_b}$, which was then designated as 'R'. Systematic observations on R are reported in section 2-2 B of this chapter and so only some informative preliminary results on the electrode system in Figure 2.1 are reported here.

Figures 2.16 and 2.17 show the variation of R with the incident beam energy for a platinum and stainless steel target respectively. One sees that the values of R are quite high, reaching 0.8 for H_3^+ on Pt at about 20 keV incident

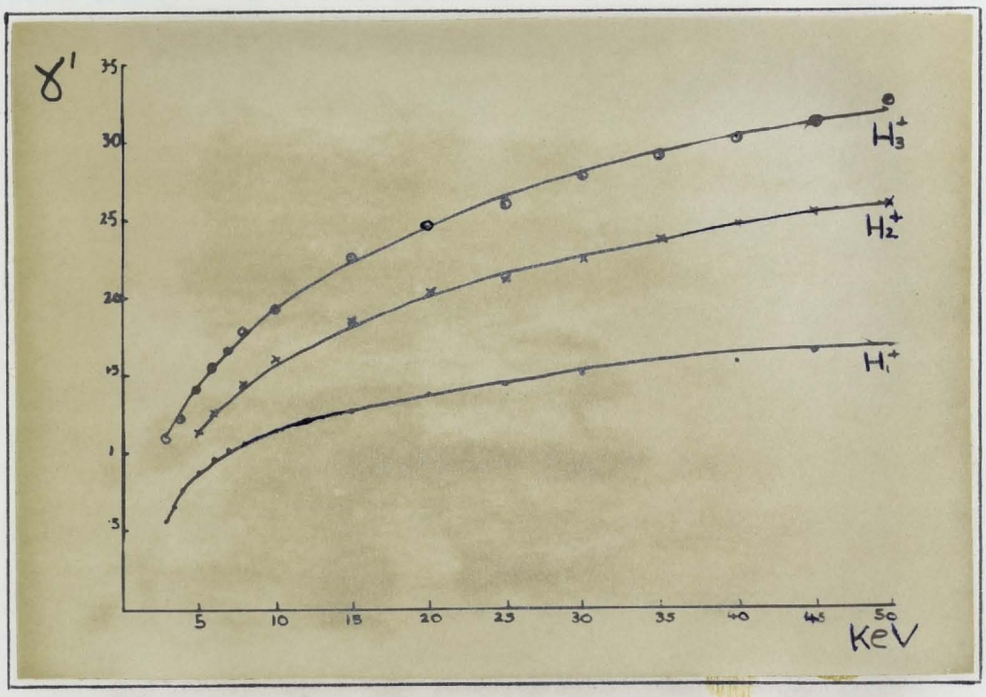

Figure 2.15

Variation of γ' with incident beam energy
for a clean stainless steel target, 4 - 50 keV.

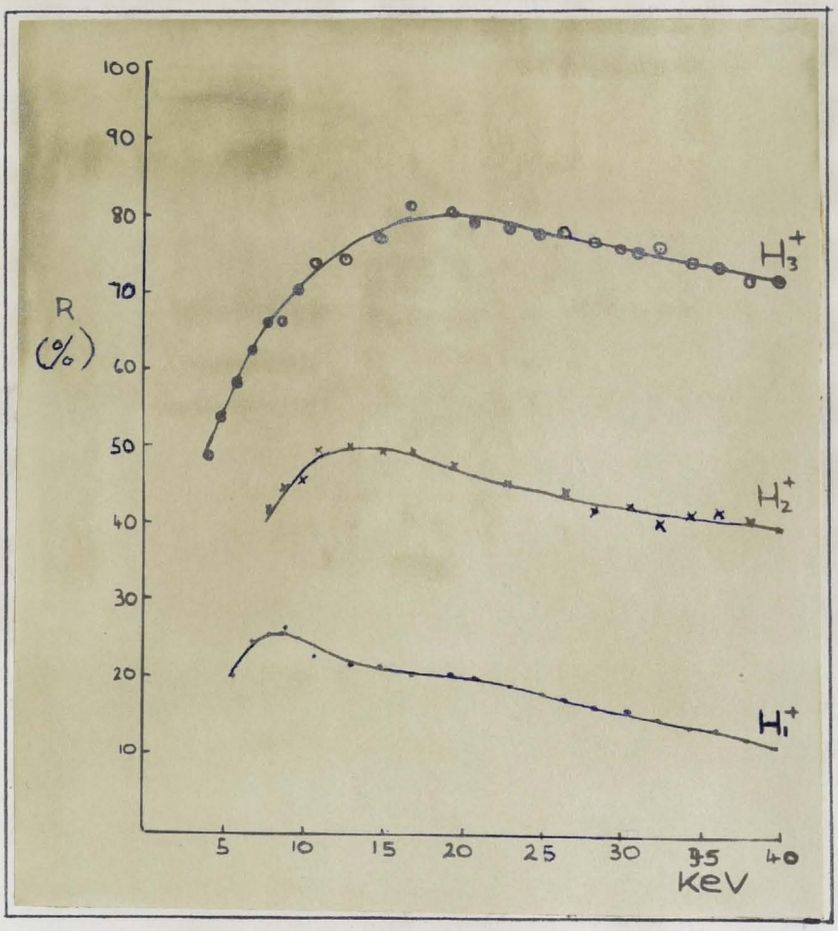

Figure 2.16

Variation of R with incident beam energy
for a clean platinum target, 4 - 40 keV.

beam energy. These measurements were taken on red hot targets, satisfying all the criteria for cleanliness discussed in section 2-1 B. As with electron emission, we cannot fully interpret this data, without reference to measurements taken at energies less than $\sim$1 keV, but some general observations are possible. Again the emission curves for the three ion species can be made to fall closely together by plotting the emission per particle against the energy per particle. This further confirms our observation made from the electron emission data, that the individual components of the molecular ions behave as discrete particles upon striking the target. While the electron emission characteristics continue to increase monotonically over the energy range covered, the ion emission coefficient, R, shows a very well defined maximum. For the platinum target, this maximum occurs at nearly the same velocity for all three incident ion species, as illustrated in the emission versus ion velocity curves in Figure 2.18. These velocity curves would seem to suggest the existence of a change in slope for R (H_1^+) at about 2×10^8 cm/sec., although this is not evident in the R (H_2^+) and R (H_3^+) characteristics. For the stainless steel target, the maximum occurs at a much lower incident ion energy, and so is not so clearly distinguished as it is for platinum.

The similarity of the scattering curves in Figures 2.16 to 2.18 to sputtering yield curves obtained by conventional sputtering techniques, have led several researchers to attribute the collector current principally to sputtered target ions[30]. This proposition will be critically examined in Chapter IV, in the light of our subsequent work, to be described. As with sputtering yield curves (section 1-3), the values of R initially increase quite rapidly with incident beam energy to the maximum, and then decrease more slowly at higher energies. The difficulty is that careful investigations have shown that the yield of sputtered ions under our experimental conditions, are at least two orders of magnitude less than the values of R indicated in Figures 2.16 to 2.18 for lighter ions. More will be said about this later.

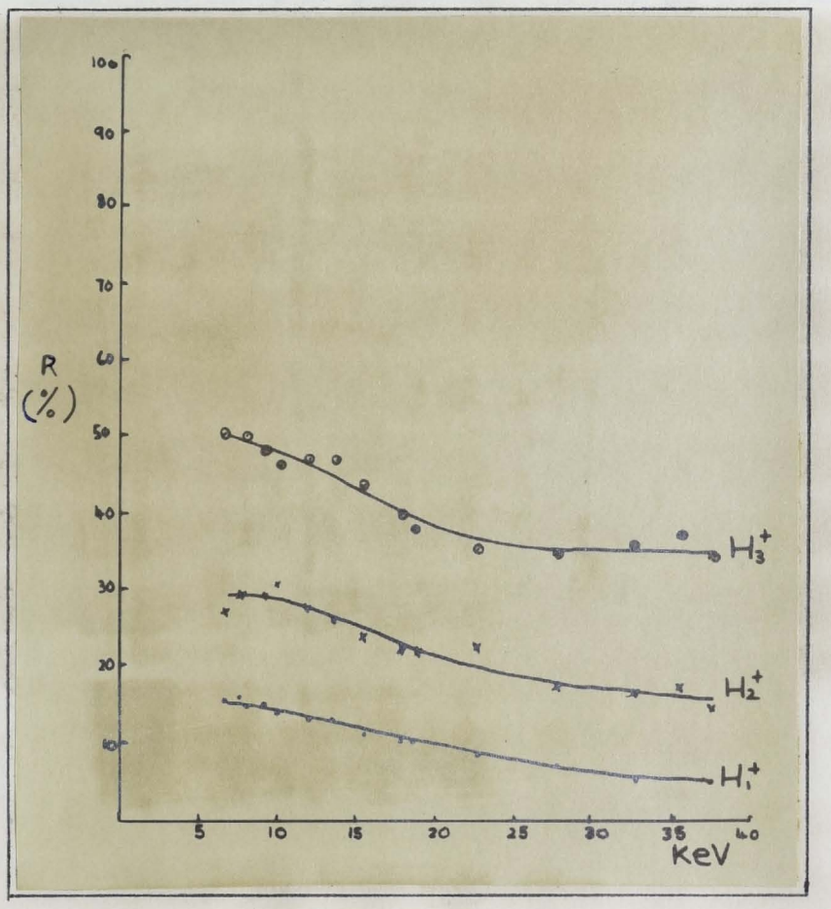

Figure 2.17

Variation of R with incident beam energy
for a clean stainless steel target, 5 - 40 keV.

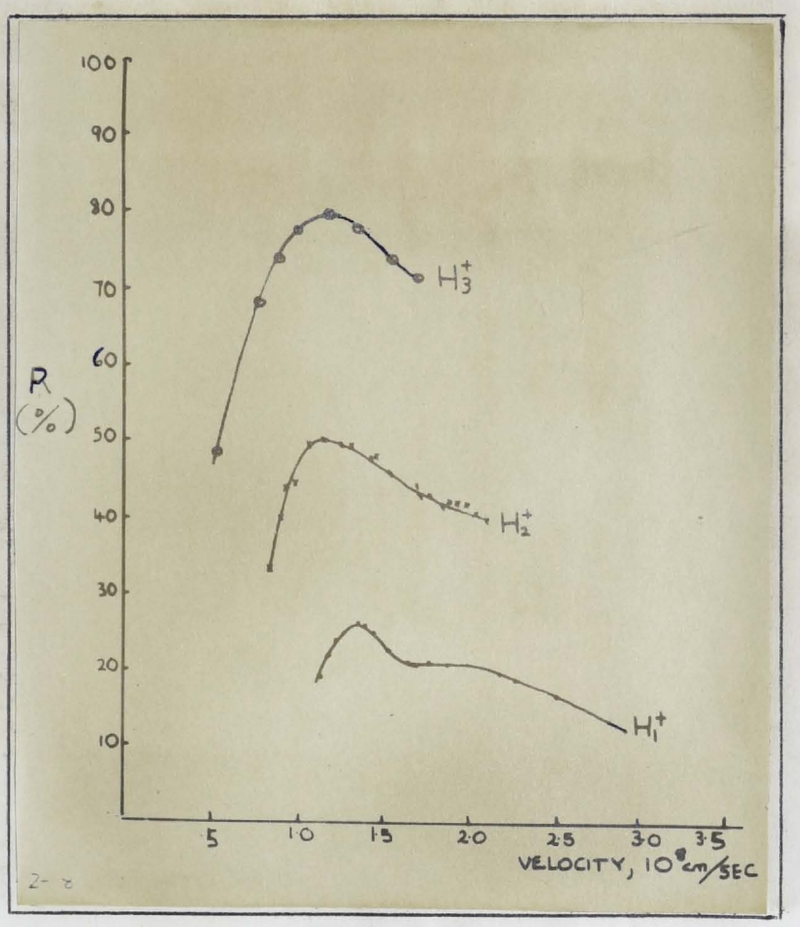

Figure 2.18

Variation of R with incident ion velocity
for a clean platinum target.

Figure 2.19 shows the dependence of R upon the target temperature for H_1^+, H_2^+ and H_3^+ incident at 23 keV on a platinum target. The target temperature, measured with an optical pyrometer, is increased from 200°C up to 1000°C. One sees that R remains constant with target temperature to a first approximation, although there is some indication of a maximum at several hundred degrees. This is probably due to the desorption of some residual gas trapped in the metal lattice, or desorbed on the surface, not to any real temperature variation of R with temperature. For a contaminated surface (dotted curve) the effect is much more pronounced, indicating that it is associated with cleaning up or desorption of gas from the target. At higher temperatures the values of R for the clean (or nearly clean, as it seems) and contaminated surfaces, approach each other as expected. This provides us with another means of estimating the surface cleanliness of the target. The minimum target temperature for complete desorption of gaseous impurities is clearly about one thousand degrees. The target can be maintained at this temperature for the duration of an experiment, e.g., for taking the curves in Figures 2.16 and 2.18; however, the target cannot be maintained at higher temperatures for extended periods without placing excessive thermal stress

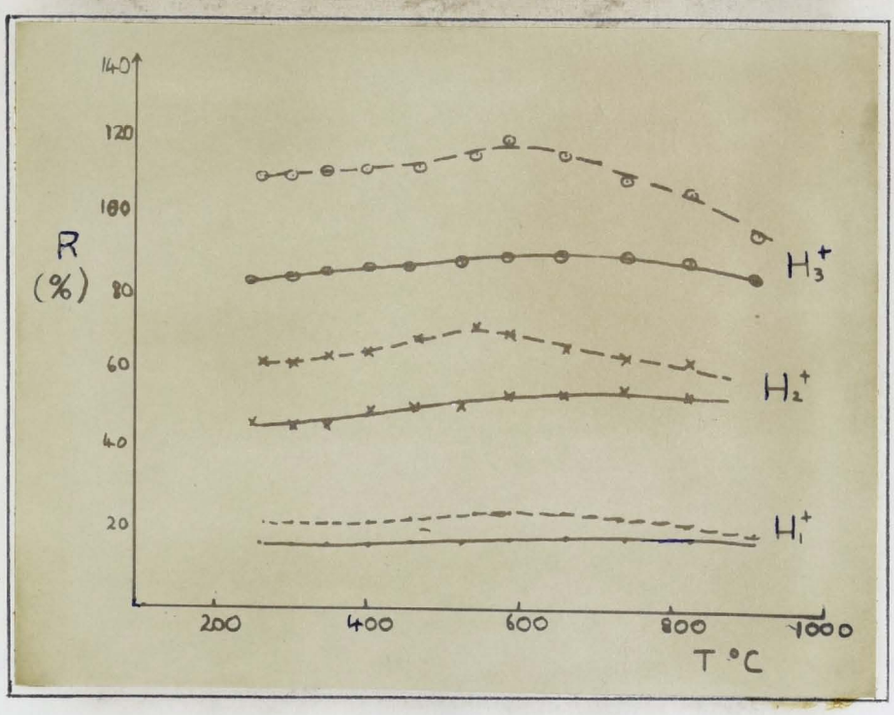

Figure 2.19

Variation of R upon target temperature
for clean and contaminated platinum targets.

upon the metal-to-glass seals supporting the target. Also, the current of thermally emitted ions increases sharply at target temperatures much exceeding 1000^{o}C. Nevertheless the target can be flashed to as high as 1500^{o}C for several seconds and, indeed, this seemed to be a necessary procedure to efficiently clean the target. Heating to a red heat ($\sim 1000^{o}$C), while sufficient to remove adsorbed gases from the target surface, did not suffice to remove the less volatile contamination from a newly installed target.

Figure 2.20, showing the variation of R with incident beam intensity, for H_1^+ and H_3^+ beams on platinum, are similar to those for the electron coefficients, Figure 2.7. For H_1^+ there is no detectable change, but with H_3^+ there is an initial decrease of several per cent. As suggested in the electron case, this latter effect is probably a result of a change in beam composition rather than to some change in the beam-metal interaction. For example, if the proportion of neutral atoms in the incident particle flux increases as the beam proper is defocussed, the result would be an apparent increase in the emission coefficients. We noted above that a neutral H^o particle gives an emission very close, at least, to that of the ion H_1^+ at the same energy. The background flux of H^o would arise from charge-changing collisions along the path of the ion beam past the bending magnet, and we would expect these to be much more probable for H_3^+ than for H_1^+, due to its lower velocity and higher ionization potential. Thus we have an experimental test on the proportion of neutrals in the incident beam flux. Our data indicate that the fraction of neutrals becomes significant only at very low beam intensities of the molecular ions.

Double beam oscilloscope experiments with ion emission revealed no initial 'dip' effect, as observed for electron emission (Figures 2.8 and 2.11), for any combination of experimental conditions. Figure 2.21 shows the variation in the ion emission coefficient, R, over the first several seconds after the beam 'comes on' at t = 0 seconds, for H_1^+ on a platinum target. The target heaters

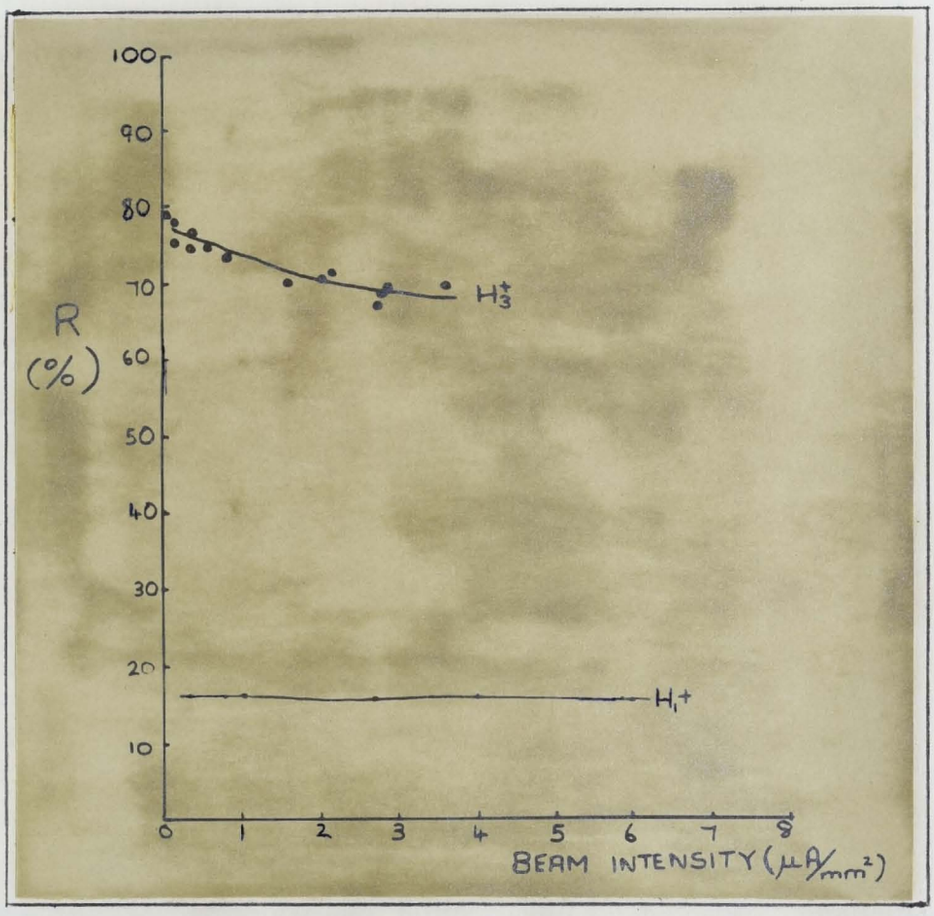

Figure 2.20

Variation of R with incident beam intensity
for a clean platinum surface.

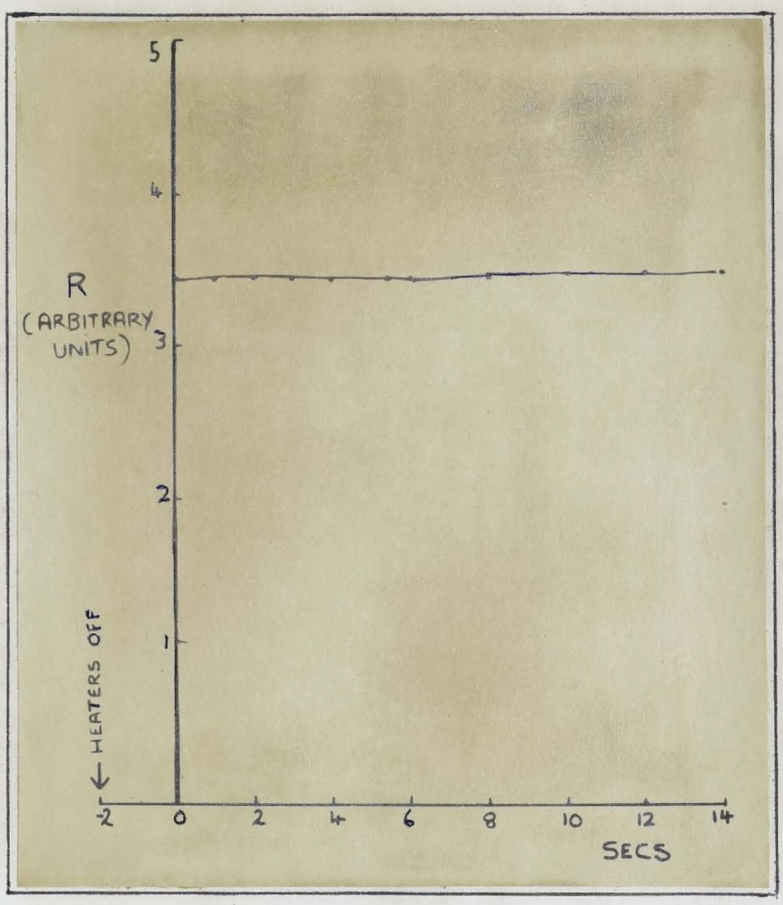

Figure 2.21

Variation of R with time after beam strikes surface.

were turned off at time t = - 2 seconds. R is seen to remain constant for up to t = 14 seconds at least. There is no indication of a minimum at t ~ 5 seconds, as occurs with electron emission. The oscillograph from which Figure 2.21 is plotted is shown in Figure 2.22. The shift in the zero of the trace at about t = - 2 seconds in the oscillograph, coincides with the cooling of the target and thus can be attributed to the presence of thermally desorbed ions from the hot (~1000^{o}C in this case) platinum target. It can be seen that, upon switching off the target heaters, the emission of thermal ions drops exponentially to zero, in contrast to the instantaneous drop when the beam is turned off at about t = 15 seconds. Arifov[28] has investigated this in considerable detail and it is clear that, in principle, the oscillographic method provides a powerful technique for the investigation of surface processes. An oscillograph trace can be recorded in a matter of seconds, whereas the use of current measuring meters (conventional technique) requires at least a full half-minute per point. An oscillograph has the advantage of being a continuous, rather than a point-by-point determination and thus is more sensitive to small signal variations. In addition, the random variations in the beam are less likely to be significant during the several seconds required to record the trace and the beam can be assumed steady over this period.

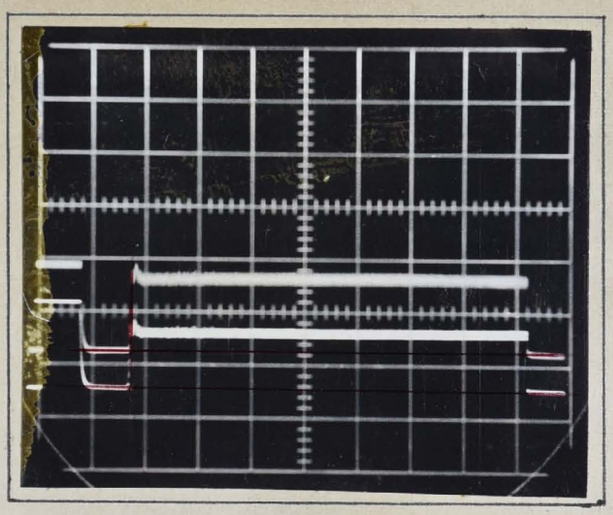

Figure 2.22

Traces for positive ion scattering from a platinum target, 40 keV incident beam energy.

Also, the target can be maintained at a temperature of 1300 - 1400°C for this length of time without excessive thermal stress on the target connections, enabling various surface characteristics to be investigated over a broad range of temperature. Moreover, the 'zero' is simply obtained by momentarily turning the beam off during the recording of the trace and is irrespective of the presence of thermal ions or electrons (provided that the thermal current is not more than six or seven times the secondary current, otherwise the deflection of the trace, due to the latter, becomes difficult to measure accurately).

2-2 Systematic Observations on the Emission Coefficients

A. Apparatus for measuring the real secondary electron coefficient, γ

Most experiments on the secondary emission of electrons have, in fact, measured the quantity γ', defined in equation (2.10). Reliable measurements of the real emission, γ, as defined in equation (2.6) are complicated by the presence of scattered ions of both signs. To repel the positive reflected ions requires a positive bias on the collector of the same order as the incident beam energy, and will not remove ions carrying a negative charge. Another factor not discussed in section 2-1 A is the generation of X-radiation from the collector by high velocity electrons striking it, this radiation then rejecting further electrons from the target. (This effect, however, is probably not appreciable, as our work on energy distributions indicates that very few electrons have energies exceeding several tens of electron-volts).

The use of electric fields alone will not differentiate between electrons and negative ions and time-of-flight methods are unsuitable, due to the velocities being of the same order of magnitude. The technique employed in the present experiments employed a magnetic field to channel the electrons into a faraday cup, without corresponding action upon the ions. This minimizes the complications due to the ions of either sign.

Figure 2.23 is a schematic diagram of the apparatus. As with the preliminary measurements described earlier in this chapter, the target, T

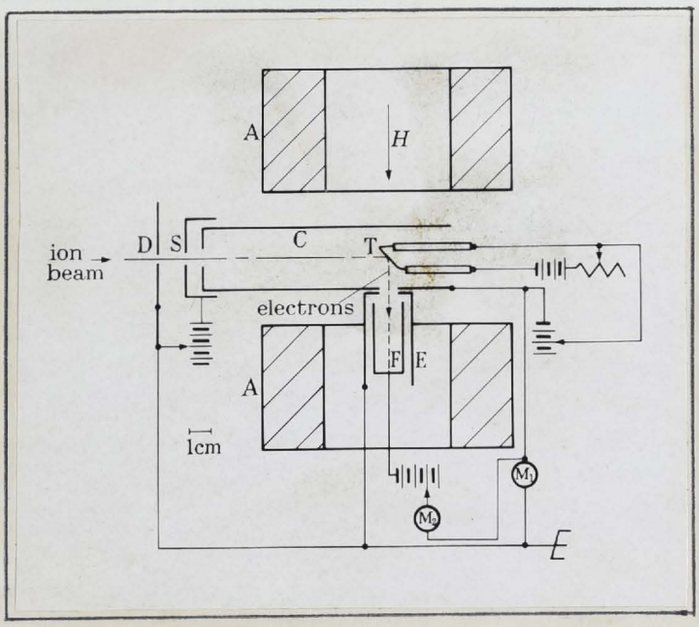

Figure 2.23

Schematic diagram of apparatus for measurement of secondary electron emission.

consisted of a strip of metal foil a few thousandths of a centimetre in thickness, which could be heated electrically, and which could be given a suitable bias with respect to the surrounding cylindrical electrode C (hereafter referred to as 'the collector'). The target was inclined at 45^{o} to the incident beam, for reasons which will become clear later in this discussion. In front of the collector, C, was another electrode, S, maintained a few volts negative to suppress secondary electrons originating from the aperture, D, or from further down the system. The diameter of D was sufficiently small to ensure that none of the beam struck either S or C. A hole 0.6 cm in diameter was cut in C, so that a line joining the centre of this hole to the point on the target struck by the beam, was normal to the beam, and a faraday cup, F, was placed with its open end facing this hole in the collector. The cup, F, was enclosed by a shield, E, at earth potential and maintained at a suitable positive bias to prevent the escape of slow electrons. The coils, A, then applied a magnetic field, H, which was ideally along the line joining the spot where the beam hit the target to the axis of the faraday cup (hereafter referred to as the transverse direction).

As the transverse field, H, was increased, an increasing fraction of the secondary electrons from the target entered the faraday cup, due to the

combined effects of the electric field applied between T and C and the magnetic field. We will see later that very few secondary electrons are emitted with energies above about 50 eV and, in a magnetic field of 300 gauss, they will nearly all have radii of revolution much less than a millimetre. Thus they were swept away from the neighbourhood of the target before recapture and spiralled along the lines of H into the faraday cup. Ions of either sign had a much larger radii, both by virtue of their larger energies and much heavier masses, and very few escaped through the hole in C to reach the cup. Measurements showed that, with a 4.5 volt negative potential on C, the positive current to F, with a 300 gauss transverse field, was only 2% of the positive current to C. From this, and the relative values of the electron and ion emissions from the target, the ionic contribution to the current at F could not have exceeded 0.2%. Thus, one could measure the current of secondary electrons free from complications arising from the presence of ions, radiation from C, etc.

Figure 2.24 illustrates the changes in the collector and faraday cup currents as the transverse magnetic field is increased, for 22 keV H_1^+ on a hot ($\sim 1000^{o}$C) platinum target. At a field value of about 300 - 400 gauss, the

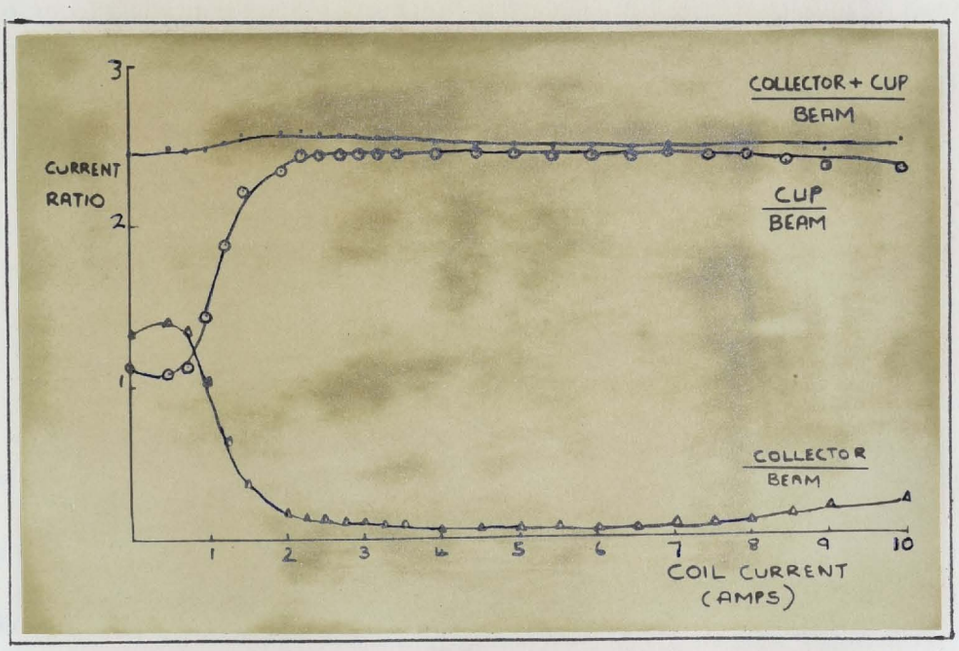

Figure 2.24

Effect of transverse field on currents to cup and collector.

collector current had dropped to a very small, but measurable, negative value, while the cup target had saturated. The small residual negative current to the collector is difficult to interpret as perhaps one might have expected it to be slightly positive (see Figure 4.15, Chapter IV). There might possibly have been some slight misalignment of the fields and the increase in the residual collector current as H is increased above 500 gauss, can certainly be attributed to the deflection of the incident beam from the central position designated X in Figure 2.23. Thus the beam was no longer precisely normal to the field, H, as required for optimum alignment. At 300 - 400 gauss field, however, at least 98% of the secondary electrons reached the cup and certainly no ions contributed significantly to the cup current, which was the most important consideration.

The pressure in the collision chamber was approximately $2 - 4 \times 10^{-8}$ mm under working conditions, and was measured on a B-A gauge attached directly to the system (see Appendix). All systematic observations were made on red hot targets. Each target was flashed to a white heat (of at least 1200°C) prior to the observations, until reproducible results were obtained and until there was no apparent temperature coefficient for electron emission. The beam intensity was $0.15 - 0.5\ \mu A/mm^2$ and the results were independent of beam intensity over this range. Experimental details pertaining to target cleanliness etc., are discussed in more detail in section 2-1 and so are not reiterated here.

B. Results for systematic measurements on the secondary emission coefficient γ

Figure 2.25 summarizes the measured results for the variation of γ with incident ion energy for the bombardment of polycrystalline nickel, molybdenum, tantalum, platinum and also of reactor grade graphite, for incident ions of hydrogen, deuterium, helium, nitrogen, oxygen, neon and argon for the 5 - 50 keV energy range. All graphs follow the same general trend and the only irregular feature is the indication of inflexions in the curve, for emission from graphite under carbon ion bombardment.

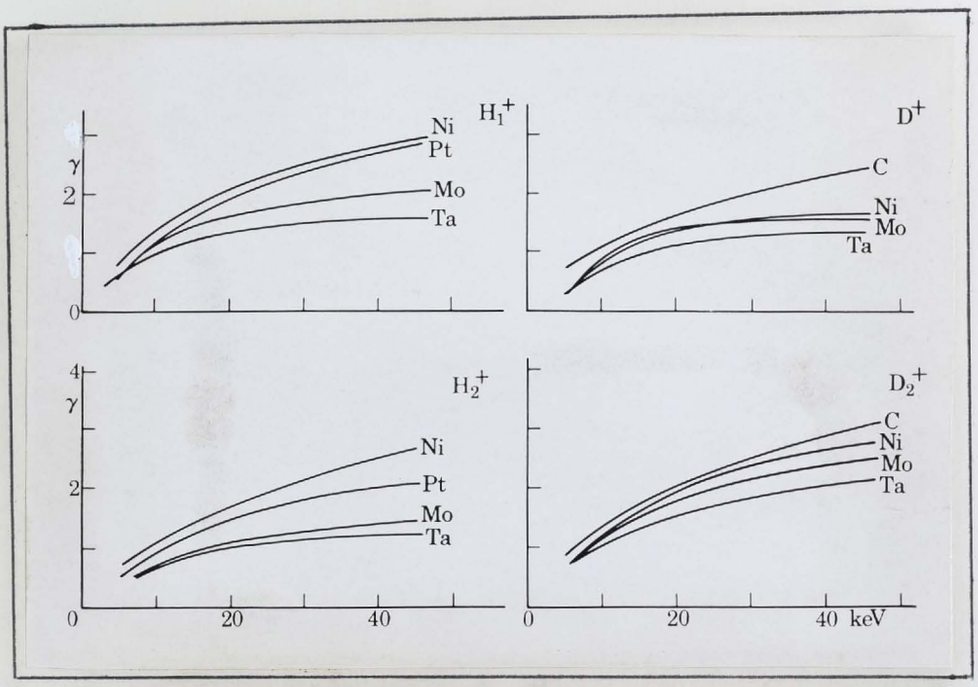

Figure 2.25 A

Secondary electron emission produced by hydrogen and deuterium ions from various target materials.

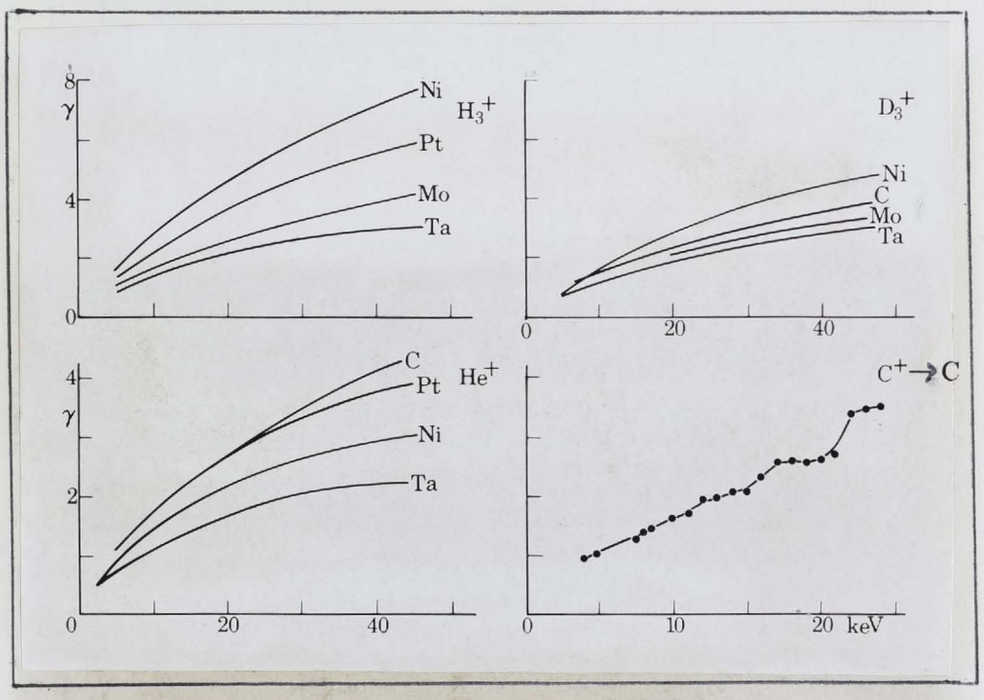

Figure 2.25 B

Secondary electron emission by hydrogen, helium, deuterium and carbon ions.

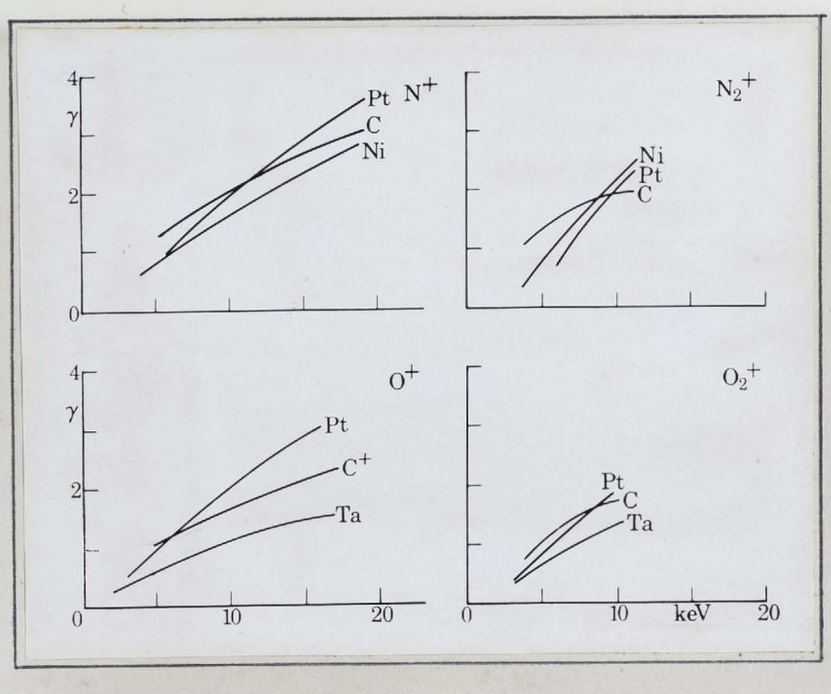

Figure 2.25 C

Secondary electron emission produced by nitrogen and oxygen ions.

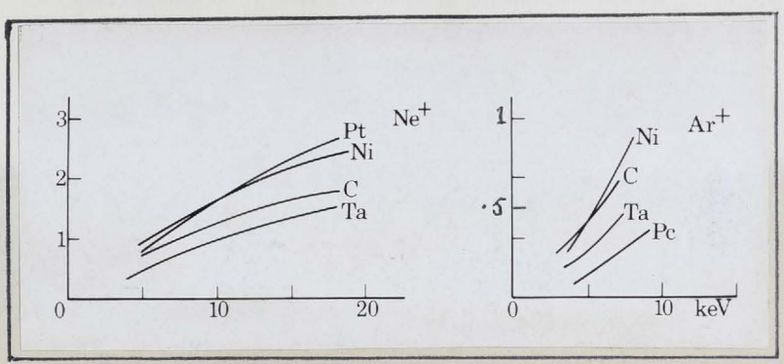

Figure 2.25 D

Secondary electron emission produced by ions of neon and argon.

The latter irregularity is probably due to experimental difficulties in maintaining a thoroughly clean carbon surface, rather than to any intrinsic physical effect.

(i) Dependence of γ on the energy and velocity of the incident ion

It is instructive to plot the experimental data in Figure 2.25 as emission against velocity of the incident ion (Figure 2.26). Our discussion in Chapter I indicated that velocity is a fundamental variable in determining the emission for low and medium energy ions, irrespective of ion mass.

The variation of the emission with velocity in Figure 2.26 is seen to be

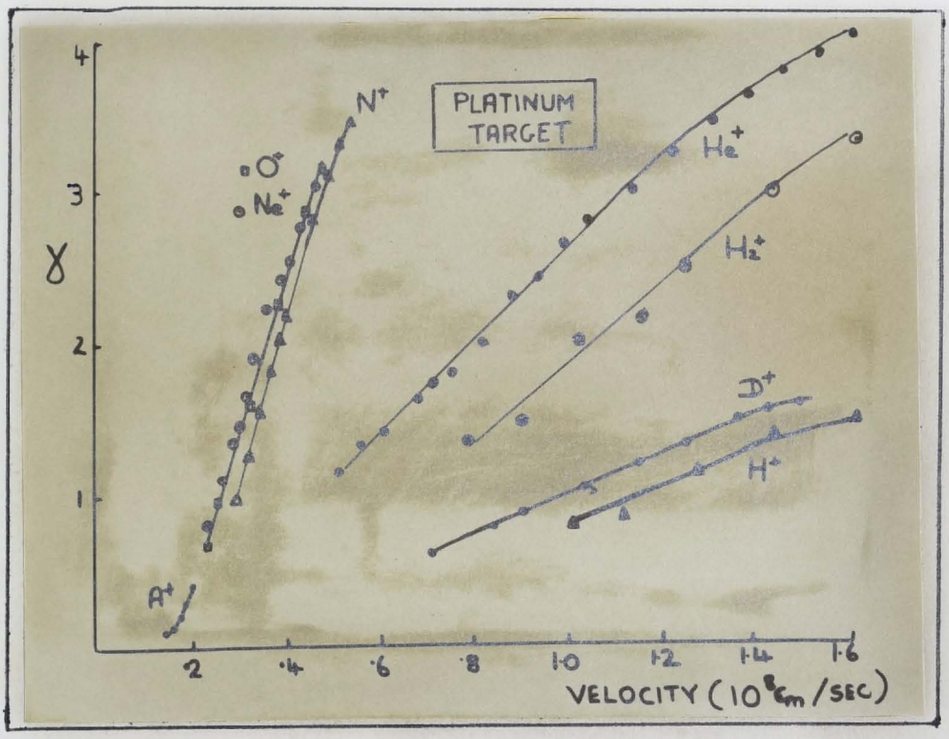

Figure 2.26 A

Variation of γ with velocity of incident ion for platinum target

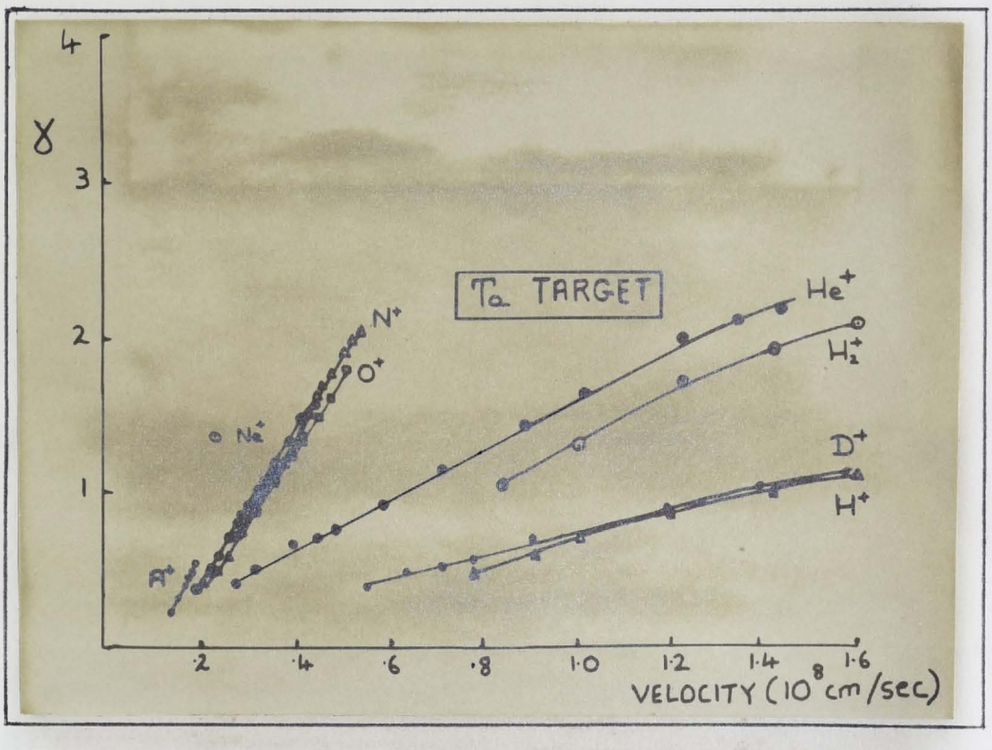

Figure 2.26 B

Variation of γ with velocity of incident ion for tantalum target.

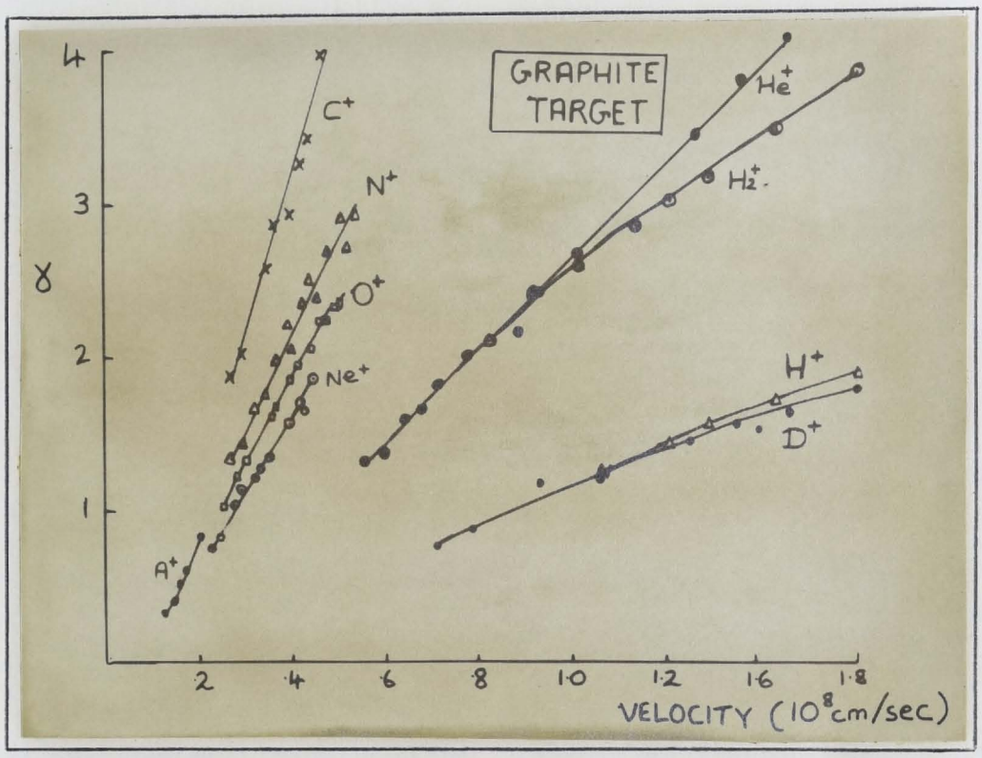

Figure 2.26 C

Variation of γ with velocity of incident ion for graphite target.

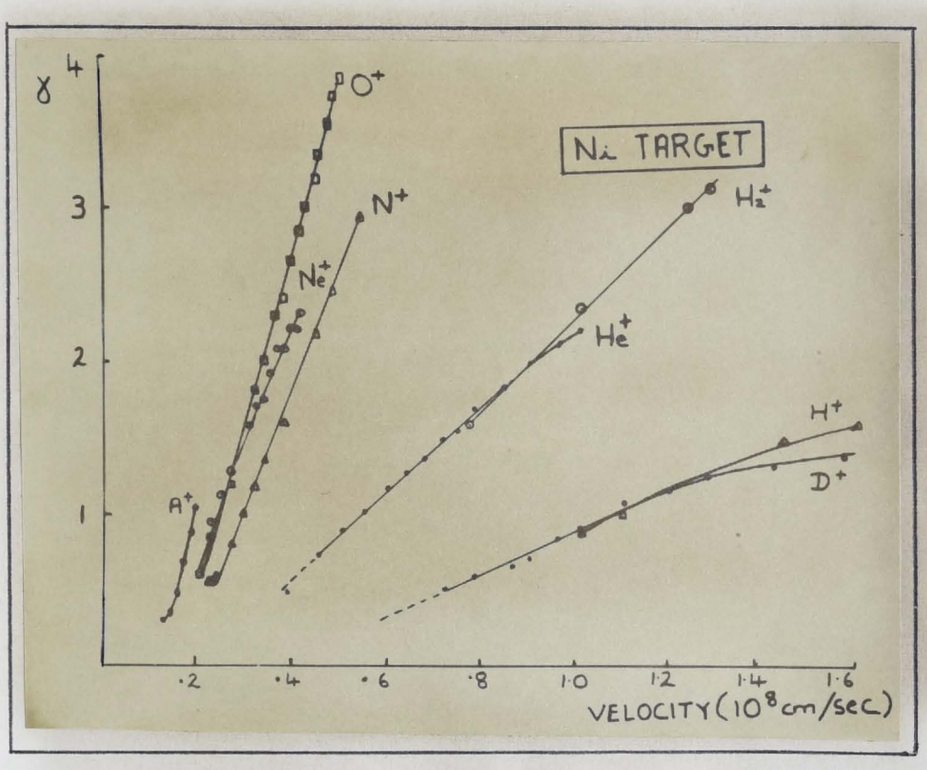

Figure 2.26 D

Variation of γ with velocity of incident ion for nickel target.

linear from ion velocities very near threshhold to velocities of an order of magnitude higher. Departure from linearity occurs at both the lowest velocities (about 10^7 cm/sec for argon) and the highest velocities (about 1.2×10^8 cm/sec, or higher for protons) investigated. This is in agreement with the predictions of the Parilis-Kishinevski theory discussed in Chapter I. At velocities very near threshhold the dependence becomes of the form v^2, while at sufficiently high velocities the emission begins to saturate.

The threshhold for kinetic emission may be estimated approximately by extrapolating the linear portions of the emission with velocity variations back to the velocity axis. The extrapolated threshholds are plotted in Figure 2.27 for various targets, as a function of Z_1 and are seen to decrease with increasing atomic number of the incident ion. Whereas the threshhold predicted by the Parilis-Kishinevski theory is the same for all target-ion combinations, and equal to 1.05×10^7 cm/sec, the observed threshholds for light ions are well above this. For heavier ions, however, the observed values do become nearly independent of Z_1 and close to the value predicted by the theory. The discrepancy for light ions is not surprising as the Parilis-Kishinevski theory is only valid,

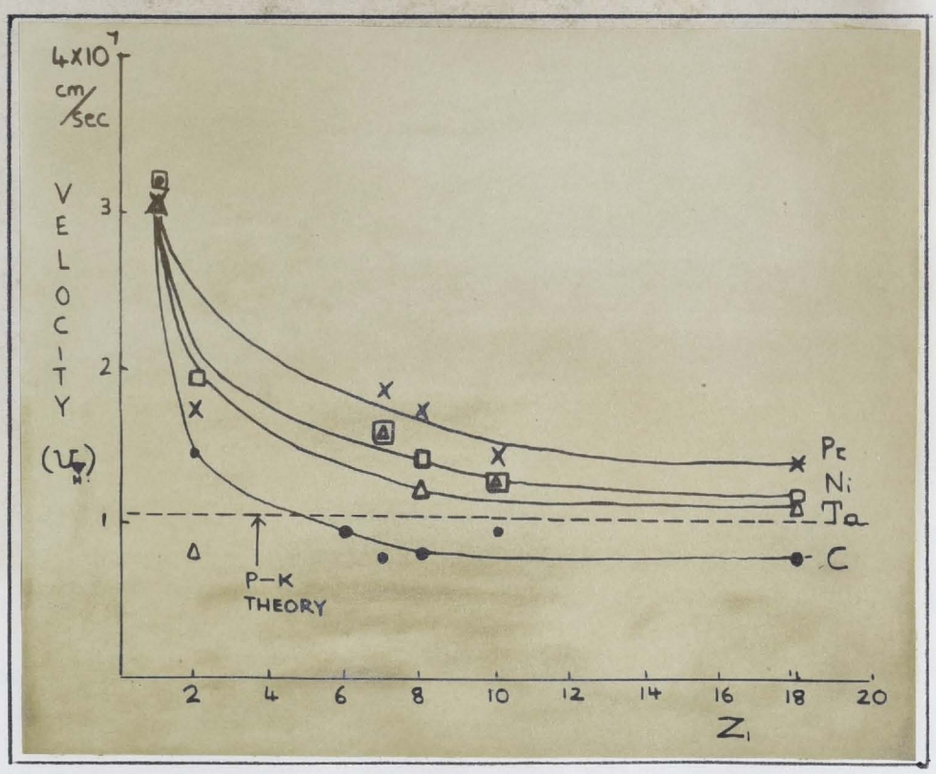

Figure 2.27

Variation of extrapolated threshholds for kinetic emission with atomic number of incident ion.

quantitatively, for ion-target combinations with

$$\frac{1}{4} < \frac{Z_1}{Z_2} < 4 .$$

The extrapolated threshholds plotted in Figure 2.27 are approximate, not only because of the departure from linearity of the emission at velocities close to the true threshhold, but also because of the presence of potential emission. Equation (2.16) becomes, in the present experiment:

$$\gamma = \gamma_{kin} + \gamma_{pot} , \qquad (2.17)$$

so that some potential emission may occur at velocities below the threshhold for kinetic emission. In Figure 2.27 the extrapolated threshholds for helium ions on Ta and Pt targets are lower than might be expected from the values for the other ions, possibly due to a higher potential emission contribution[29].

(ii) Dependence of γ on the masses of the incident and target particles

At a given velocity above threshhold, the atomic numbers of the colliding particles and not the mass numbers, are the important parameters in determining the emission. The present results indicate that the emission is roughly proportional to Z_1 for the lighter ions and, indeed, we can formulate the empirical relation:

$$\gamma = \frac{v - v_{TH}}{X} Z_1 , \qquad (2.18)$$

where X is approximately 2 for Pt and C, approximately 4 for Ta and approximately 2.5 for Ni. v_{TH} (or v_{min}) is the extrapolated threshhold and v is the incident ion velocity. The writer has been unable to relate this 'X factor' to any specific physical property of the target. While Ta clearly gives a lower emission at a given velocity above threshhold than the other targets, there is no directly apparent relationship between γ and the atomic number of the target atom, Z_2.

The theory of Parilis and Kishinevski[22, 23] predicts a mass dependence of the form

$$\frac{Z_1 + Z_2}{Z_1^{\frac{1}{2}} + Z_2^{\frac{1}{2}}}^2$$

for heavy ions and

$$(Z_1^{\frac{1}{2}} + Z_2^{\frac{1}{2}})(Z_1^{1/6} + Z_2^{1/6})^3$$

for light ions. Figure 2.28 plots the variation in emission for an incident ion species Y, normalized to the emission for N^+ ions, as predicted by both the relations proposed by Parilis and Kishinevski, and by the empirical relation (2.18) above. One sees that the empirical relation (2.18) is in reasonably good agreement with experiment for the lighter ions, whereas neither of the Parilis-Kishinevski expressions is at all accurate for these ions.

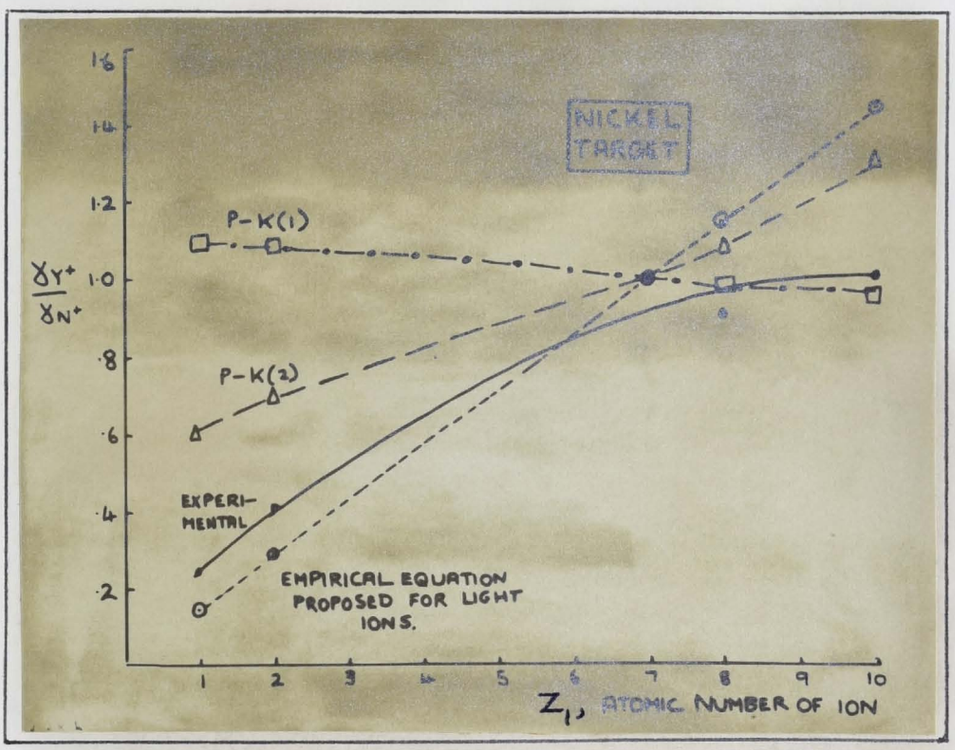

Figure 2.28 A

Variation of electron emission (normalized to emission for N^+) with Z_1 for nickel target.

For heavier ions the first Parilis-Kishinevski expression is the most accurate and the normalized emission is close to unity. The empirical relation (2.18) predicts that the emission would continue to increase linearly with Z_1.

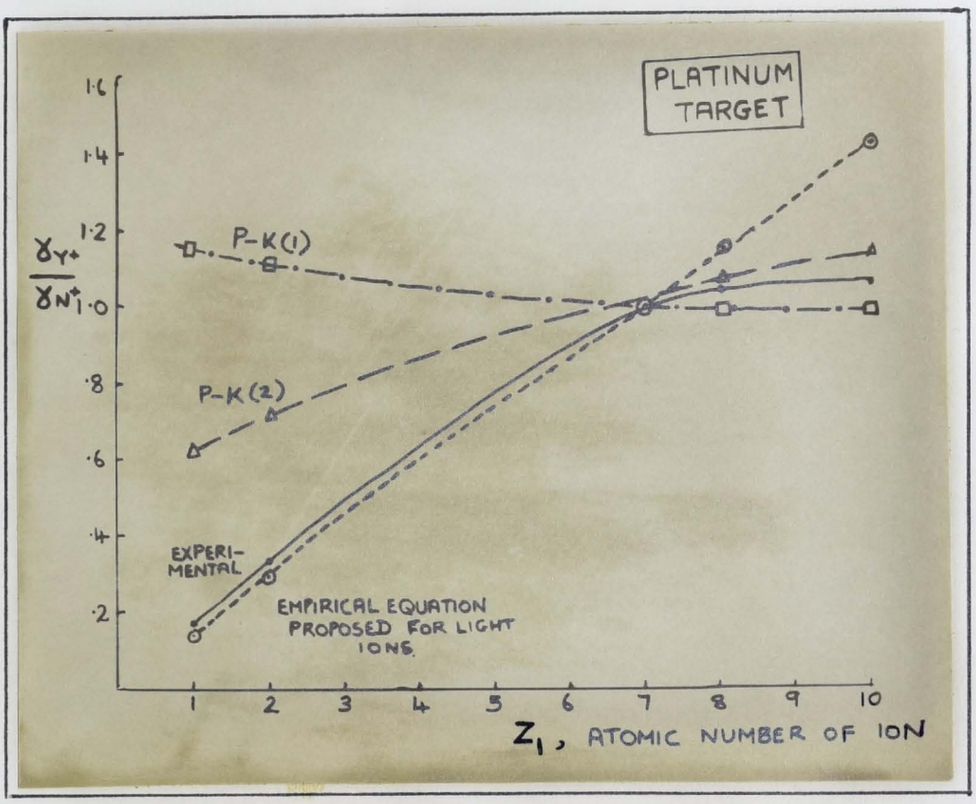

Figure 2.28 B

Variation of electron emission (normalized to emission for N^+) with Z_1 for platinum target.

We would not expect the Parilis-Kishinevski theory to be accurate for the lighter ions as the condition

$$\frac{1}{4} < \frac{Z_1}{Z_2} < 4$$

is not satisfied. Their second expression, however, does predict the correct form of the variation - an increase of emission with Z_1 - for lighter ions.

Figure 2.28 is plotted for platinum and nickel targets at a velocity above threshhold of about 3.2×10^7 cm/sec, this value being chosen to obtain maximum data for the figure. In the previous section 2-2 B (i), we discussed the possible source of error in obtaining the threshhold by extrapolation of the linear portions of the emission-velocity variation: these errors are, however, by all indications, small compared to 3.2×10^7 cm/sec.

Figure 2.29, for a graphite target, is interesting. None of the proposed equations is satisfactory for the heavier bombarding ions and the experimental

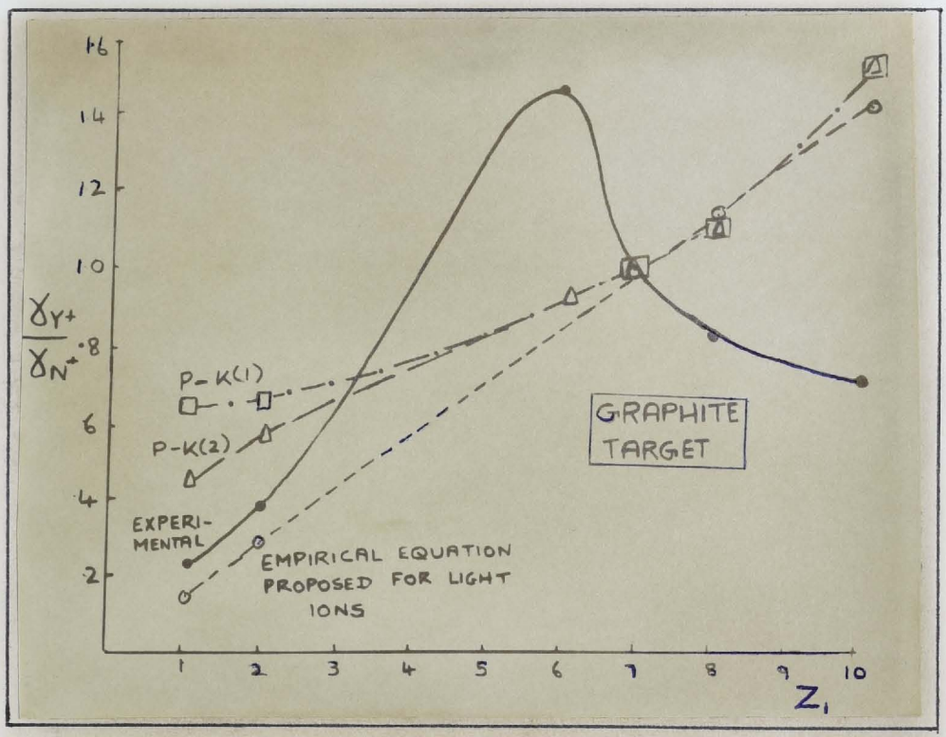

Figure 2.29

Variation of electron emission (normalized to emission for N^+) with Z_1 for a graphite target.

data indicate a peak in the emission for C^+ ions on graphite, with a pronounced decrease in emission for heavier ions. The Parilis-Kishinevski theory predicts an increase in emission with Z_1. Clearly, therefore, the Parilis-Kishinevski theory falls down for the case of a low atomic number target, even when the condition

$$\frac{1}{4} < \frac{Z_1}{Z_2} < 4$$

is satisfied. To the writer's knowledge no present theory explains the results for a graphite target, particularly the peak in the emission which occurs at $Z_1 = Z_2 = 6$. The presence of some surface effect, leading to an enhanced apparent emission for C^+ ions on graphite, cannot be ruled out.

The emission at 8 keV is plotted in Figure 2.30, against the incident ion mass, for graphite and tantalum targets. Omitting the results for protons, one sees that the emission increases with Z_1 initially, peaking at several a.m.u. The emission then drops until, for incident A ions, it has fallen to the value for

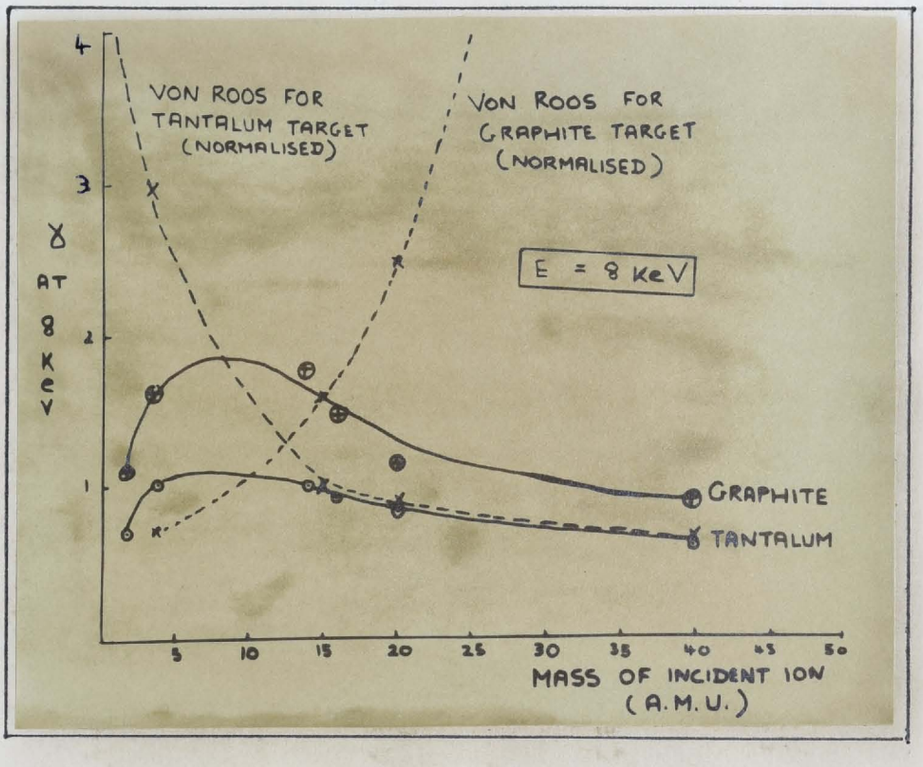

Figure 2.30

Variation of electron emission with the mass of incident ion at 8 keV ion energy, for graphite and tantalum targets.

deuteron ions again. The data is presented in this form, as it enables us to check the prediction of the Von Roos[25] theory (section 1-4) that

$$\gamma \propto \frac{(1+\mu')^4}{\mu'},$$

where

$$\mu' = \frac{M_1}{M_2}, \text{ at constant incident ion energy.}$$

The velocity ranges attainable for the various ions do not overlap sufficiently, at any single velocity, for his prediction at constant incident-ion velocity to be tested over a broad incident mass range. The predictions of the Von Roos theory are drawn to be coincident with the experimentally observed plots at 15 a.m.u. incident ion mass. Experimental data for platinum and nickel targets are not included, as they follow the same pattern as for tantalum.

The Von Roos theory, like the Parilis-Kishinevski theory, gives very close to the correct dependence of emission on the particle masses, for heavy ions incident on high Z_2 targets. Like the Parilis-Kishinevski theory, however,

it becomes inaccurate for light ions on high Z_2 targets and also does not predict the observed trends for a graphite target, over any part of the mass range. This is clearly indicated in the figure.

One would not expect the Von Roos theory to be accurate for light ions, as it assumes that the elastic collision cross section is much more than the ionization cross section. Our discussion in the first chapter showed that this assumption is only valid at low ion velocities, i.e., for heavier ions at medium energies. However, Von Roos' other basic assumptions, especially his assumption of the target as a "gas" of "free" lattice atoms, would seem to render the physical basis of his theory rather suspect. Thus the agreement between his theory and experiment for the dependence of emission on particle masses, for heavier incident ions on high Z_2 targets, may be fortuitous. The Parilis-Kishinevski theory probably corresponds best to the physical reality of the emission process and further refinement of it - as attempted by the authors themselves[23] - will undoubtedly lead to a more detailed understanding of kinetic emission.

We saw in Chapter I that the theory of Izmailov[24] predicts $\gamma \propto E_0/M_1$ at low energies, i.e., $\gamma \propto v^2$. This agrees with the v^2 dependence predicted by the Parilis-Kishinevski theory for velocities very close to threshhold (equation (1.57)): however, its predictions are invalid for all higher velocities and the theory, which considers only the ejection of free electrons, is clearly inadequate to explain the observed data.

(iii) Dependence of γ on the charge of the incident ion

This can be ascertained from Figure 2.31 which supplements Figure 2.25 and indicates the emission per particle as a function of energy per particle for various molecular ions. The near coincidence of the emission functions for each molecular ion target combination indicates that:

1. The molecular ion dissociates into its atomic components upon striking the surface.

2. Each atomic component makes nearly the same contribution to the total electron emission.

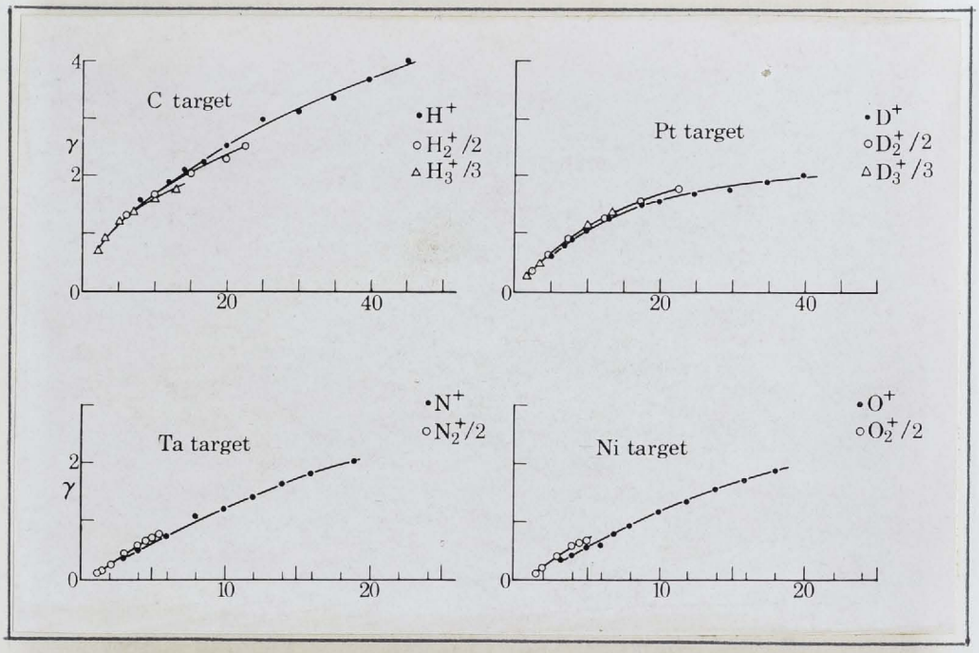

Figure 2.31

Comparison of secondary electron emissions per particle produced by atomic and molecular ions. Energy in keV per particle.

Thus, for example, there occurs at the surface:

$$H_3^+ \rightarrow H^+ + H^o + H^o$$

$$O_2^+ \rightarrow O^+ + O^o$$

and the singly charged and neutral dissociation products release the same, or nearly the same, number of secondary electrons from the target.

At low incident ion energies, there is some indication that, in general, the neutral component of the molecule produces slightly greater emission than the atomic ions, but at higher energies there is no consistent pattern and the differences are seldom large. Table 2.2 summarizes the results, where a plus sign indicates that neutral emission is greater than atomic ion emission and a negative sign indicates that it is less. Zero denotes that the emissions are the same to within the experimental error. The latter is about 5% for these experiments.

TABLE 2.2

TARGET	BOMBARDING SPECIES			
	H	D	N	O
Ta	-	0	+	0
Mo	-	-	.	.
Ni	+	+	+	+
Pt	+	0	+	+
C	-	-	-	-

(iv) The effect of the presence of potential emission on the electron emission experiments

For ion target systems, where the ionization energy exceeds twice the work function, emission can also occur by the potential emission process (Auger neutralization). Indeed, the probability of potential emission increases as this difference increases. For hydrogen, deuterium, nitrogen and oxygen ions on our targets, the difference is small, but for helium, neon and argon ions, particularly the former two, the difference is quite large and potential emission cannot be ignored in our results. We noted previously that potential emission could account for the threshholds for helium ions on platinum and tantalum targets being lower than expected (Figure 2.27). From Figure (2.26) it is also to be noted that the emission for helium ions, at all velocities covered, exceeds that of H_2^+ ions, although upon the basis of kinetic emission alone, one would expect the emissions to be identical (same Z_1 value). The higher emission for helium ions which is about 0.5 units higher for platinum, and 0.1 units higher for tantalum, is probably due to the potential contribution.

By the same token, one concludes from the near coincidence of the emission per particle versus energy per particle (or velocity) data presented above for the molecular ions and atomic ions of hydrogen, deuterium, nitrogen and oxygen, that the contribution due to potential emission must be small in these cases.

More aspects of electron emission in the light of energy distribution measurements on the emitted electrons will be given in the next chapter, together with more about the theory.

C. Results for systematic measurements on the apparent ion scattering coefficient, R

Figure 2.32 plots the experimental data for R as a function of ion beam energy for various ion target combinations. All follow the same trends except for the results for the heavy ions A^+ and CO_2^+ on graphite, which are anomalous. This anomalous behaviour may be associated with the fact that $M_1 > M_2$,

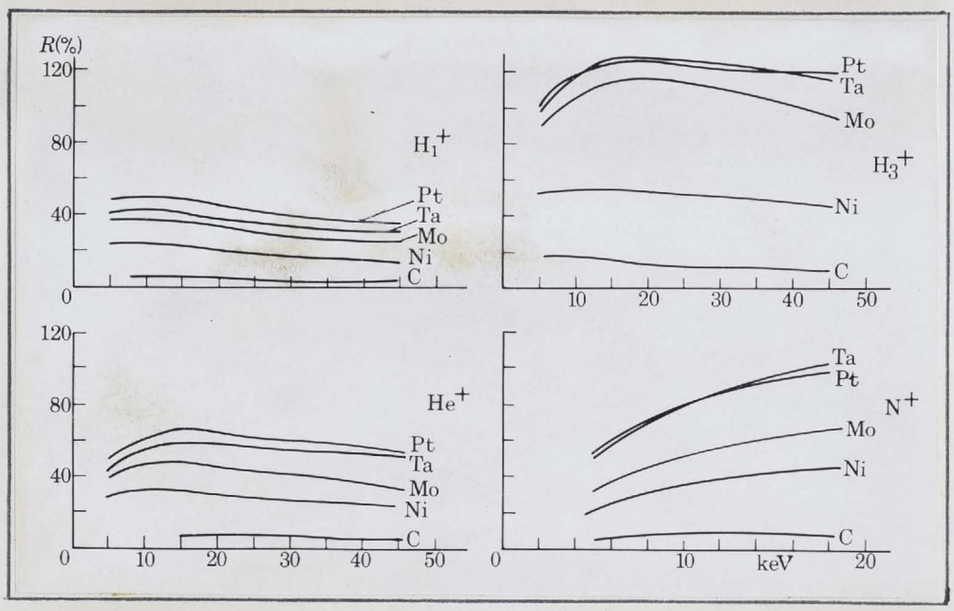

Figure 2.32 A

Variation with bombarding energy of apparent total scattering of hydrogen, helium and nitrogen ions from various targets.

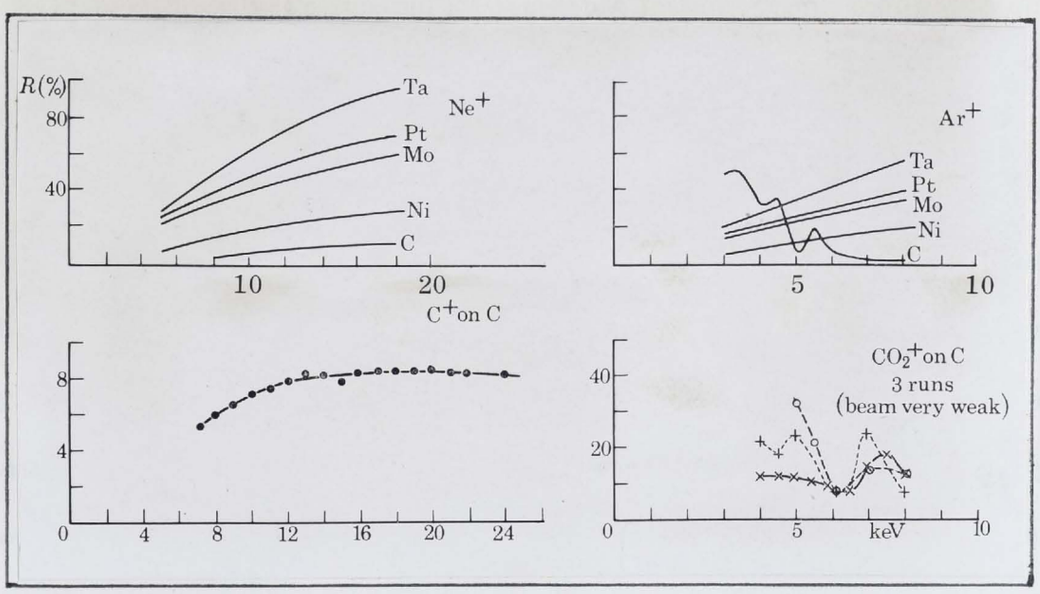

Figure 2.32 B

Variation with bombarding energy of apparent total scattering of neon, argon, carbon and CO_2^+ ions from various targets.

although one would expect the CO_2^+ molecular ion to dissociate into its components upon striking the target surface. (The CO_2^+ ion beam was quite weak - about 5×10^{-10} amps - and so it was not possible to obtain good reproducible results with it. However, its behaviour was clearly anomalous and also the results for A^+ ions did not conform to the trends observed for the lighter ions).

From equations (2.9) and (2.12), we can write:

$$R = \underset{(1)}{(\rho_+ - \rho_-)} + \underset{(2)}{s_+} + \underset{(3)}{\gamma'_c(\rho_+ + \rho_- + \rho_m)} + \underset{(4)}{\gamma_s(s_+ + s_-)} \; . \qquad (2.19)$$

The question now arises of the relative importance of the contributions arising from the sputtering of target ions (terms (2) and (4)) and from scattering of incident particles (terms (1) and (3)). While some researchers have attributed the positive emission 'R' to sputtered target ions[30] this assumption is not supported by the present work. Several considerations to be discussed both below and in Chapter IV, indicate that it is not tenable to assume a sputtering coefficient for IONS of the order of 40 - 50% (for the heavier targets) at several keV energies. If, therefore, we assume that the sputtering terms in equation (2.19) are very small compared to the ion scattering terms, we have:

$$R = (\rho_+ - \rho_-) + \gamma'_c(\rho_+ + \rho_- + \rho_m) \; . \qquad (2.20)$$

The above assumption is certainly permissible for light ions. For heavier ions, the sputtering yield increases at a given incident ion energy, but one still would not expect the proportion of sputtered ions to make an appreciable contribution to the positive current, comprising R. There is no obvious relation between R and the number of electrons in the "d" shell, whereas the sputtering yield has a strong dependence upon the latter[21]. Also, the R(E) curves for A^+ on various metals (Figure 2.32) are quite different from the sputtering yield curves found by several authors (Figure 1.6). The cases where significant numbers of sputtered target ions may be present are for the heavy ions, CO_2^+

and A^+ on graphite and, as noted above, these are the very cases which do not follow the trends observed for the scattering of other ions.

(i) Dependence of R on the velocity of the incident ion

In Figure 2.33 are plotted the variation of R with incident ion velocity for various ion target combinations.

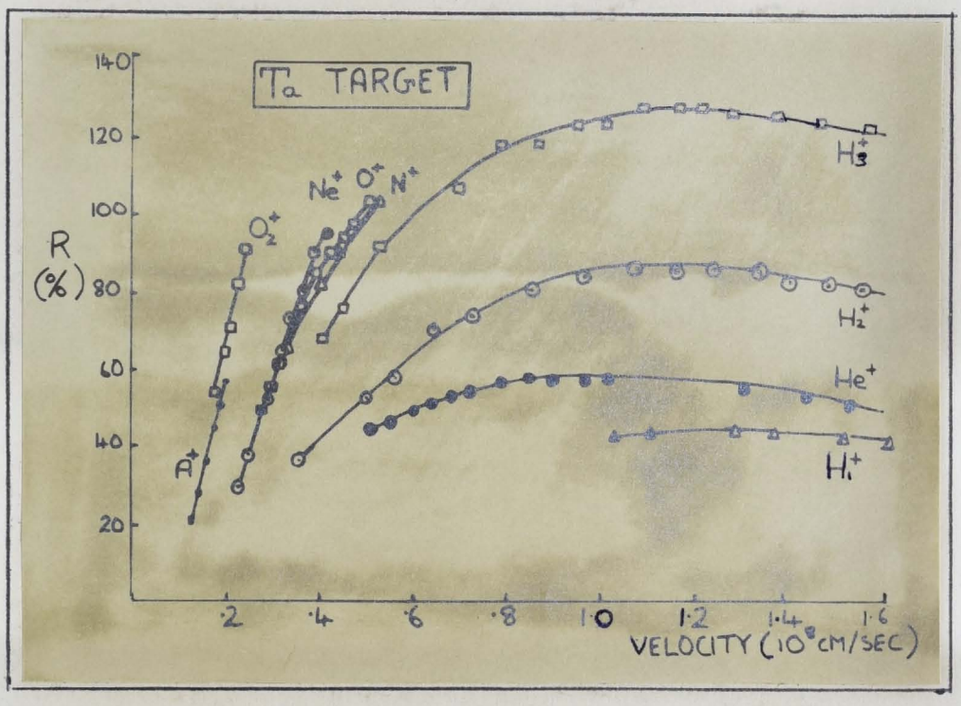

Figure 2.33 A

Variation of R with velocity of incident ion for tantalum target.

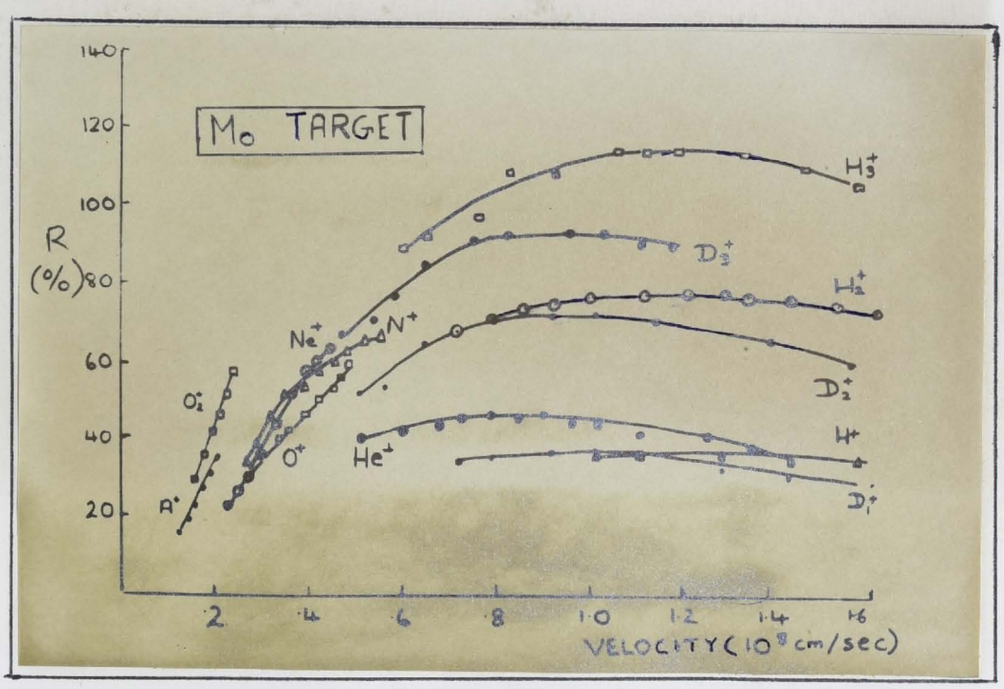

Figure 2.33 B

Variation of R with velocity of incident ion for molybdenum target.

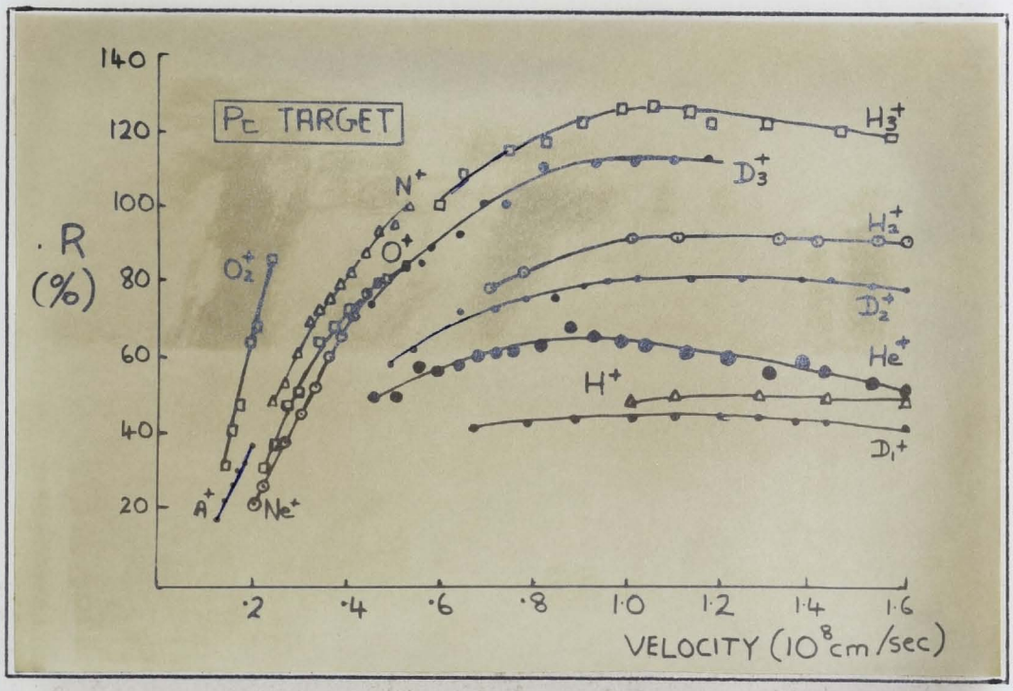

Figure 2.33 C

Variation of R with velocity of incident ion for platinum target.

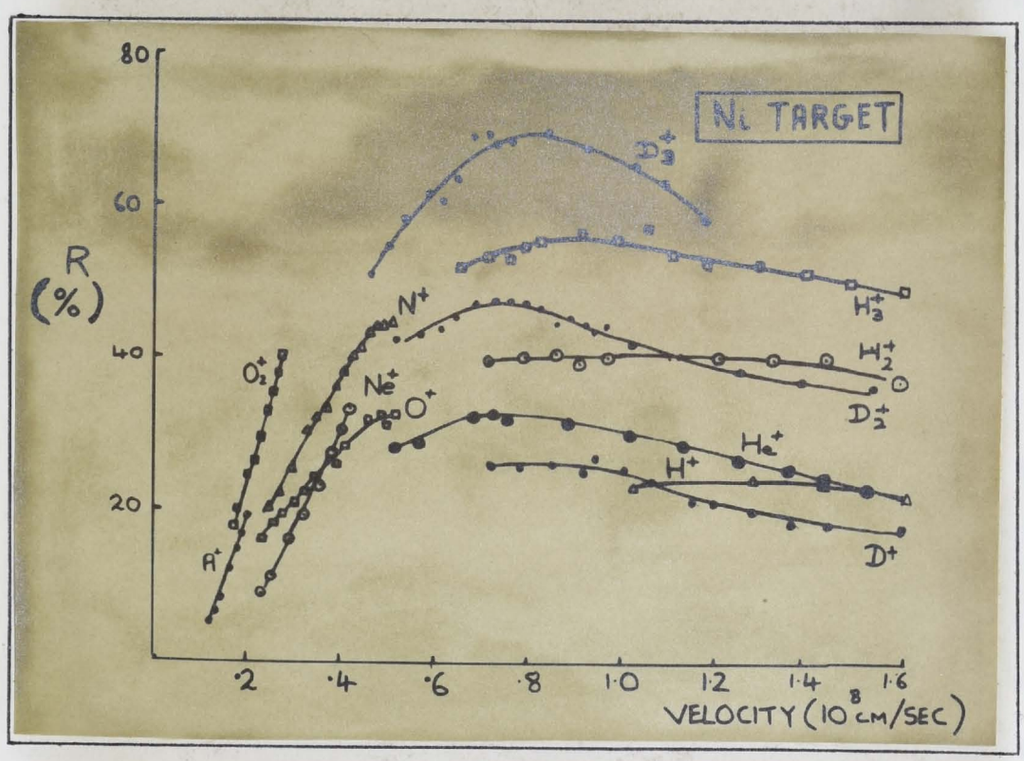

Figure 2.33 D

Variation of R with velocity of incident ion for nickel target.

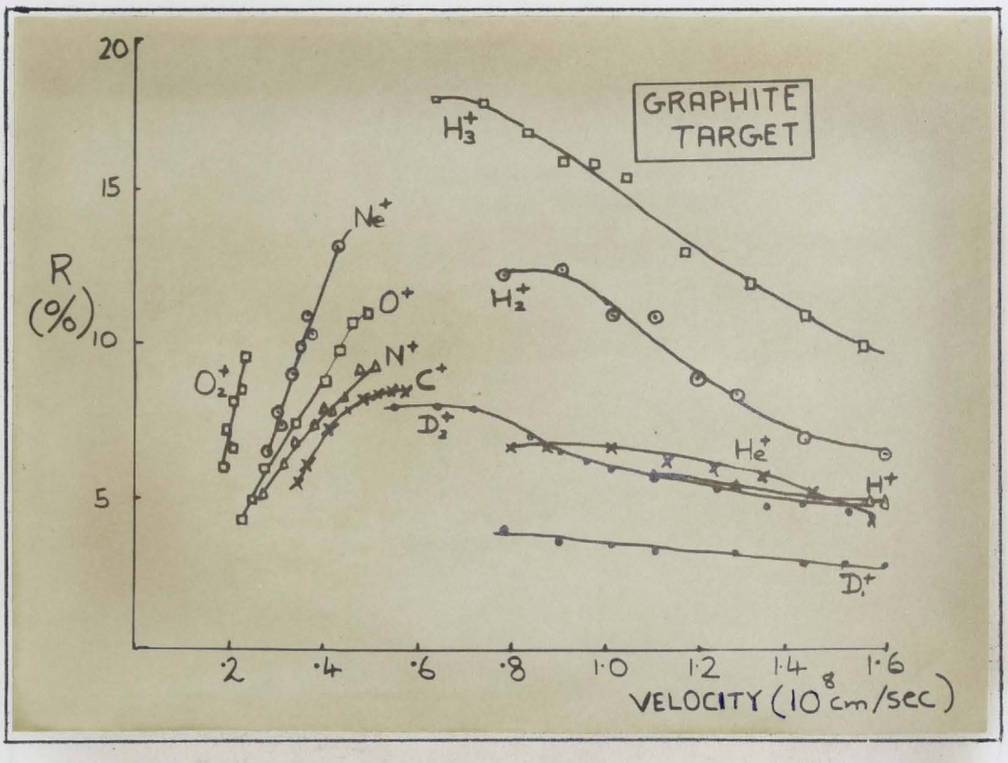

Figure 2.33 E

Variation of R with velocity of incident ion for graphite target.

In equation (2.20) the reflection coefficients ρ_+, ρ_- and ρ_m do not have the same dependence upon the incident ion velocity and in Chapter IV we shall see that ρ_+, $\rho_- \ll \rho_m$, for velocities below about 10^8 cm/sec. Thus for low velocities, we can reduce equation (2.20) to the form:

$$R \simeq \gamma'_c \rho_m . \qquad (2.21)$$

At velocities close to zero, ρ_m probably drops sharply to zero, but over the range from these very low values up to about 3×10^7 cm/sec, there are indications that it remains approximately constant. From Figure 2.33 we see that R increases linearly with velocity up to about 4×10^7 cm/sec, where it begins to turn over. Now in the previous section, we saw that the secondary electron coefficient γ increases linearly with velocity up to velocities well above this, and so it is reasonable to assign the linear increase in R to the γ'_c factor in equation (2.20). Thus the reflection coefficient ρ_m must remain approximately constant for velocities up to about $\sim 4 \times 10^7$ cm/sec, as stated above. The corresponding energy is about 1 keV for protons and 30 keV for A ions.

TABLE 2.3

ION	TARGET				
	C	Ni	Mo	Ta	Pt
H_1^+	-	0.80	1.2	1.30	1.30
H_2^+	0.70	-	1.1	1.1	1.1
H_3^+	0.65	0.90	1.1	1.15	1.05
D^+	-	0.80	1.05	-	1.10
D_2^+	0.60	0.75	0.90	-	1.10
D_3^+	-	0.80	0.90	-	1.00
He^+	0.80	0.75	0.90	0.90	0.95
average	0.69	0.80	1.02	1.09	1.07

Table 2.3 lists the positions of the maxima in units of 10^7 cm/sec, to the nearest 0.01×10^7 cm/sec.

Figure 2.34 plots the average position of the maxima for the various targets. One sees that the average position of the maxima moves towards higher velocities as Z_2 increases, the shift being quite significant for lower values of the latter. For Rutherford type back-scattering one would expect the number of back-scattered particles at low velocities (which are mainly in the neutral charge state) to fall off more rapidly with velocity for the lower Z_2 targets (equation (1.43)). This would shift the peaks in the apparent scattering curves towards lower velocities, as observed.

(ii) Dependence of R on the atomic numbers of the incident ion and target

Figure 2.35 shows the apparent scattering of H_1^+, H_2^+, H_3^+, D_1^+, D_2^+ and D_3^+ at an energy per particle of 15 keV (or velocity of 1.75×10^8 cm/sec), plotted against Z_2. Figure 2.36 shows similar results for some heavier ions,

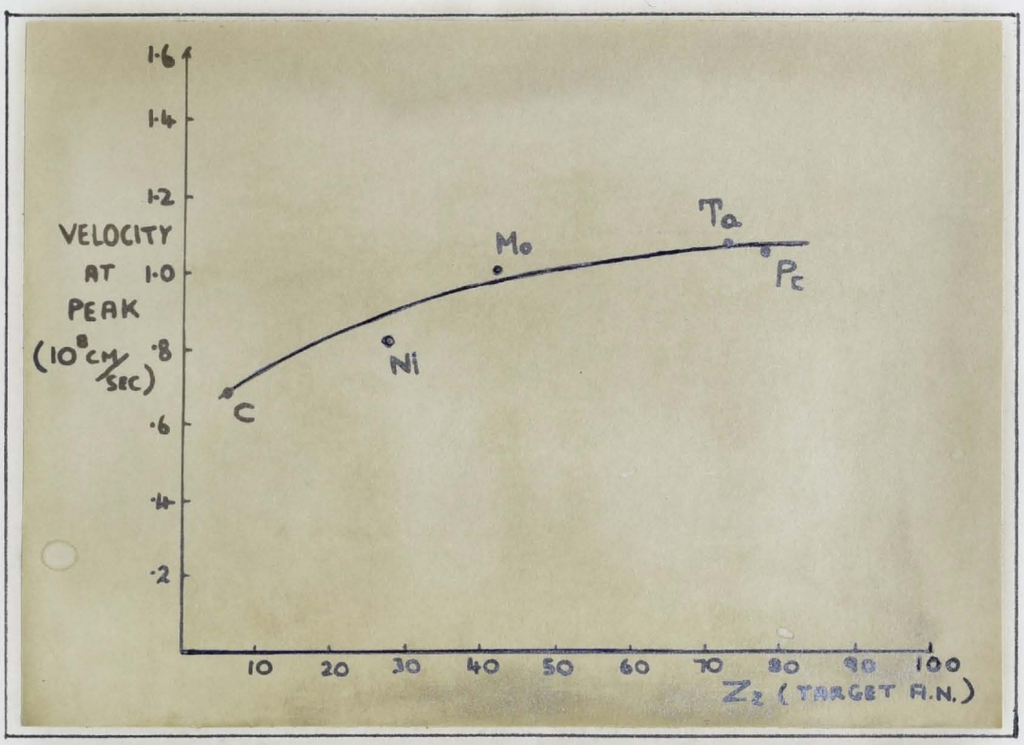

Figure 2.34

Average value of velocity at peak of R versus velocity curves plotted against the atomic number of the target.

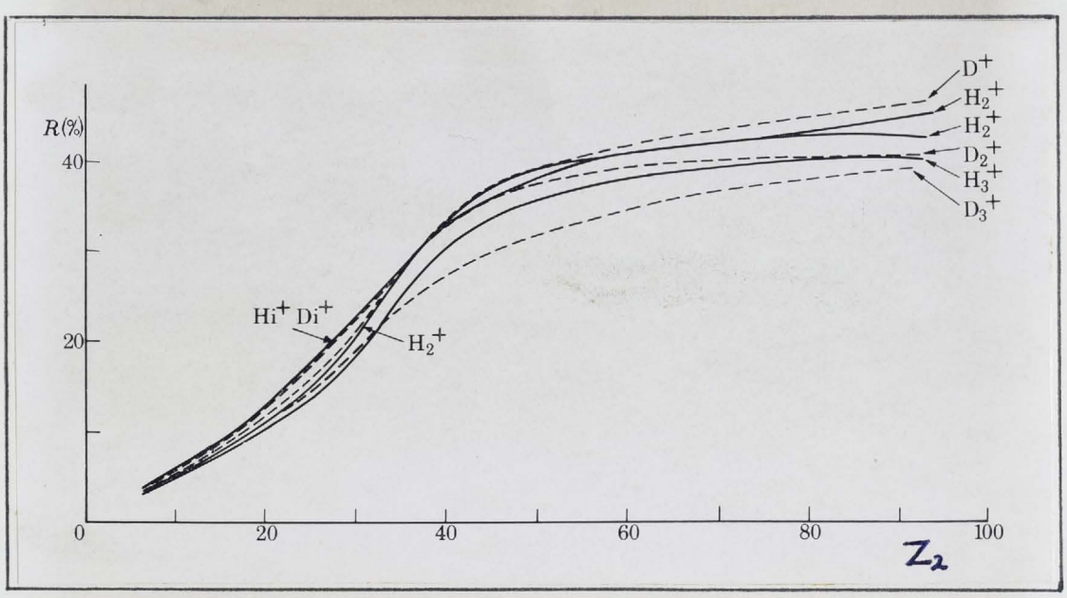

Figure 2.35

Variation with atomic number of total apparent scattering of hydrogen and deuterium particles with initial energy of 15 keV per particle.

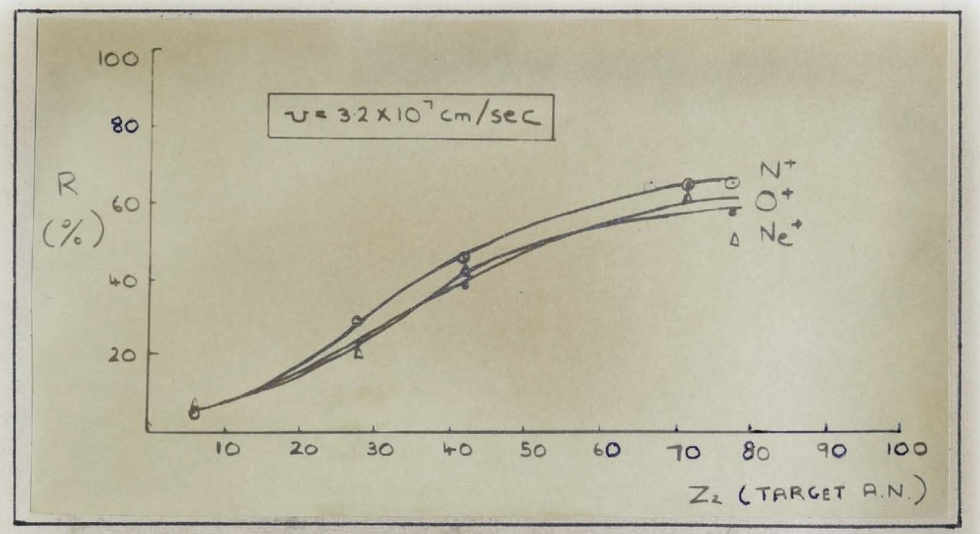

Figure 2.36

R for N^+, O^+, Ne^+ ions at a velocity of 3.2×10^7 cm/sec plotted against Z_2.

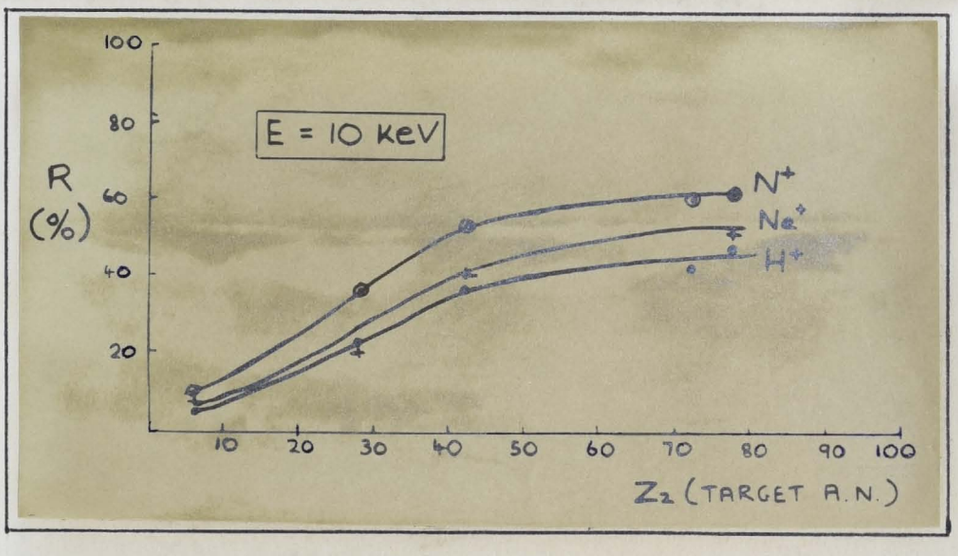

Figure 2.37

R for various ions at 10 keV incident energy, plotted against Z_2.

N^+, O^+ and Ne^+ at a somewhat lower velocity (3.2×10^7 cm/sec), while Figure 2.37 plots R against Z_2 for various ions at an incident ion energy of 10 keV. In all cases R increases roughly as Z_2^2 for low Z_2 values, but levels off to a nearly constant value for Z_2 values exceeding about 50. On the other hand, Figure 2.38 plots the variation of R with Z_1 for various targets, at a velocity of 4.8×10^7 cm/sec, while Figure 2.39 plots the variation of R with Z_1 for various targets, at an incident beam energy of 10 keV.

Summarizing these results, one sees that the apparent scattering

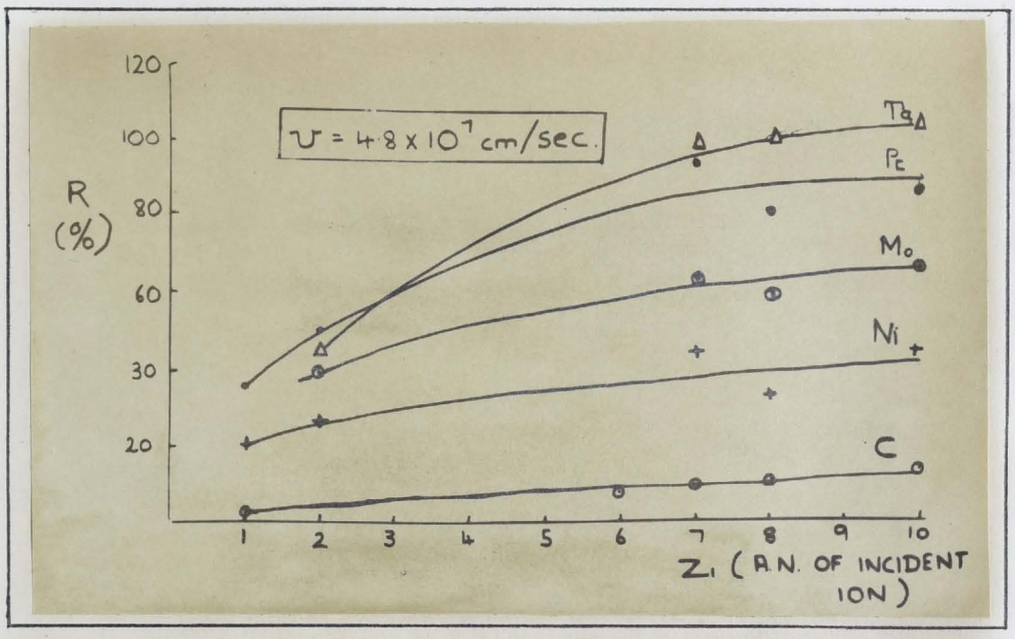

Figure 2.38

Variation of R with atomic number of incident ion, for constant incident ion velocity.

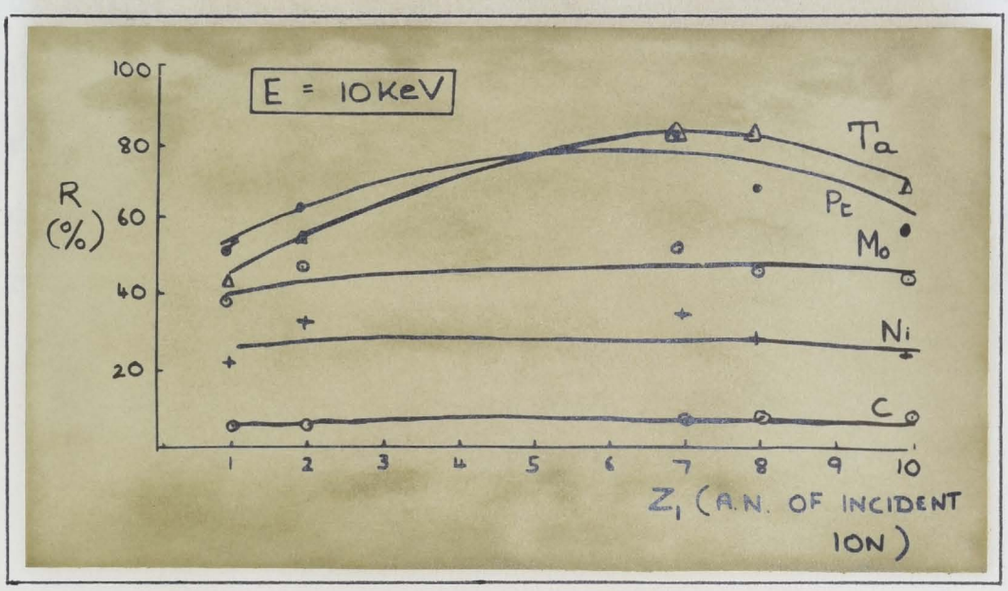

Figure 2.39

Variation of R with atomic number of incident ion, for constant incident ion energy.

coefficient R has a dependence upon both Z_1 and Z_2. With either one of these kept constant, R generally increases with the other. However, the dependence upon Z_2 is much more pronounced than upon Z_1, at a given incident ion energy. These observations are important in view of equation (2.20), from which we see that any dependence of the reflection coefficients ρ_+, ρ_- and ρ_m upon the atomic numbers, Z_1 and Z_2, will be mirrored by the same dependence of R upon these quantities. At a given incident ion energy or velocity, the factor

γ_c' is, of course, a constant. From equation (1.43), one would expect, for Rutherford type back-scattering, R to be nearly independent of Z_1 for $Z_1 \ll Z_2$ and to increase with Z_2. The turnovers in Figure 2.39, for higher Z_2 targets, are probably due to the increased role of screening in scattering from these targets. It is of interest to note that in Figure 2.39, R varies very little for Z_1, even for the cases where $Z_1 > Z_2$ (N^+, O^+, Ne^+ on a graphite target).

(iii) Dependence of R on the charge of the incident ion

The near coincidence of the various curves in Figure 2.35 shows that the initial charge state of a bombarding particle does not greatly influence the total scattering. R for D^+ on Pt is about 15% greater than one third of the R value for D_3^+, while R for H^+ on Pt is about 10% greater than one third of the R value for H_3^+ at 15 keV per particle incident energy. On the other hand, R for O_2^+ and N_2^+ is slightly more than twice the values for O^+ and N^+, respectively, at the same velocity. Thus, as for the case of electron emission, it is difficult to make any definite generalizations. However, to a first approximation, R is clearly independent of the ionic charge.

CHAPTER III

ENERGY DISTRIBUTION MEASUREMENTS I: ANALYSING SYSTEM AND ENERGY SPECTRA FOR ELECTRONS

3-1 Energy Analysing System

A. Description

The work on energy distributions reported in this and the following chapter, was performed with the energy analysing system shown schematically in Figure 3.1. In the Appendix, some results will be briefly discussed for an energy analyser of quite different design, but suffice it to say here, that they confirm the general results reported.

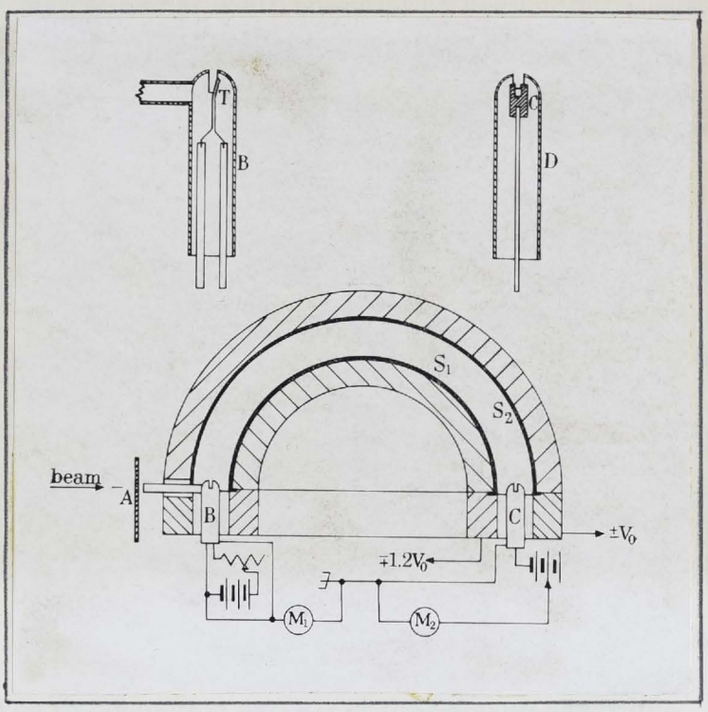

Figure 3.1

Diagram of apparatus used for analysis of the energies of secondary charged particles produced by positive ions bombarding a solid target.

The analyser shown in Figure 3.1 consisted of two hemispheres S_1 and S_2, to which voltages could be applied via insulated glass to metal seals from external supplies. The resulting electrostatic field, for the appropriate applied voltages, focussed secondary electrons from the target T, through a 180^{o} deflection, onto the collector C. The hemispheres were accurately

machined to radii of 5,398 and 4,445 cm and were faced with pure gold to minimize surface charge effects.

In order to obtain correct focussing, it was necessary to accurately align the analysing system so that all the secondary electrons from the target at right angles were collected at C, while no spurious signals were measured at the latter. With correct alignment the currents to the target and collector peaked simultaneously as the ion beam was swept across the target chamber aperture.

Both T and C were enclosed in platinum cylindrical boxes B and D respectively and the particles emitted from T followed paths with a mean radius of 4.921, the mean geometrical radius between the hemispheres. This mean path was maintained at earth potential by keeping the inner electrode at - 1.2, i.e., $\left(\frac{5.398}{4.445}\right)$ times that on the outer.

The incident ion beam was defined by a diaphragm A, about 1.5 mm diameter and passed through a length of straight tubing to ensure that it struck the target at the correct place - precisely under the slot in the target box, B.

The energy of the secondary electrons in eV was obtained by multiplying the potential difference between the electrodes, in volts, by a numerical factor obtained from the geometry of the analyser. The calculation performed in the Appendix shows that the factor is 2.56 in the present case.

The analyser was mounted in a "top-hat" shaped detection chamber, mounted on the detection section of the vacuum apparatus. The ion pumps of the latter reduced the residual pressure in the analysing space to less than 10^{-8} torr, but the beam itself raised the pressure in the space by a factor estimated to be of the order two. The pressure in the analysing space could not be measured directly, but was estimated from readings from a B-A ionization gauge located in the side arm.

The actual target consisted, as in the work reported in the previous chapter, of a strip of foil, 0.0025 - 0.050 mm thick and 5 mm wide. However, for these experiments, the foil was folded closely to minimize the magnetic

field arising from the heating current. The target was flashed to a white heat and then maintained at a temperature of about 1,000°C or more, prior to each experimental run. Upon cooling the target to room temperature, the secondary emission, monitored on a recorder, changed only slowly with time, indicating a slow build-up of contamination on the target surface. The target was usually kept at a red heat during the experiments and all results were reproducible to within a few per cent for an outgassed target.

The Vibron electrometer M_1 in Figure 3.1, measured the total beam current into the target chamber, plus the current due to secondary electrons or scattered ions which escape through the slot into the analysing space. The latter is estimated to be about 5% of the total secondary electron current, which is of the same order as the total beam current (Chapter II). In the results which follow, the quantity 'i_b' will denote the reading on M_1 and so our $\frac{i_c}{i_b}$ values will be slightly less than the actual collector current to beam current ratio. During these measurements, B was kept at target potential, so that no additional acceleration was imparted to the electrons. The second Vibron electrometer, M_2, measured the collector current to C. The latter could be suitably biassed relative to earth to prevent the escape of tertiary electrons from it (see below).

B. Testing of the Analyser

The analyser was tested by replacing the target with a hairpin of tungsten wire which was heated to incandescence to give thermionic emission. For a sufficient thermionic current, the potential drop across the filament was about 3V and so electrons emitted from the centre of the filament had a potential energy of about - 1.5 V relative to the positive end of the wire. The latter was now given a potential of - 3.2 V relative to the slot (i.e., relative to B), and so the total acceleration energy imparted to the electrons entering the analysing chamber from the centre point of the wire was (1.5 + 3.2) = 4.7 eV.

Curve a in Figure 3.2 shows that the collector current peaked at 5.07 eV and so electrons entering the analysing space clearly tended to originate from a

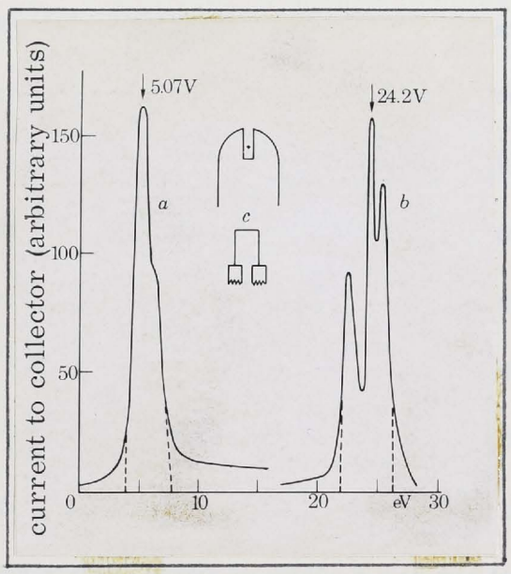

Figure 3.2

Test spectra of the energies of accelerated electrons

portion of the wire slightly off its centre. The asymmetry of curve a and its extrapolated base width of about 4 eV, could be explained by the scattering of electrons at the edges of the slit, combined with the effects of the voltage drop along the filament and of the magnetic field due to the heating current. In the ion beam experiments, however, the slot was kept at cathode potential and the magnetic field was negligible because of the folding of the target: also, of course, there was very little voltage drop across the heated target. Thus, the broadening of the energy spectra from these factors would be insignificant.

When curve a was taken, a bias potential of + 3V was applied to the collector C, to suppress tertiary electron emission from it. An investigation showed that this bias was responsible for the pronounced high energy tail in curve a, as the tail disappeared when the bias was removed. It appeared, therefore, that the platinum box D, surrounding C, did not supply sufficient shielding to prevent the small bias on C from perturbing the analysing field between S_1 and S_2 in the region of the slot in D. This resulted in some electrons being collected from parts of the analysing system, e.g., the slot in B, the analysing electrons S_1 and S_2, etc., other than the target. These electrons were released by radiation or, more likely, by secondary electrons and scattered

ions from the target.

In view of the above observation, it was decided to measure the energy spectra with zero bias on the collector. This introduced an error arising from current loss due to electron reflection from the collector: however, this could not have exceeded about 1 - 2% of the incident electron current on C, at the low energies (several eV) of the bulk of the electrons incident on C.

Curve b in Figure 3.2 shows the spectrum obtained from the filament with a negative potential of 22.5 V applied to the filament, to give a mean total accelerating potential of (1.5 + 22.5) V = 24.0 V. The central peak occurs at 24.2 eV. The subsidiary peaks in curve b are due to the scattering of electrons at the edges of the slit, where the electric field was strongest and where most of the accelerated electrons were concentrated. Curve b has a total extrapolated base width of about 4 eV, the same as for curve a, but the extrapolated base width of the central peak alone is only about 1.2 eV. The high energy tail is not present in curve b, as no bias was applied to the collector in this case.

In view of the above tests, the energy analyser was assumed to give quite accurate electron energy spectra under the conditions of the ion-bombardment experiment. Under a given set of experimental conditions the results were reproducible to within a few per cent, the slight difference arising from the difficulty in maintaining precisely the same target surface conditions from run to run. Obtaining the total emission at right angles from the area under the energy spectra (see below for the details), is somewhat less accurate - to within about 5%, due to the difficulties in accurately measuring the actual beam and incident beam currents. The electrons collected by the collector C, were emitted from the target within a range of angles of 90 ± 3.7^{o}, relative to the incident ion beam direction. This angle of acceptance by the collector was determined by the geometry of the analyser. An important limitation on the spherical analyser described above, was the technical difficulty involved in varying the acceptance angle and all results given in this chapter and the next, are for emission at right angles.

From curve b the resolution of the analyser can be estimated to be about 30. This is in good agreement with the value estimated from the geometry of the analyser.

3-2 Experimental Results on Electron Energy Distributions

Figures 3.3, 3.4 and 3.5 show some typical energy spectra of secondary electrons emitted from Pt and Mo targets under bombardment by an assortment of light and heavy ions, over the 10 - 40 keV incident energy range.

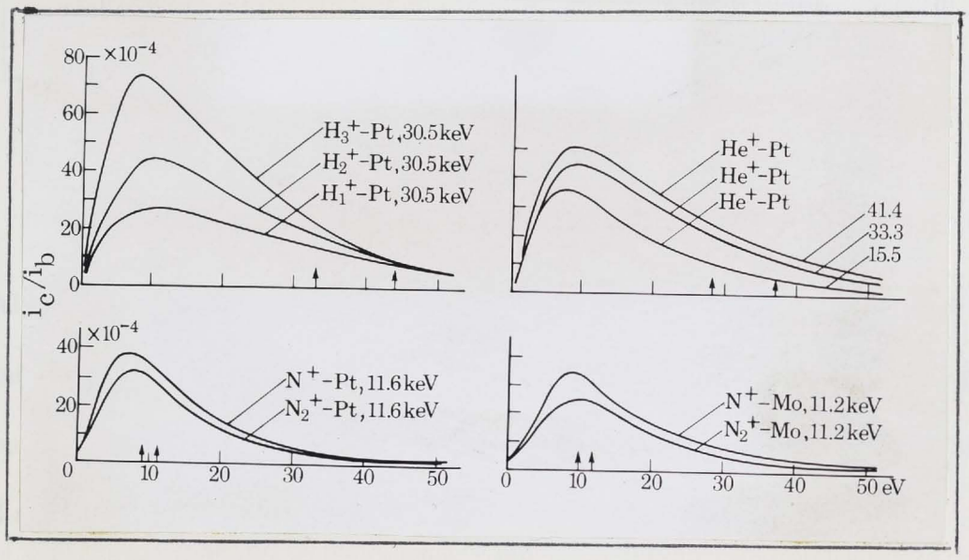

Figure 3.3

Energy spectra for secondary electrons produced by hydrogen, helium and nitrogen ions bombarding platinum and for nitrogen ions bombarding molybdenum.

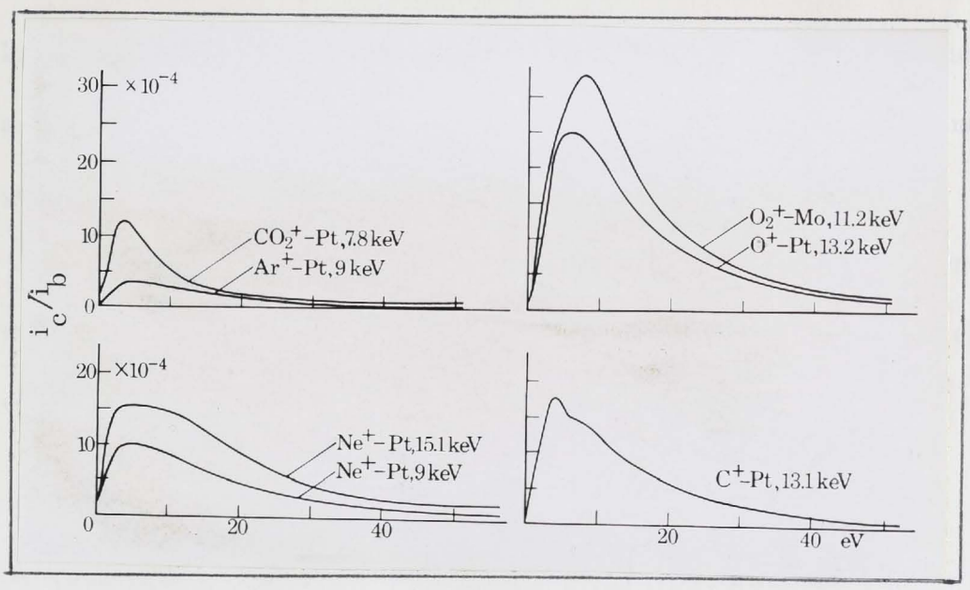

Figure 3.4

Energy distribution for secondary electrons produced by various heavy ions bombarding platinum and molybdenum.

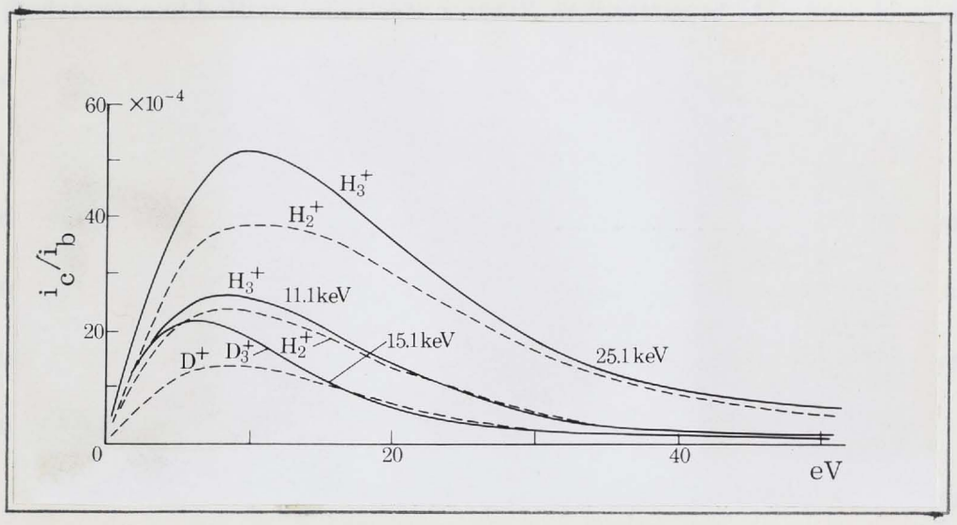

Figure 3.5

Comparison of the energy distributions of secondary electrons by hydrogen and deuterium ions bombarding platinum.

All spectra show the same general characteristics, these being a rapid initial increase to a fairly broad peak, followed by a more gradual decrease up to energies of several tens of electron volts. All spectra peak at energies between 5 and 10 eV.

It should be noted that these spectra are plotted with the normalized collector current as the ordinate. Alternatively, they could be presented with electrons per incident ion per eV as the ordinate. While the latter takes into account the fact that the range of energies ΔE, collector by C, increases linearly with the incident beam energy E, the former represents the actual data as measured and is quite a legitimate representation from the experimental point of view.

Simple particle collision theory predicts that the maximum energy with which singly charged positive ions of mass M and kinetic energy eV can eject electrons from a metal surface is given by:

$$E_{max} = e\left\{\left(\frac{4m_e}{M}\right) V + V_i - \phi\right\} , \qquad (3.1)$$

where ϕ is the work function of the surface, m_e the electron mass and V_i the ionization potential for the incident species. In Figure 3.3 the values of E_{max}

so calculated, are designated by the arrows and one sees that for light ions (hydrogen and helium ions) only a small proportion of electrons have energies exceeding these values. However, for heavier ions, the values of E_{max} calculated from (3.7) lies in the vicinity of the peaks of the distributions. Our discussion in Chapter II showed that the emission of secondary electrons involves many particles necessitating a Thomas-Fermi statistical treatment, and so it is not surprising that (3.7) is so inaccurate, especially for heavy ions where the electronic clouds undergo considerable mutual penetration.

The theory of Izmailov[24] predicts a maximum emitted electron energy of about 1 - 2 eV (section 1-4), well below the values observed in the present work. Also in Chapter II, we saw that his prediction that $\gamma \propto \frac{E_o}{M_1}$ at low energies is not in accordance with observation. Clearly, the electron emission does not arise from release of free conduction electrons by transient fields produced by the incident particle, as he proposed.

Where the incident ion can be scattered from the target with negative charge, the presence of these ions may make some contribution to the spectra in Figures 3.3 to 3.5, particularly to the high energy tails. In Chapter IV we will discuss the spectra of scattered ions in some detail, but indications are that there are few such ions in the energy range up to about 1 keV for heavier ions, while not inappreciable numbers for hydrogen and deuterium ions, especially at the higher incident energies.

In Figure 3.6 are plotted the positions of the peaks in the various electron energy distributions for a Pt target, as a function of incident ion velocity in units of 10^8 cm/sec. There is a definite shift of the peak position towards higher energies as the incident ion velocity increases and, for hydrogen ions at least, there is an apparent slowing down of the rate of peak shift at velocities above about 1.5×10^8 cm/sec. Below this value the curves for hydrogen, deuterium and helium ions come close together. Also, there is some indication that the mean energy of the secondary electrons increases more rapidly with velocity, the heavier the ion, as might be expected from a Russek-Thomas statistical type

process (Chapter I).

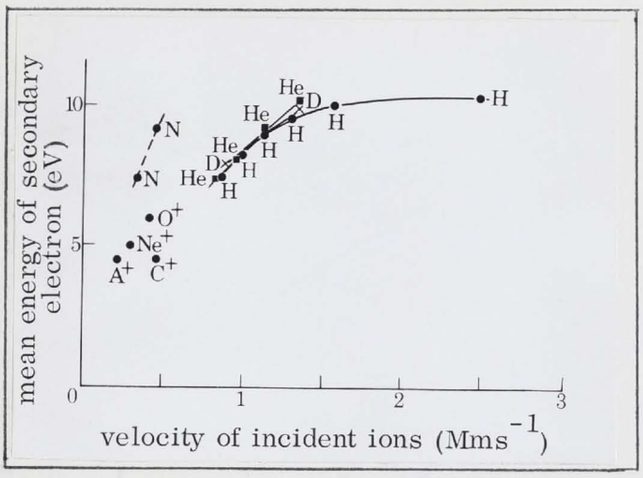

Figure 3.6

The mean energy of secondary electrons produced by various ions from a platinum target as a function of the velocity of the incident ions.

In Figure 3.6 it is assumed that the molecular ions dissociate into their atomic components upon striking the surface: thus H_3^+ at 30.5 keV, for example, was assumed to give a spectrum of the same shape but thrice the height of H_1^+ at 10.2 keV. Thus some of the points labelled 'H' or 'D' were taken from data with molecular ions. This assumption is reasonable in view of the work on total emission characteritstics described in Chapter II.

All the spectra presented in this chapter are for emission at an angle of 90 ± 3.7^{o} relative to the incident ion beam direction. To obtain the emissions over this range of acceptance angles, it was necessary to measure the areas beneath the energy distribution curves plotted as a function of the logarithm of the energy: the emission at 90 ± 3.7^{o} was then proportional to this area for a given spectrum. The factor of proportionality was determined from the scales of the co-ordinate axes and the energy resolution of the analyser. The areas under the energy distributions in Figures 3.3 to 3.5 do not give a measure of the total emission, as they do not allow for the dependence of the energy resolution of the analyser upon the energy of the emitted particles.

In Figure 3.7 are plotted the electron emissions per incident beam particle at 90 ± 3.7^{o}, obtained by the above procedure, for various ions

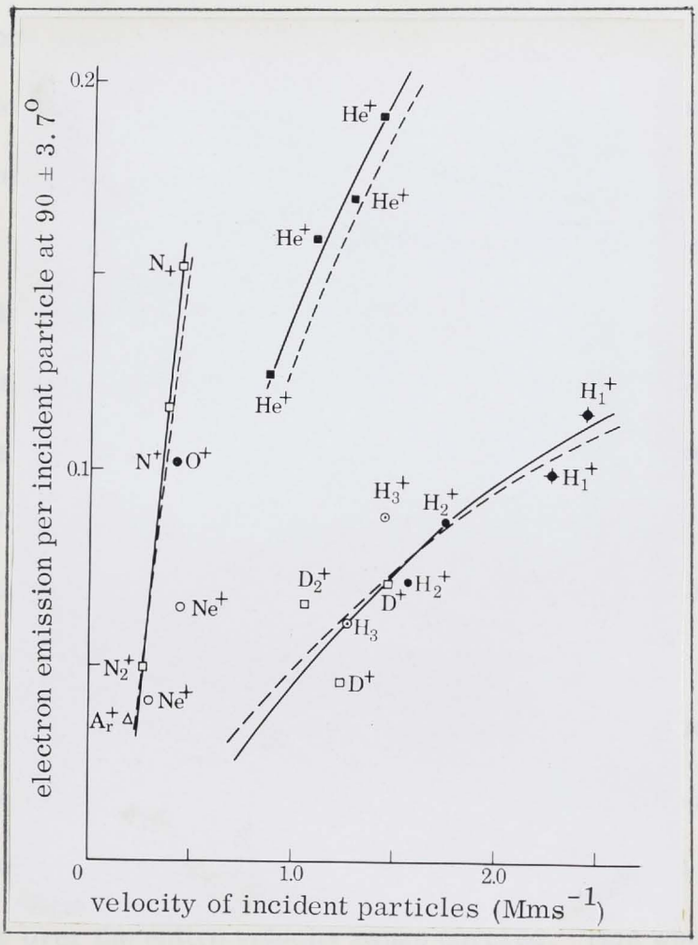

Figure 3.7

Variation of electron emission per incident particle with the velocity of the particle for various ions bombarding a platinum target.

bombarding a Pt target. One sees that they are very similar in shape to the total integrated emission over all angles investigated in Chapter II, i.e., the emission at $90 \pm 3.7^{\circ}$ is closely proportional to the total emission over all angles. When comparing the emissions it is necessary to allow for the difference in the angle of incidence of the incident ion beam on the target. In the total emission observations reported in Chapter II, this angle was 45° while in the present work, it was 75°. In the Appendix, we shall see that the electron emission varies as the secant of the angle of incidence, and so we can write:

$$\frac{\text{emission at } 90 \pm 3.7^{\circ}}{\text{total emission}} \quad \frac{\sec 45^{\circ}}{\sec 75^{\circ}} = k^{-1}, \qquad (3.2)$$

where k is a constant. In Figure 3.7 the dotted curves are drawn from the data on the total emission from Chapter II, with the value for k taken to be 17.

Equation (3.2) permits us to infer something about the angular distribution of the secondary electrons. Clearly the shape of the distribution must be similar for all ion types. Also, the fact that as much as one seventeenth of the total emission is detected at 90 ± 3.7^{o}, would seem to suggest an approximately uniform angular distribution. If the secondary electron emission varied sinusoidally with the angle between the target surface and the direction of observation, as found by Abbott and Berry[31] for He^{+} on W at bombarding energies less than 1 keV, we would not expect nearly as much emission at 90 ± 3.7^{o} in view of the target only being 15^{o} off normal to the incident beam. More will be said about the actual angular distribution of the secondary electrons in the Appendix.

From Figure 3.6 it is seen that the shapes (positions of the peaks) of the secondary electron energy distributions change with incident ion velocity. Also from Figure 3.7, it is seen that the relationship (3.2) holds with considerable accuracy over the entire velocity range covered. This would suggest, although not decisively, that the shape of the energy distributions of the secondary electrons does not change drastically with the angle of observation.

In Figure 3.8 the natural logarithm of the electron emission greater than energy E is plotted as a function of E for two typical energy distributions. The near-linearity of the plots indicates that the energy distributions of the secondary electrons are closely Gaussian with the "electron gas", having temperatures of about $100,000^{o}K$ in these cases.

Figure 3.9, which displays some typical TOTAL negative spectra, is of considerable interest. One sees that the negative ion emission is by no means negligible relative to the electron emission, and for O^{+} on Pt, at 13.7 keV, for example, the ratio of the emissions is as high as 11%. Oxygen is a very electronegative element, however, and for hydrogen ions, the ion emission from a clean, degassed target, is only about 2.5% the magnitude of the electron emission at medium energies. It is clear that accurate, systematic measurements of secondary electron emission must provide for the separation of the electrons from

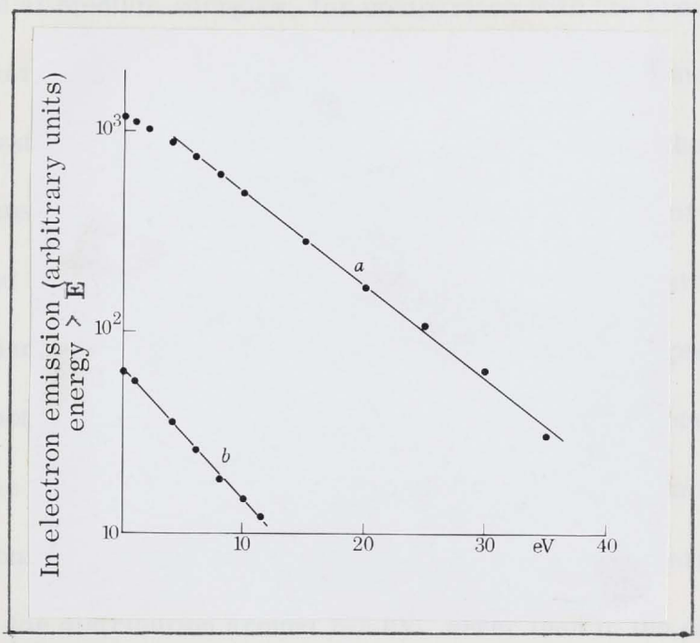

Figure 3.8

Plots of number of electrons with energy in excess of E as function of E:

(a) H_3^+ at 25.1 keV on Pt, $T \approx 110$ K.

(b) O^+ at 13.7 keV on Pt, $T \approx 79$ K.

the scattered negative ions. The measurement of the total secondary negative current to a collector surrounding the target, without magnetic separation, will not suffice. In addition, scattered positive ions need to be clearly separated from the secondary electrons, as discussed in section 2-2 A.

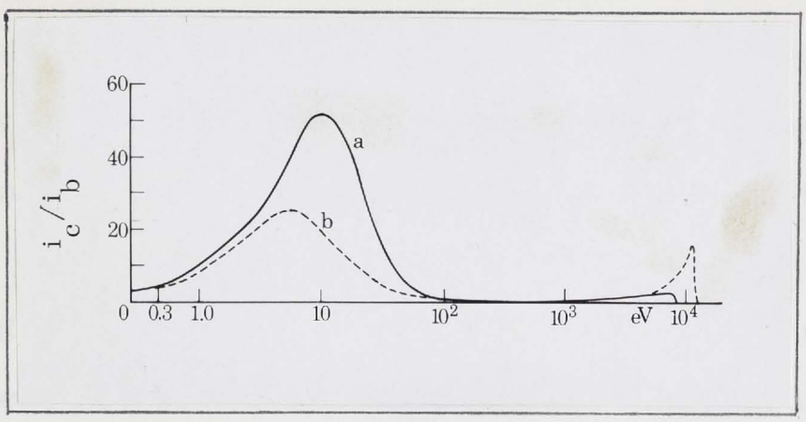

Figure 3.9

The secondary electron and negative ion emission plotted as a function of the logarithm of the energy for

(a) H_3^+ ions on Pt at 25.1 keV, and

(b) O^+ on Pt at 13.7 keV.

The total emissions at 90 ± 3.7^o to the beam direction can be obtained from the areas beneath the curves. The negative ion emissions are: (a) 2.5%, and (b) 11% of the electron emissions respectively.

There are few published results on the energy distributions of kinetic electrons at medium energies, for comparison with the present results. Many researchers have measured the energy distribution integrated over all angles of observation, using retarding potential methods. The inherent uncertainties of such methods were discussed in Chapter II. The work of Abbott and Berry[31] confirmed the present observation that electron energy distributions are close to Gaussian with "temperatures" of the excited "electron gas" in the vicinity of tens of thousands of degrees. Their ion beam energies were somewhat lower than in the present work. Also, many of the published data is presented in the form of electrons per ion per eV plotted against the electron energy in eV. This gives a peak in the distribution around 2-5 eV, lower than in the electrons per ion presentation given here. When plotted in the same units, there is good agreement between the shape of the distributions obtained by various researchers.

We noted above that negative scattered ions (sputtered negative ions are negligible by all indications - Chapters II and IV) may make some contribution to the high energy tails of the measured electron spectra. The fact that there are apparently some electrons with energies in excess of 100 eV (figure 3.9) was explained by Kaminsky[32] on the basis of electron ejection from dense lower bands of the target electron shell structure. Such electrons can emerge with substantial velocity from the metal. As noted in Chapter II, there is little doubt that the theory of Parilis and Kishinevski corresponds best to the physical reality and, of course, no theory based upon the thermal hypothesis could explain the presence of secondary electrons with energies exceeding a few eV.

The secondary electron energy spectra from C^+ and Ne^+ bombardment of Pt (figure 3.4) show evidence of structure with a high energy peak at 8-10 eV apparently superimposed on the main distribution, which peaks at about 4-5 eV. It has been suggested that the double peak for the case of C^+ bombardment arises from the presence of a dilute solution of carbon in the metal. However, this is not indicated by the work on the heavy ion spectra, reported in Chapter IV, and cannot explain the less pronounced, but still fairly definite, double peak for

Ne^+ bombardment.

None of the spectra reveals many electrons with energies close to zero. Thompson[33] (within the context of sputtering) pointed out that many electrons formed within the metal with small or near-zero energies, will be unable to escape the surface binding forces: thus the energy distribution of the emitted electrons will be quite different from that just inside the metal surface. While the former shows a peak at a value determined by the surface forces, the latter will contain many electrons with near-zero energies and, indeed, may possibly increase continuously as the energy approaches zero.

CHAPTER IV

ENERGY DISTRIBUTION MEASUREMENTS II: ENERGY SPECTRA FOR POSITIVE AND NEGATIVE SCATTERED IONS

4-1 Experimental Considerations

The analyser used in these measurements has been described in the previous chapter. The essential differences for positive ion analysis lay in:

(a) The higher potentials required to be applied to the deflecting (hemispherical) electrodes, in order to focus the scattered ions from the target on to the collector, and

(b) The necessity of applying a positive bias on the collector in order to suppress electron emission from it.

The higher potentials on the deflecting electrodes are necessitated by the much higher mean energies of the scattered ions, compared to the secondary electrons. This is clearly shown by the composite negative spectra, Figure 3.9, Chapter III. From equation (1.25), Chapter I, we see that for light ions, the maximum energy of the scattered ions is very nearly that of the incident ions: even for heavier ions the majority of scattered ions, for incident beam energies of several keV or more, have energies well into the keV range. On the other hand, our work reported in Chapter III showed that few secondary electrons have energies in excess of several tens of electron volts.

The maximum potential which could be applied between the hemispheres was about 6 kV and this limited us, for complete spectra, to incident ions of energy E_o and charge q, such that $\frac{E_o}{q} < 6 \times 2.56 \simeq 15.5$ keV. For heavier ions, this energy exceeded the limit set by the maximum field available in the bending magnet for ion sorting the beam prior to entry into the detector chamber (see Appendix).

For ion scattering, the problem of electron emission from the collector was much more serious than for electron emission, as the value of the electron coefficient γ is of the order of unity for ions of several keV incident upon metal surfaces (Chapter II). It was necessary to make the collector quite shallow in

order to collect the scattered ions from the target, over the large solid angle permitted by the hemispherical analyser. It was found that a positive bias of 10 volts on the collector was sufficient to suppress most of the electron emission from it. The current reaching the collector was usually of the order of 10^{-11} amp., or about 10^{-4} of the incident current to the target. With the rather conventional measuring apparatus employed for these observations, the lowest current measurable above the noise level was about 10^{-13} amps. A bias of 15 volts or more was found to increase the leakage current to the collector significantly above the noise level: thus only a moderate bias of 10 volts was applied to the collector. Possible errors arising from the escape of high energy electrons from the collector are discussed in section 4-2. While the bias on the collector reduced the total collector current by about half, as expected, it did not change the shape of the energy distributions appreciably.

Over two hundred ion spectra were taken during the program discussed in this chapter. The bulk of spectra presented were made on metal targets maintained at a red heat in a good vacuum (of about 2×10^{-8} mm of mercury) to assure surface cleanliness (see Appendix I).

The necessity for surface cleanliness is shown by a comparison of the spectra from contaminated targets, i.e., targets freshly placed in the vacuum, with those from properly degassed targets. In Figure 4.1, (1) and (2) it is possible to trace the change in the positive ion spectra for protons incident on Pt at about 8 keV energy. For a freshly introduced target (which is invariably contaminated) the ion spectra show a broad maximum at about half the maximum, with a much smaller maximum at about 7 keV scattered ion energy. As the surface is cleaned, the latter peak grows relative to the former. The absolute size of the higher energy peak does, however, change little until the target is flashed to a white heat for a few moments and maintained at a bright red heat for several hours at least. In Figure 4.1 (1) the spectrum b is remarkably different, both in magnitude (area) and shape from the spectrum a for the contaminated target. The half energy peak for a contaminated target is sharply reduced, even by a

mild heating of the target for a few minutes. This peak is clearly due to scattering from contaminants, or possibly to ionized contaminants knocked off the surface by the bombarding beam. However, why such processes should result in a peak at near half-energy is not clear. The degassed target contains no evidence of any half energy peak, but only a single shape peak at an energy close to the maximum ($E_{peak} \simeq 0.95\ E_{max}$). Figure 4.1 (3) shows the effects of surface cleanliness upon the spectrum of a heavier incident ion - N_2^+ on Ni in this case. For a contaminated surface freshly introduced into the vacuum system, there is no sign of a peak due to elastically scattered particles, but only a rather broad peak at low energies. However, as the target is heated, the elastic peak appears and becomes increasingly prominent. While the low energy peak also grows, the elastic peak and the proportion of high energy scattered ions in general, increase even more markedly.

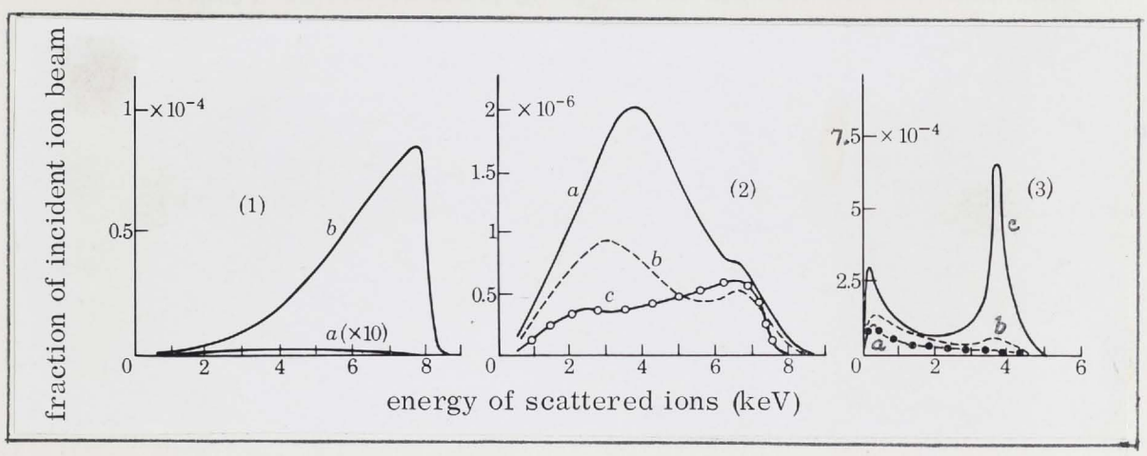

Figure 4.1

Effects of contamination of target surface on the energy distribution of particles scattered with positive electric charge.

(1) H^+ on Pt at 8.2 keV: (a) fresh contaminated target;
(b) target degassed and kept at red heat.
Pressure 20 μ Torr.

(2) H^+ on Pt at 8 keV: (a) fresh target;
(b) 24 h in vacuum;
(c) mild heating for few minutes.
Pressure 20 μ Torr.

(3) N_2^+ on Ni at 11.6 keV: (a) fresh target;
(b) red hot for 5 min, cooled;
(c) red hot for 15 min, cooled.
Pressure $\sim$ 1 μ Torr.

Once a surface was properly degassed it did not return to the contaminated conditions indicated by the spectra in Figure 4.1 (1) a and (3) a, provided it was not removed from the vacuum. However, for heavy ions, the elastic peak did decrease in absolute intensity over a period of days, if the target was left cold in the vacuum, while the low energy peak (where one occurred) remained relatively unchanged.

In our semi-theoretical discussion in Chapter I, we saw that an ion bombarding a solid loses energy by two competing processes - inelastic losses due to interactions with electrons and losses due to collisions with lattice atoms. Equations (1.11) and (1.12) express the respective stopping cross sections S_e, S_n for these processes using a Thomas-Fermi statistical model of the atom. Both equations are sufficiently accurate to provide us with a semi-quantitative explanation of the observed energy spectra.

We may, for convenience, group the ion spectra into two main categories, those from light ion and those from heavy ion bombardment. Although this division is somewhat arbitrary, it forms a very useful basis for presentation and discussion of our results.

4-2 The Spectra of Light Ions; Experimental Results and Discussion

From Table 1.1, Chapter I, we see that the light ions H^+ and He^+ lose most of their energy in inelastic collisions with the electrons of the solid and this results in a general broadening of the spectra. The equations for elastic collisions (1.25) and (1.26) indicate that for light ions ($\mu \gg 1$) the incident particle loses very little energy in a single elastic collision. In the particular experimental arrangement employed for these experiments, $\theta_1 = 90 \pm 3.7^o$, and so (1.25) becomes:

$$\frac{E_1}{E_o} = \frac{1}{(1+\mu)^2}\left(\pm \sin 3.7 + \sqrt{\mu^2 - \cos^2 3.7}\right)^2$$

$$\simeq \frac{M-m}{M+m} \pm \frac{\sin 3.7}{(1+\mu)^2}, \quad (\mu \gg 1) \qquad (4.1)$$

where M and m are the masses of the target atom and incident ion respectively.

Now the second term on the right hand side of (4.1) is at least five orders of magnitude less than the first term and so the spread in the spectra arising from the finite acceptance angle of the analyser is negligible.

The main contribution of elastic scattering events is to deflect or "back-scatter" the incident light particles out of the target and in Chapter I some theoretical discussion was given, based upon this "one deflection model".

Figure 4.2 shows energy distributions for ions scattered with positive charge from a hot platinum target bombarded by H^+, H_2^+ and H_3^+ at various energies covering a range of from 3 to 15 keV per particle. The spectra are all sharply peaked, with $\frac{E_{peak}}{E_{max}} \simeq 93\%$ on the average, and the majority of scattered ions possessing energies exceeding 78% of the incident beam energy.

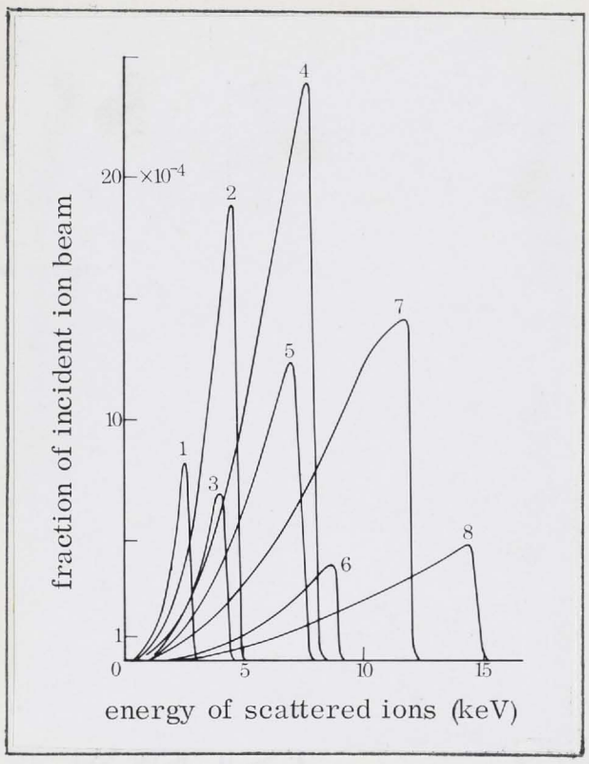

Figure 4.2

Energy spectra of hydrogen particles scattered at $90 \pm 3.7^{\circ}$ with positive charge from a platinum target at various bombarding energies:

(1) H_3^+ at 9.1 keV; (2) H_3^+ at 15.1 keV;
(3) H_2^+ at 9.1 keV; (4) H_3^+ at 25.1 keV;
(5) H_2^+ at 15.1 keV; (6) H^+ at 9.1 keV;
(7) H_2^+ at 25.1 keV; (8) H^+ at 15.1 keV.

(The incident beam energy per particle is equal to the maximum energy, E_{max}, of the light scattered ions, to within the limits of accuracy of the analyser and measuring apparatus.) There are very few scattered ions with energies less than about 10% of E_{max} but a thorough search for low energy ions, using a 300 volt acceleration bias on the target, showed that a very small number are scattered with down to nearly zero energies.

All the spectra in Figure 4.2 have the same general shape, as would be expected if the molecular ions dissociated into their atomic components upon striking the target. The fact that the spectra are not even more sharply peaked near the E_{max} values and that E_{peak} is closer to 93% (average value) of E_{max} than the 99% of E_{max} predicted from equation (4.1) for elastic collisions, arises, as we noted, from inelastic energy losses within the metal.

Figure 4.3 shows some corresponding energy distributions for a Ni target and in this case E_{peak} is, on the average, about 81% of E_{max}, well below the 97% of E_{max} value expected from (4.1) for elastic collisions. This is possibly due to the deeper mean penetration depth for light ions in Ni (equation (1.34)).

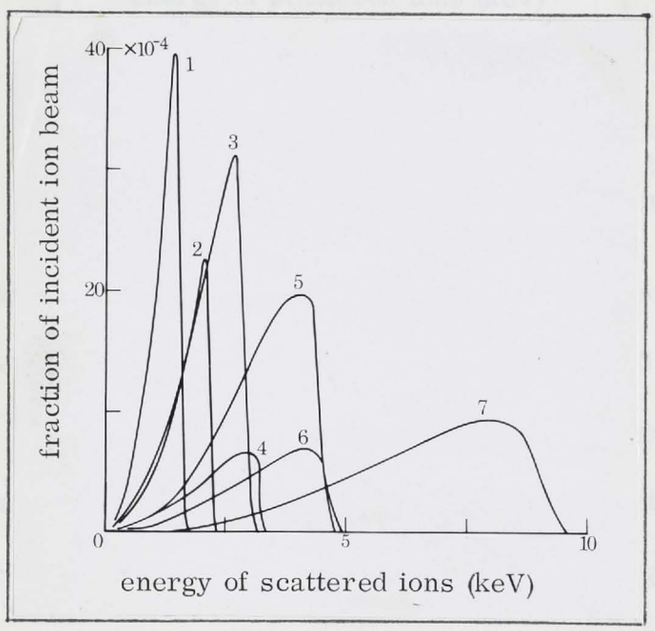

Figure 4.3

Energy spectra of hydrogen particles scattered at 90 ± 3.7^{o} with positive charge from a nickel target at various bombarding energies:

(1) H_3^+ at 4.9 keV; (2) H_2^+ at 4.9 keV; (3) H_3^+ at 9.5 keV;
(4) H^+ at 3.4 keV; (5) H_2^+ at 9.5 keV; (6) H^+ at 4.9 keV;
(7) H^+ at 9.5 keV.

Figure 4.4, for a molybdenum target, shows a hump in the energy distributions of scattered protons at approximately half the E_{max} values. In section 4-1 it was pointed out that the presence of a half-energy peak indicates surface contamination, and so the Mo target surface was probably not wholly free of contaminants. The half-energy hump was not removed from the spectra, even by prolonged baking of the target to a red heat, interspersed with flashing to a white heat.

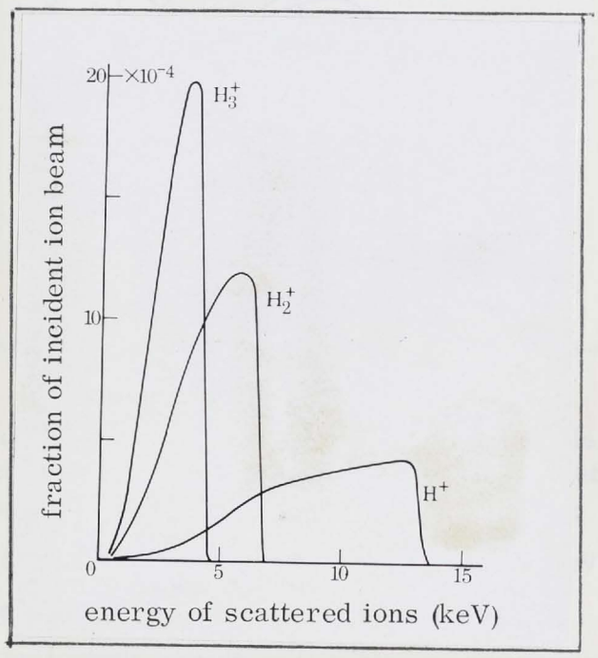

Figure 4.4

Energy spectra of hydrogen particles scattered at 90 ± 3.7^{o} with positive charge from a heated molybdenum target at 13.5 keV bombarding energy.

Figures 4.5, 4.6 and 4.7 show some energy spectra of negatively charged particles scattered from a Pt target in the 90 ± 3.7^{o} direction, with incident H^{+}, H_2^{+} and H_3^{+} beams respectively. Clearly the scattered particles consist almost entirely of H^{-} as E_{max} is, in all cases determined by the incident energy per particle rather than by the total incident energy.

The negative spectra are considerably broader than the positive spectra shown in Figure 4.2, and at higher incident ion energies, there are considerable numbers of low energy scattered ions. The latter feature clearly distinguishes the negative from the positive spectrum for the same incident ion beam energy. The increase in collector current at low energies is due to the entry of secondary

electrons and so it is not possible to ascertain the numbers of very low energy (a couple of hundred eV, or less) negative ions.

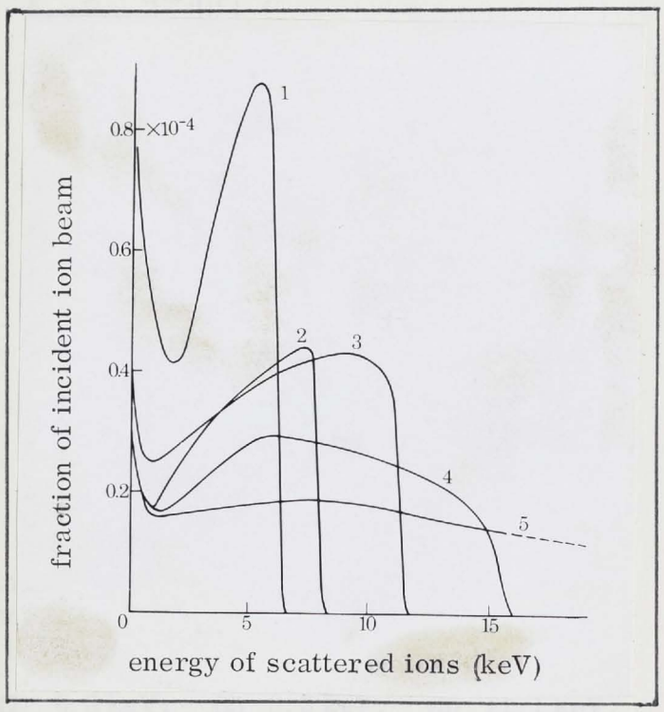

Figure 4.5

Energy spectra of negatively charged particles scattered at 90 ± 3.7° from a platinum target bombarded by protons at various energies:

(1) 6.3 keV; (2) 8.3 keV; (3) 11.6 keV

(4) 15.8 keV; (5) 30.5 keV.

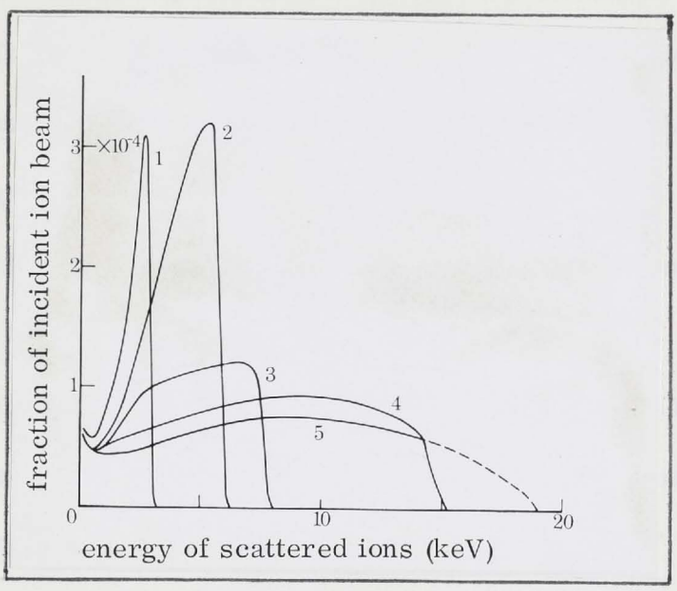

Figure 4.6

Energy spectra of negatively charged particles scattered at 90 ± 3.7° from a platinum target bombarded by H_2^+ ions at various energies:

(1) 6.3 keV; (2) 11.6 keV; (3) 15.8 keV;

(4) 30.5 keV; (5) 39.1 keV.

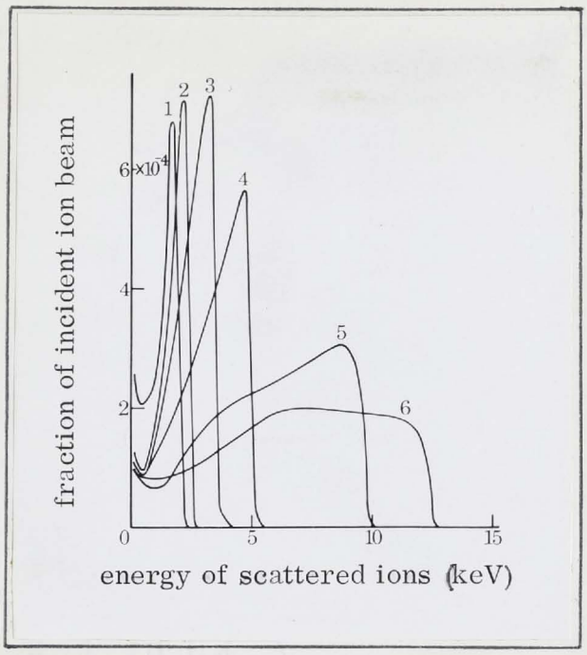

Figure 4.7

Energy spectra of negatively charged particles scattered at 90 ± 3.7° from a platinum target bombarded by H_3^+ ions at various energies:

(1) 6.3 keV; (2) 8.3 keV; (3) 11.1 keV;

(4) 15.3 keV; (5) 30.5 keV; (6) 39.1 keV.

The negative spectra for a Ni target (Figure 4.8) are also considerably broader than the corresponding positive spectra, but there are fewer low energy negative ions than for platinum.

The energy spectra of positively and negatively charged deuterium ions are shown in Figures 4.9 and 4.10. The general trends are the same as for hydrogen ions, these being:

(1) Negative spectra are generally broader than positive spectra at the same incident ion beam energy.

(2) The broadening for both negative and positive spectra increases with incident beam energy, slightly for positive spectra, but very markedly for negative spectra.

In Chapter I it was shown that the broadening of the spectra of back-scattered particles is NOT a result of multiple elastic collisions, although this explanation has been advanced by several researchers[9]. Multiple collisions only have a second order effect on the spectra.

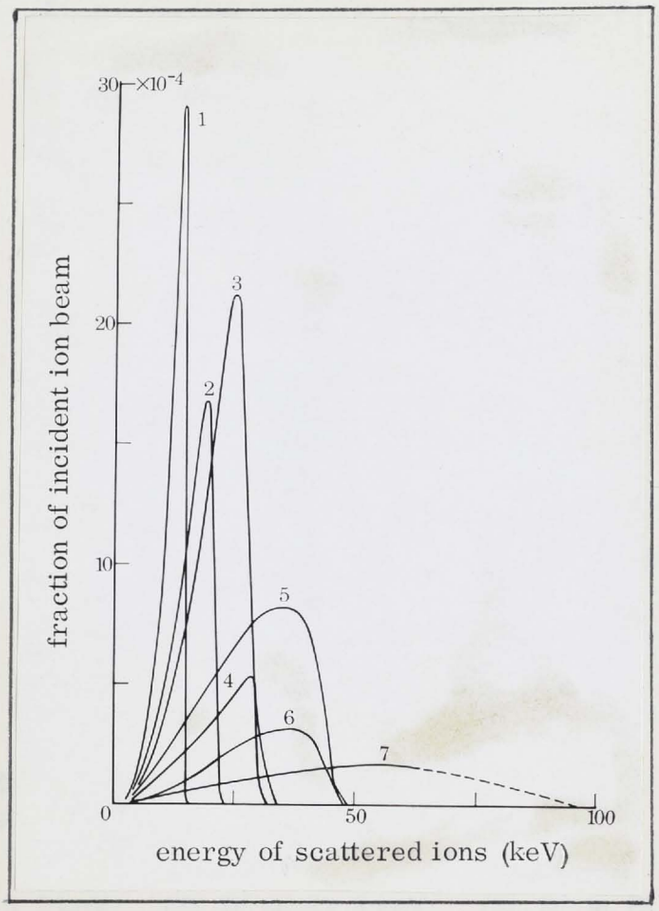

Figure 4.8

Energy spectra of negatively charged particles scattered at 90 ± 3.7° from a nickel target bombarded by hydrogen ions:

(1) H_2^+ ions at 4.9 keV; (2) H_2^+ ions at 4.9 keV;

(3) H_3^+ ions at 9.5 keV; (4) H^+ ions at 3.4 keV;

(5) H_3^+ ions at 9.5 keV; (6) H^+ ions at 4.9 keV;

(7) H^+ ions at 9.5 keV.

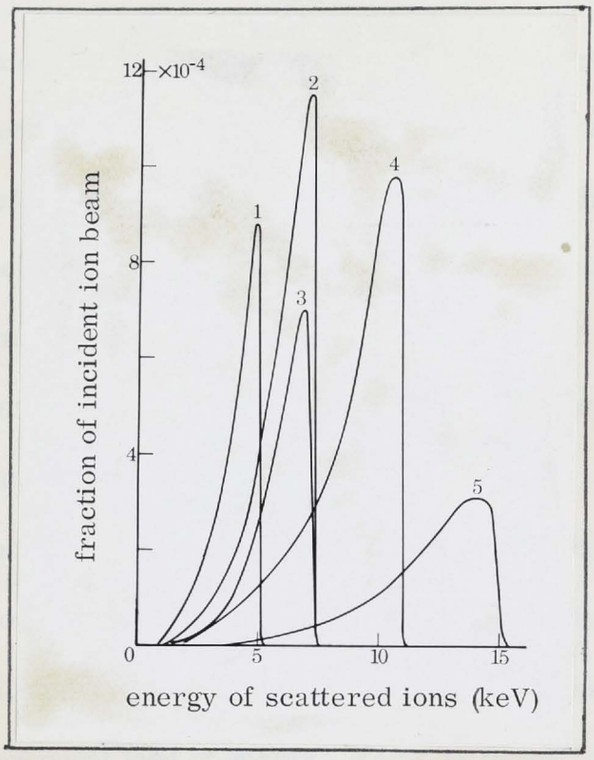

Figure 4.9

Energy spectra of positively charged particles scattered at 90 ± 3.7° from a platinum target bombarded by deuterium ions:

(1) D_3^+ at 15.1 keV; (2) D_3^+ at 22.3 keV; (3) D_2^+ at 15.1 keV;

(4) D_2^+ at 22.1 keV; (5) D^+ at 15.1 keV.

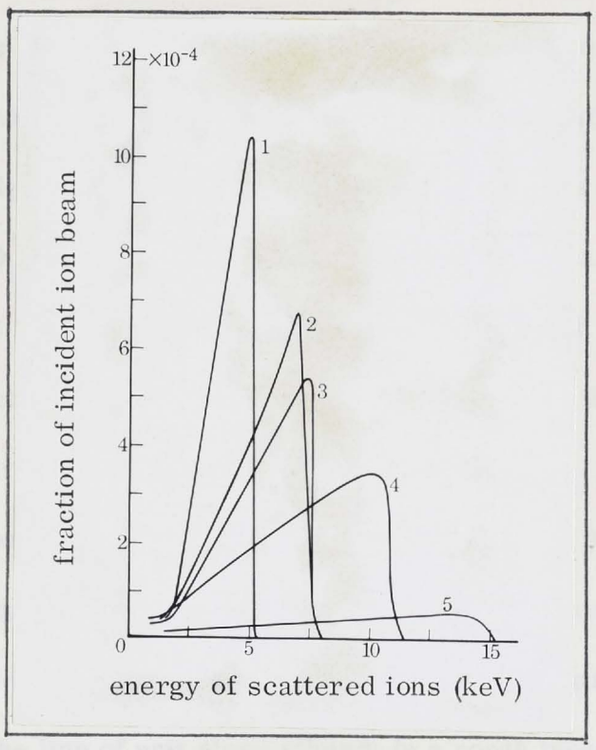

Figure 4.10

Energy spectra of negatively charged particles scattered at 90 ± 3.7° from a platinum target bombarded with deuterium ions:

(1) D_3^+ ions at 15.1 keV; (2) D_3^+ ions at 22.1 keV; (3) D_2^+ ions at 15.1 keV;

(4) D_2^+ ions at 15.1 keV; (5) D^+ ions at 15.1 keV.

From equation (1.32) it follows that the smaller the value of E_s, the energy of the emergent ion, the greater is the penetration depth, x_c, of the incident ion before it is scattered out of the target. Or from (1.34) the "average" penetration depth (path length) $\bar{x}_c$ increases with decreasing value of the maximum E_m (or E_{peak}). Thus the broadening of the spectra with increasing energy is probably a reflection of the increasing mean penetration depth of the incident ions.

The property (1) above, the fact that negative ion spectra are broader than positive ion spectra at the same incident ion beam energy, may be a result of the probability of capturing an additional electron depending upon the penetration and consequent loss of energy. For a Pt target, where the broadening is very pronounced at higher energies, the relatively large numbers of slow (less than 10% of E_{max}) negative particles, is also suggestive of appreciable penetration. It should be noted that the term "appreciable" is used here in a strictly relative sense, to indicate several atomic layers at the surface: the penetration is still much less than that involved, for example, in channelling phenomena and ion scattering is basically a surface, rather than a bulk, process.

In Figure 4.9 it should be noted that the values of E_{peak} and E_{max}, for incident D_2^+ ions at 15.1 keV, are very nearly the same as the values for D_3^+ ions at 22.3 keV. This is what would be expected if the molecular ions dissociated into their atomic components upon striking the surface.

Figures 4.11 and 4.12 plot the values of E_{peak} against the incident energy per particle (which is the same as E_{max} within the accuracy of these measurements), for both hydrogen and deuterium ions on the various targets. From our previous discussion, it follows that the deviation of the values of E_{peak} from the line of unit slope (dotted) is a rough measure of the broadening of the spectra for these lighter ions. (Alternatively the widths of the spectra at half maxima height could be plotted against E_{max}, to obtain an indication of broadening). The broadening of the negative spectra of higher energy protons on Pt is quite pronounced.

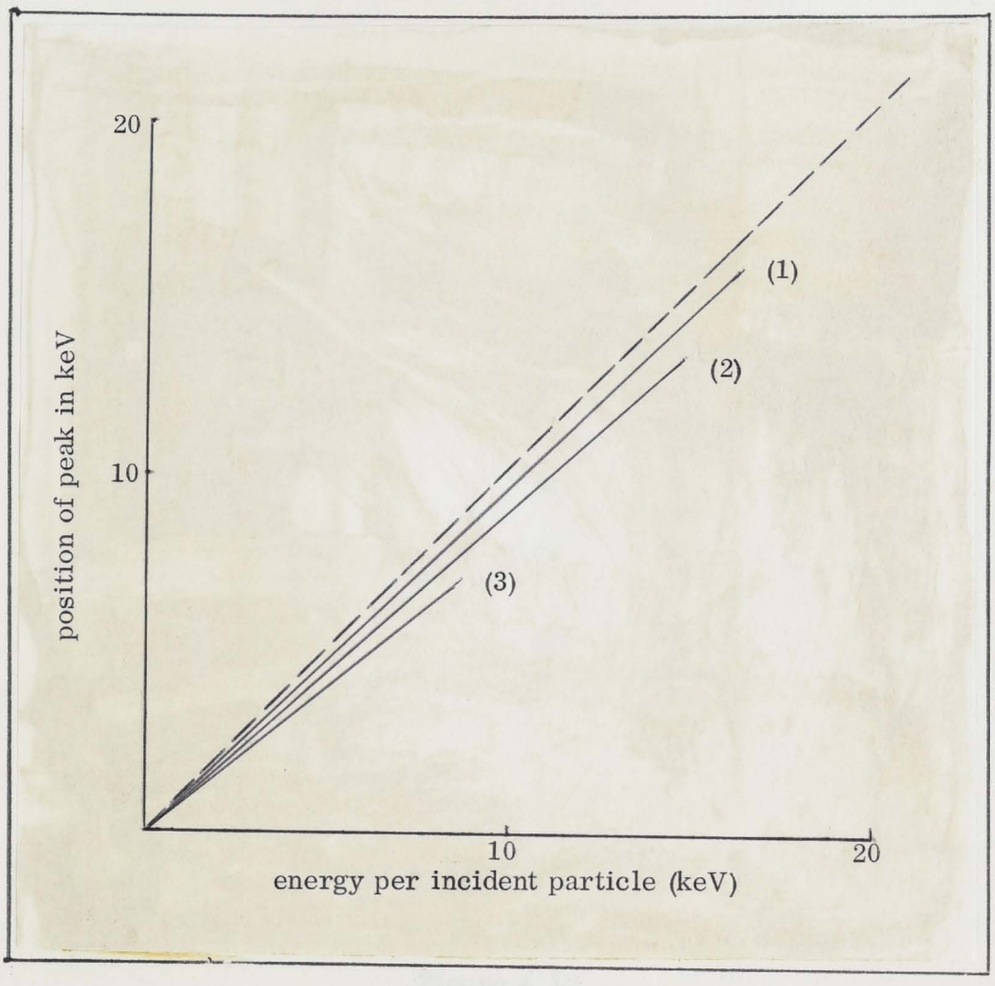

Figure 4.11

E_{peak} plotted against the energy per incident particle, for positive spectra of light ions.

(1) D^+ on Pt

(2) H^+ on Mo

(3) H^+ on Ni

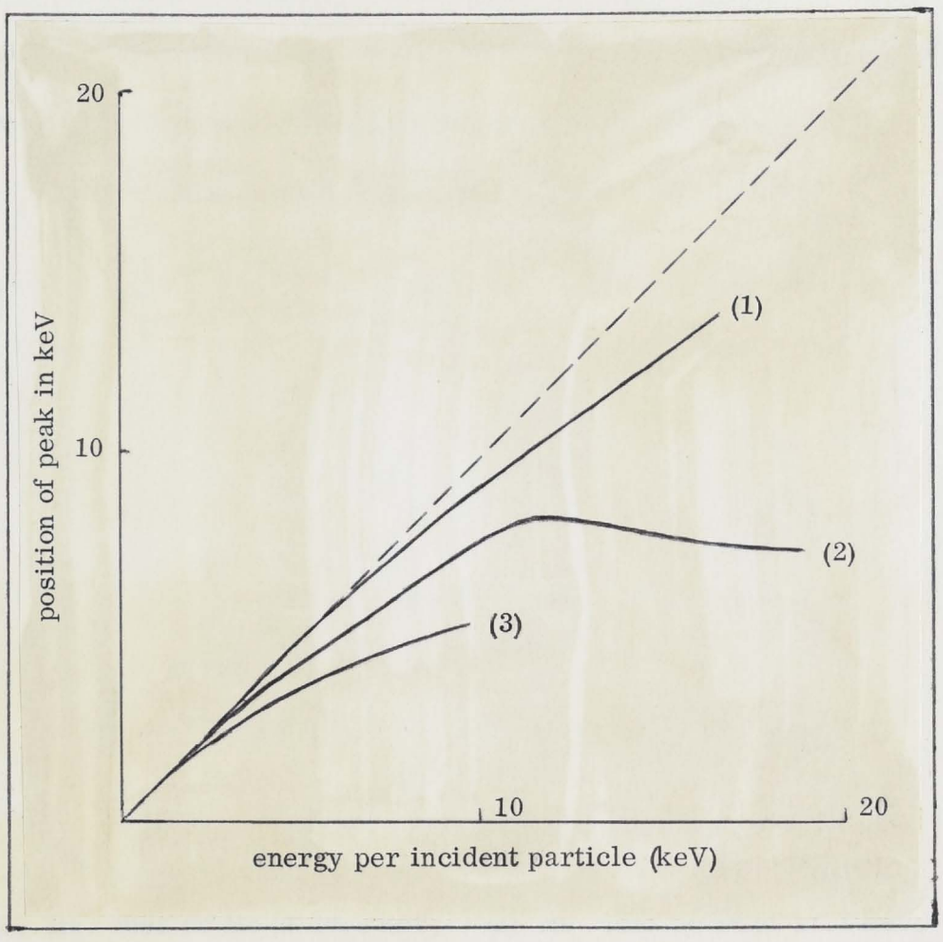

Figure 4.12

E_{peak} plotted against the energy per incident particle for negative spectra of light ions.

(1) D^+ on Pt
(2) H^+ on Pt
(3) H^+ on Ni

Incident helium ions are only scattered with positive charge due to the high ionization potential of the helium atom. The spectra, shown in Figure 4.13, are somewhat narrower than for incident hydrogen or deuterium ions, especially for a Pt target. For a Pt target, there are very few scattered ions with energies below half the maximum. From Table 1.1, Chapter I, we see that for helium ions, approximately 15% of the energy loss rate arises from elastic collisions at 10 keV, their velocities being only half those for protons at the same energy. Thus they will not penetrate into the target as far as protons before being back-scattered and they will lose less energy in quasi-continuous inelastic processes. However, the mass ration, μ, is still

$\gg$ 1 and so the energy loss in discrete elastic collisions will still be quite small. This explains the absence of low energy ions and the peaks of the spectra occurring close to the maximum energies of the spectra.

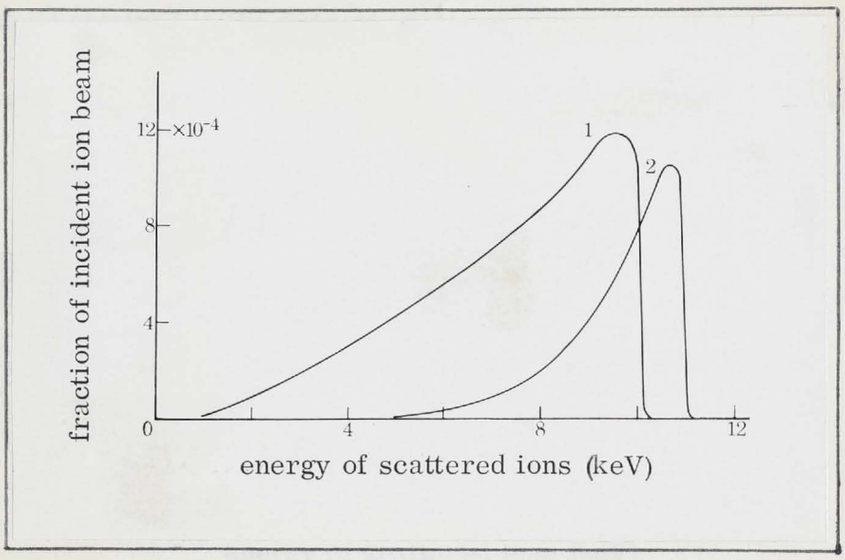

Figure 4.13

Energy spectra of positive charged particles scattered at 90 ± 3.7° from molybdenum and platinum targets: (1) He^+ ions on Mo at 10.5 keV; (2) He^+ ions on Pt at 11.1 keV.

The energy spectra for scattered light ions at medium energies have been recently measured by Morita et al.,[10] and Mashkova et al.,[9]. Neither of these groups measured spectra of ions scattered with negative charge and most of their work was performed at scattering angles $\leq 60^\circ$, while the angle is close to 90° for the present work. With $\theta_1 = 60^\circ$ and $\phi = 45^\circ$ (typically), the factor $1 - \cos\phi \sec(\theta_1 + \phi)$ in the denominator of (1.34), becomes equal to about 3.5, while for the case $\theta_1 = 90^\circ$ and $\phi = 15^\circ$ (present work), the factor becomes equal to about 4.8. Thus the fact that the spectra of Morita and Mashkova are somewhat broader and more dome shaped than those presented here, probably arises from the greater mean penetration depth for their data. We noted above that the inelastic energy losses and hence the broadening of the spectra increases with the ion penetration.

The present work showed no indication of a sharp "spike" very close to E_{max}, as reported by Mashkova.

Panin[34] also measured spectra for light (and heavy) ions in the

7.5 - 30 keV region with $\theta_1 = 90^o$, as in our case. However, his surfaces were apparently contaminated, rendering his spectra with light ions, particularly, difficult to interpret. Figure 4.14 compares some of Panin's light ion spectra with those obtained in the present work.

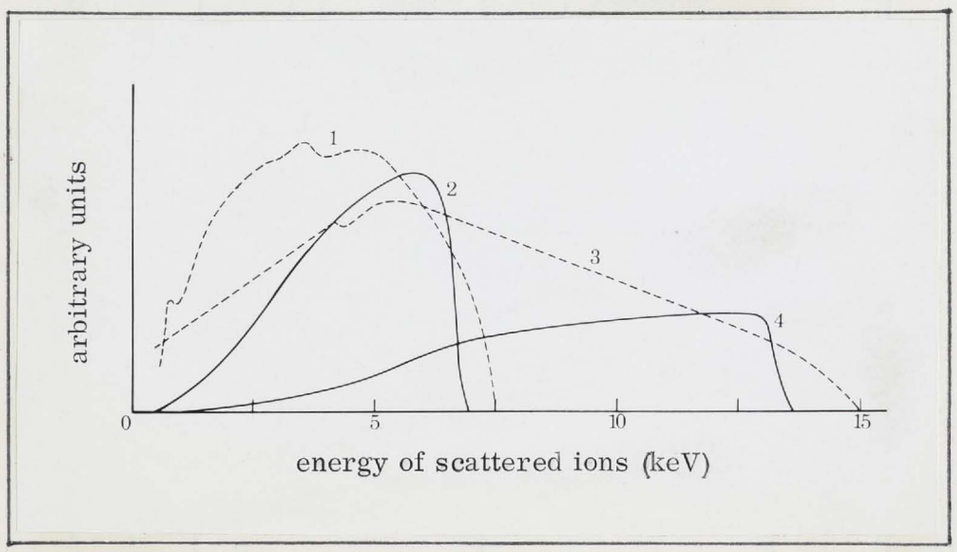

Figure 4.14

Energy spectra of positively charged hydrogen ions scattered at 90^o to beam direction from a molybdenum target:
(1) H^+ at 7.5 keV, according to Panin[34]; (2) H_2^+ at 13.5 keV;
(3) H^+ at 15.0 keV, according to Panin[34]; (4) H^+ at 13.5 keV.

Using the procedure outlined in Chapter III, we can obtain the total ion emission in the solid angle at 90 ± 3.7^o to the incident beam, by measuring the areas of the energy spectra plotted against the logarithm of the energy (or the areas of the energy spectra with emission per incident particle per unit energy plotted on the vertical co-ordinates). The areas, in the appropriate units, are multiplied by 30, the calculated and measured resolution of the analyser (see Chapter III for details). Figure 4.15 plots the total emissions thus derived, as a function of incident ion energy, for hydrogen ion bombardment of Pt and Ni targets.

From Figure 4.15, the scattering with positive charge increases monotonically with energy, over the range covered, while scattering with negative charge increases to a maximum in the 3 - 8 keV region and then decreases.

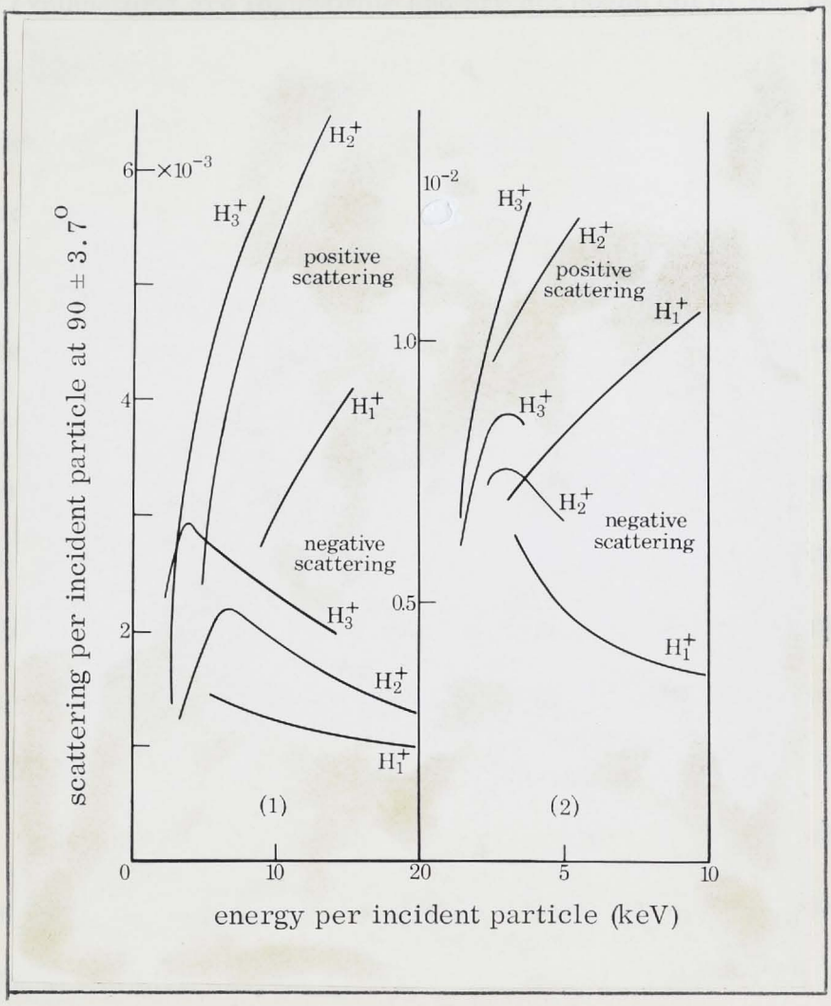

Figure 4.15

Total scattering of hydrogen particles at 90 ± 3.7°, with positive and negative charge, as a function of bombarding energy, for platinum and nickel targets.

The total scattering with charge is, in all cases, about twice as great for Ni as for Pt and, at a given energy per incident particle, the positive and negative ion emissions increase in the order H^+, H_2^+, H_3^+ for both targets.

In Chapter II we found that the total scattering from Pt is considerably greater than from Ni, due to the greater Z_2 value of the former. Yet the scattering with charge is greater for the Ni target. The inference is that nearly all particles scattered from a Pt target are neutrals and hence are not detected by the electrostatic energy analyser.

The non-coincidence of the scattering curves for H^+, H_2^+ and H_3^+ in Figure 4.15, would seem to indicate that the neutral dissociation products from the incident molecular ions are scattered with less energy than the singly ionized products, or that the neutral products are scattered more efficiently as protons than the singly ionized products. From basic physical considerations

these explanations are improbable and are not borne out by our observations on the total apparent ion scattering (Chapter II). Our previous work indicates an equi-partition of energy between products, whenever dissociation of a molecular ion occurs at a metal surface, and in this chapter, we have seen that the shapes of the energy spectra depend upon the incident energy per particle (e.g., the positive spectrum for D_2^+ ions at 15.1 keV has the same E_{peak} and E_{max} values as the positive spectrum for D_3^+ ions at 22.3 keV, in Figure 4.9) and not on the number of particles in an incident ion. The indications, therefore, are that some systematic error was involved in the collection of the scattered ions - possibly there was some escape of fast secondary electrons from the collector. Systematic measurements using a particle counter detector should decide this question.

The monotonic increase in the scattering with positive charge over the 3 - 20 keV energy range is in agreement with the observations of Morita et al., who found a similar increase for proton scattering from Cu and Au targets, for energies up to 40 keV and for the conditions $\theta = 45^o$ and $\phi = 90^o$. At 40 keV their scattering curves flattened out. Our results in Chapter II showed that the total apparent ion scattering decreases at incident ion energies in excess of about 20 keV for a Pt target (Figure 2.32). Thus the scattering with positive charge cannot continue to increase indefinitely, but must show a maximum in the tens of keV region. The well defined maximum in the scattering with negative charge curves (Figure 4.15) is very interesting, and is suggestive of a resonant process for the formation of negative ions. The equilibrium H^- current produced by passing a proton beam through most gases also peaks at about 10 keV[14].

The above observations are confirmed by the deuterium data, although the negative scattering maximum occurs at a slightly higher energy.

We will now use the results reported in Chapter II for the total apparent scattering, in conjunction with the present results on scattering with electric charge at 90 ± 3.7^o, to estimate roughly the proportion of incident ions scattered

as neutral atoms from the metal surface. This is important as the electrostatic analyser was unable to analyse neutral scattered atoms and interpretation of the results for scattered ions is complicated by electron capture and loss processes in the metal. From equations (2.9) and (2.12), Chapter II, we can write:

$$R = (\rho_+ - \rho_-) + \gamma'_c(\rho_+ + \rho_- + \rho_m) + s_+ + \gamma_s(s_+ + s_-) , \qquad (4.2)$$

where the various coefficients were defined. (ρ_+, ρ_- and ρ_m are the fractions of the incident beam scattered as positive ions, negative ions and as neutral atoms respectively).

A consideration of the light ion spectra presented in this section indicates that sputtered ions must be completely absent or, if present, comprise only a very small fraction of the total secondary current reaching the collector. In Chapter I we saw that the mean energies of sputtered target atoms is only of the order of a few eV and using the random collision model, the maximum energy of sputtered Pt particles under H^+ bombardment is only $E_o W_{12} \simeq 0.02\, E_o$ (equation (1.53)). The spectra presented in this section all contain very few ions at such low energies, and so we can take the coefficients s_+ and γ_s as being negligible compared to the ion scattering coefficients. Thus (4.1) becomes:

$$R = \rho_+ - \rho_- + \gamma'_c(\rho_+ + \rho_- + \rho_m) . \qquad (4.3)$$

Here it is assumed that the energy distributions for the scattered incident particles are qualitatively the same for all charge states, so that the electron emission coefficient γ'_c is the same for all scattered particles and is the value appropriate to the distributions. This is, of course, not strictly true as the negative ion spectra are considerably broader than the positive ion spectra at the same incident particle energy. Still, to a first approximation, we can accept (4.3) as correct, remembering that our discussion is only intended to be semi-quantitiative, and write for the fraction of particles reflected as neutrals:

$$\rho_m = \frac{R - (\rho_+ - \rho_-) - \gamma'_c(\rho_+ + \rho_-)}{\gamma'_c} \quad . \tag{4.4}$$

To obtain ρ_+ and ρ_- from the emissions at 90 ± 3.7^o, it is necessary to assume some known form for the angular distribution of the scattered particles: this gives the numerical factor by which to multiply the emissions at 90 ± 3.7^o to obtain estimates for ρ_+ and ρ_-. In fact, however, the precise form of angular distribution assumed does not alter the basic conclusions to be reached. For Coulomb scattering, the factor is 9.5, while for isotropic (uniform at all angles) it is 21.

The values of the electron emission coefficient γ'_c, for the Ni collector employed in the measurement of the total apparent scattering, can be estimated from the data on the secondary emission of electrons presented in Chapter II. The values of the total apparent scattering coefficient, R, can be obtained from Chapter II. For the measurement of energy spectra, the target orientation is approximately 75^o with respect to the incident beam, whereas in the apparatus for measuring the coefficient, R, in Chapter II, the target orientation was approximately 45^o. In deriving the values for ρ_m plotted in Figure 4.16, no allowance is made for this difference, but again, the basic conclusions will not be altered.

The values of ρ_m thus obtained, are plotted in Figure 4.16. It must be reiterated that the values are subject to considerable uncertainty, due to the assumptions mentioned above, regarding the angular functions of the scattered particles and also in the estimation of γ'_c. However, it is quite evident that, at lower energies, nearly all particles scattered are without charge. It is these neutral particles which, by producing electron emission from the collector, gave the high values for the total apparent scattering coefficient, R, reported in Chapter II.

As an example, consider the case of a H_3^+ beam bombarding a Pt target at an energy of about 3.5 keV. Then from Figure 4.15, we see that the positive

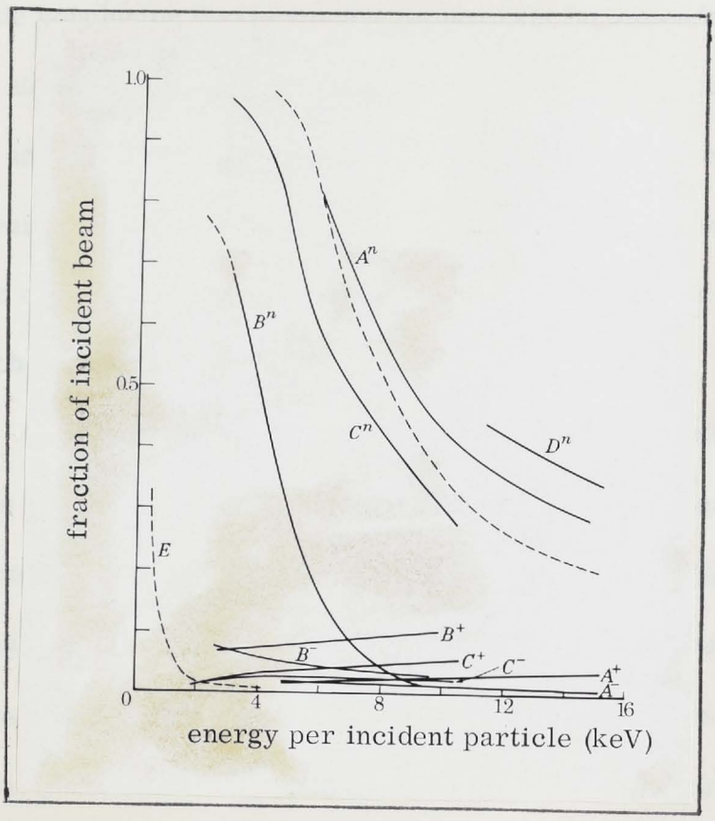

Figure 4.16

Total scattering of hydrogen particles with positive charge, negative charge and as neutral atoms, assuming Coulomb scattering:

A^+, A^-, A^n, H^+ ions on Pt, scattered as positive ions, negative ions and neutral atoms.

The dashed curves is that derived on the assumption of isotropic scattering.

B^+, B^-, B^n, H^+ ions on Ni, scattered as positive ions, negative ions, and neutral atoms.

D^n, scattering of N^+ ions on Pt as neutral atoms.

E, scattering of Cs^+ ions on W as positive ions after Brunée[38].

C^+ C^- C^n H_3^+ ions on Pt.

and negative scattering coefficients ρ_+ and ρ_- are approximately the same under these conditions. Also from Figures 2.25 and 2.32, Chapter II, we have γ'_c and R equal to 0.90 and 0.95 respectively (approximate values obtained by extrapolation of presented data). Thus, substituting into equation (4.4) gives:

$$\rho_n = \frac{0.95 - 0.90(0.025 + 0.025)}{0.90} \simeq 100\% .$$

Of course, the proportion of incident ions scattered as neutrals is actually less than this and perhaps is as small as 50%. Yet one cannot dispute

the basic conclusion that scattering as neutrals far exceeds scattering with charge at low energies. The rapid increase in the scattering of hydrogen, helium and nitrogen ions as neutral atoms at lower energies, is similar to the behaviour observed when protons are passed through various gases. The fraction of H^o in the emerging flux approaches unity as the beam energy approaches zero[35].

In Chapter II, section 2-2 C, we saw that the coefficient ρ_m probably remains fairly constant for velocities up to about 4×10^7 cm/sec, corresponding to an energy of about 1 keV for incident protons. Also, Figure 4.15 would seem to indicate an extrapolated value for ionic scattering of about 1 keV. This suggests that for incident energies from quite small values up to about 1 keV, very nearly all scattered particles are neutral. More direct and systematic work on the scattering of low energy ions is clearly called for, to settle these matters.

In Chapter I, we discussed the theory of McCracken and Freeman for the back-scattering of protons and deuterons from metals in the 10 - 30 keV energy region. They approximated the screened coulomb scattering, representing the physical process, by Rutherford scattering and thus obtained, for the number of back-scattered particles:

$$N_{TE} = - 1.42 f(z) I(\theta) E_o^{- 3/2} , \qquad (1.43)$$

where the various quantities were defined in Chapter I. For a Pt target, the screening is not negligible, due to the high Z_2 value, and the energies under consideration here are well below the values for (1.43) to be accurate, but nevertheless, equation (1.43) is in good qualitative agreement with the predictions of the experimental data. Figure 4.17 plots N_{TE} against the incident proton energy, taking $\frac{E}{E_o} = 0.1$ in Figure 1.3 a, for both Pt and Ni targets.

The trends are clearly the same as for Figure 4.16, and confirm the marked increase in scattering at low energies. A more detailed theoretical

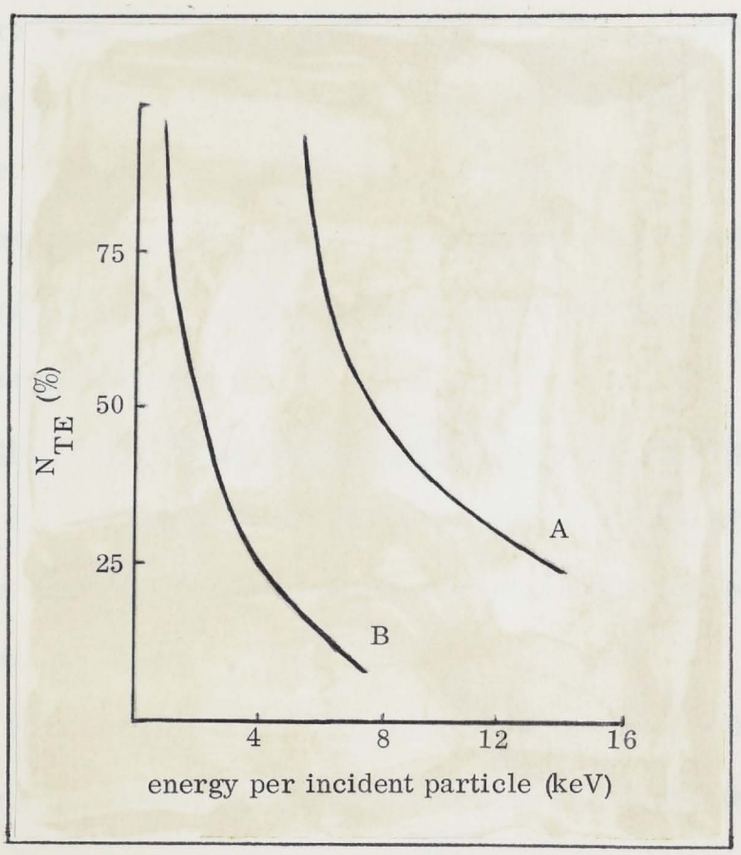

Figure 4.17

N_{TE} (%) as a function of incident beam energy
for protons upon Pt (curve A) and Ni (curve B) targets,
taking $\frac{E}{E_o} = 0.1$,
and assuming Rutherford back-scattering.

discussion was presented in Chapter I, where it was shown that a knowledge of the capture and loss cross sections in the solid is necessary to estimate the numbers of back-scattered protons (or H^- ions) alone.

For 5 keV H^+ on Pt, we see, from Figure 4.15, that $\rho_+ \sim \rho_-$ and so (4.4) becomes:

$$\rho_m = \frac{R - \gamma'_c(\rho_+ + \rho_-)}{\gamma'_c} \qquad (4.5)$$

or, as $\rho_+ + \rho_- + \rho_m = 1$,

$$R = \gamma'_c \, . \qquad (4.6)$$

Now, from Chapter II, Figure 2.32, we can obtain the value of R as 0.48 and so $\gamma'_c = 0.48$. From Figure 2.25, Chapter II, we find that for a

secondary electron emission coefficient of 0.48, the equivalent incident particle energy is 3.5 keV. Thus the "average energy" of the scattered particles from the target is roughly 3.5 keV, or 70% of the incident energy. As most of these are neutrals, we conclude that the energy spectra of scattered neutrals are much broader than for particles scattered with positive charge, confirming the conclusions reached above.

4-3 Spectra of Heavy Ions: Experimental Results and Discussion

A great number of energy spectra was taken for heavy ions and they require a somewhat different explanation from the light ion spectra discussed in the previous section.

Referring to Table 1.1, Chapter I, we see that $\sim$ 10 keV nitrogen and argon ions lose most of their energy in nuclear collisions with lattice atoms, due to their much lower velocities relative to protons or deuterons at the same energy. (The inelastic loss cross section increases linearly with velocity according to the Lindhard theory.)

A. Results

(i) Nitrogen ions

Figure 4.18 B shows positive spectra obtained at 90 ± 3.7^{o} for N^{+} and N_2^{+} ions bombarding molybdenum, nickel and platinum targets, with energies in the 10 - 15 keV range.

All the spectra in Figure 4.18 B show a peak very close to the value predicted from equation (1.25) for elastic scattering. The spectra for nickel and molybdenum ions also show a peak at about 5 - 10% of the incident beam energy, although this was absent from the platinum spectra. Indeed, for a Pt target, there was no detectable current of scattered ions with energies less than about half the incident beam energy. (A similar observation made for the spectrum of helium ions, scattered from a Pt target, was shown in Figure 4.13).

As in the case of light ions, the scattering from Pt in Figure 4.18 B

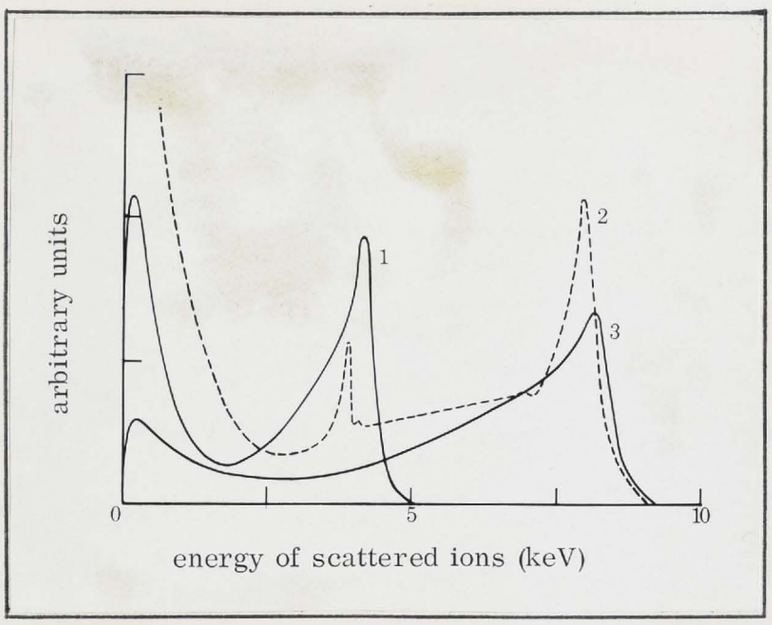

Figure 4.18 A

Energy spectra of positively charged scattered particles at 90^{o} to beam direction:

(1) N_2^+ on Mo at 11.2 keV; (2) Spectrum due to Panin[34];

(3) N^+ on Mo at 11.2 keV.

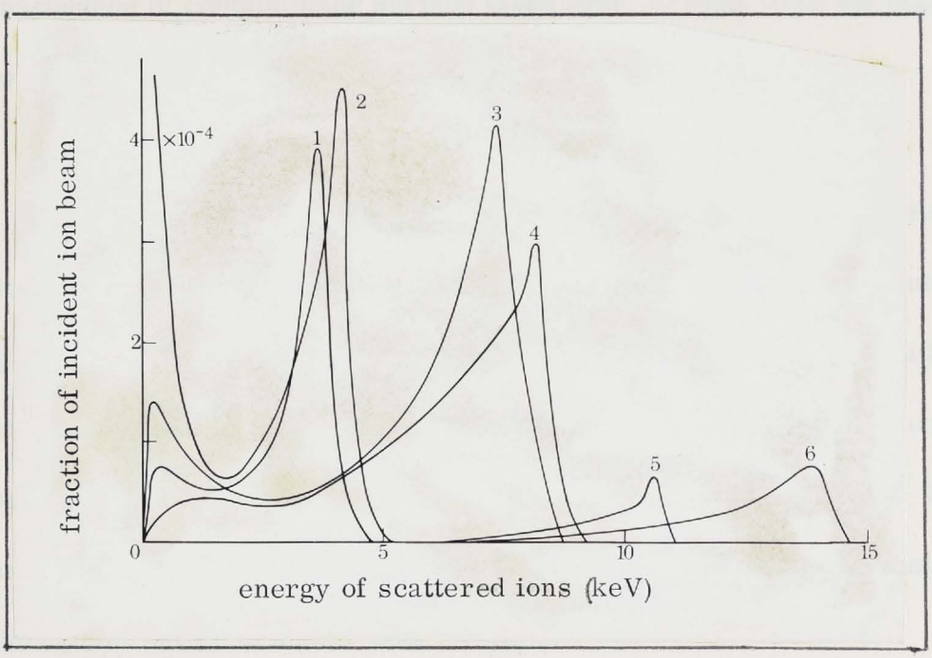

Figure 4.18 B

Energy spectra of positively charged particles scattered at 90 ± 3.7^{o} from various outgassed targets bombarded by nitrogen ions:

(1) N_2^+ ions on Ni at 11.6 keV; (2) N_2^+ ions on Mo at 11.2 keV;

(3) N^+ ions at 11.6 keV; (4) N^+ ions on Mo at 11.2 keV;

(5) N^+ ions on Pt at 11.6 keV; (6) N^+ ions on Pt at 15.1 keV.

is much less than from Ni or Mo, although the results for the total apparent scattering indicate that the total scattering over all angles and charge states is considerably greater for Pt, as expected for Rutherford scattering.

No scattering of ions with negative charge could be detected for incident N^+ and N_2^+ ions upon any of the targets employed in this work.

Figure 4.18 A compares present results with nitrogen ions, with those of Panin[34]. Panin's spectrum for N_2^+ at 22 keV has nearly the same values of E_{max} and E_{peak} as the present spectrum obtained for N^+ at 11.2 keV, as expected if the molecular ion dissociates upon striking the surface into components of equal energy. However, Panin's spectrum contains a peak at half the energy of the elastic peak, due to N^+ ions, which he attributed to N^{++} ions. He also observed a much higher proportion of low energy ions and a sharp increase in their numbers at low energies. It is probable that both these features were a consequence of contaminated surface conditions, arising from the high background pressures (about $1 - 3 \times 10^{-7}$ mm of Hg) in his apparatus.

(ii) Carbon and Oxygen ions

Results for these ions are illustrated in Figure 4.19. We see that O^+ and O_2^+ ions scattered with charge are predominantly negative because of the high electron affinity of oxygen. Only a couple of per cent of oxygen ions scattered with charge carry a positive charge for the case of a Pt target, while for a Mo target, the percentage is about 25%. The proportion of C^+ ions, scattered as negatives, also exceeds the proportion scattered as positives, although the latter is higher than for oxygen ions.

The negative scattering from Pt is greater than for Mo, whereas the positive scattering, as in the case of other ions, is less. This again suggests that the total scattering (over all charge states) is greater for Pt, despite the smaller value of the positive scattering. Also, from Figure 4.19, we see that there are considerable numbers of negative particles scattered from Pt with energies below half the incident beam energies, suggesting that the energy

spectra for neutral particles is considerably broader than the positive spectra and extends down to near zero energies.

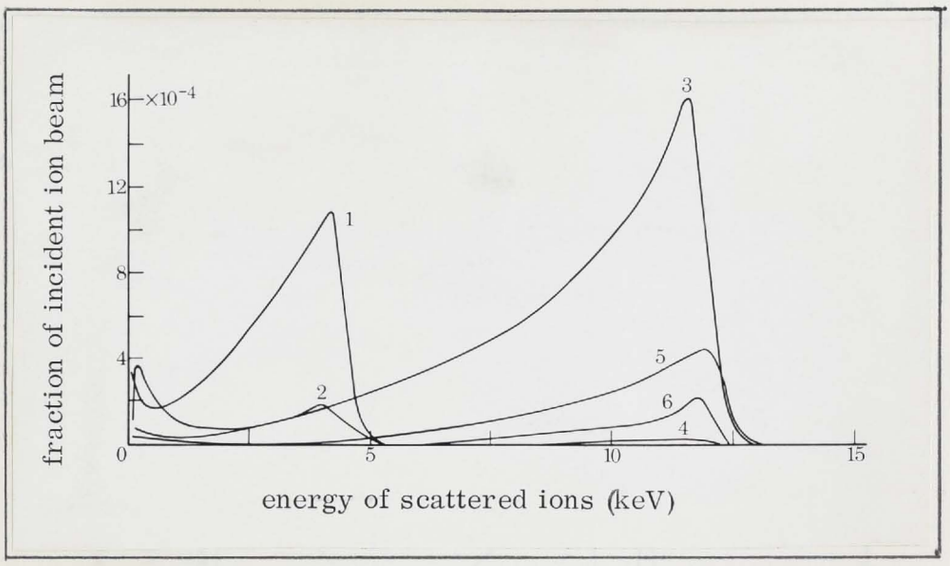

Figure 4.19

Energy spectra of particles scattered at 90 ± 3.7^{o} from molybdenum and platinum targets bombarded by oxygen and carbon ions:

(1) negative emission, O_2^+ on Mo at 11.2 keV;

(2) positive emission, O_2^+ on Mo at 11.2 keV;

(3) negative emission, O^+ on Pt at 13.7 keV;

(4) positive emission, O^+ on Pt at 13.7 keV;

(5) negative emission, C^+ on Pt at 13.7 keV;

(6) positive emission, C^+ on Pt at 13.7 keV.

None of the negative spectra in Figure 4.19 shows any indication of a low energy peak, nor is one evident for the positive ion spectra from a Pt target. The positive spectrum for O_2^+ ions upon a Mo target, however, does show a low energy peak at about 500 eV scattered ion energy.

Spectra obtained for CO_2^+ ions are not shown. However, this ion gave spectra of negatively charged scattered ions with a single peak due to O^- (as can be shown if one assumes that the incident molecular ion energy is shared between the dissociation products in proportion to their masses) and no appreciable positive ion spectra.

(iii) Neon ions

Figure 4.20 shows the energy spectra of particles scattered with positive charge from Mo and Pt targets under bombardment by Ne^+ ions. As in the case of other noble gas incident ions, no negative ion spectra were detectable, due to the high ionization potential of the noble gas atoms.

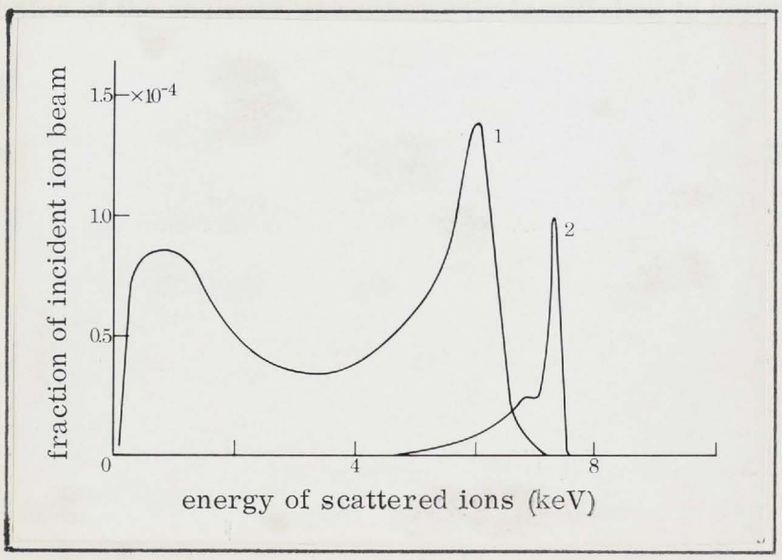

Figure 4.20

Energy spectra of positively charged particles scattered at 90 ± 3.7° from molybdenum and platinum targets bombarded by neon ions:

(1) Ne^+ ions on Mo at 9.2 keV;

(2) Ne^+ ions on Pt at 9.0 keV.

The spectra show the elastic peaks and, as for the previous spectra, there are no ions scattered from a Pt target with energies less than about half the incident beam energy. On the other hand, there is again a low energy peak in the spectrum for ions scattered from a Mo target, at about 10% of the incident beam energy.

The scattering with positive charge is much less for Pt than for the Mo target, as observed for other ions.

(iv) Argon ions

Figure 4.21 A shows the spectra of positive particles scattered from Mo, Ni and Pt targets. The general features are the same as for neon and nitrogen, apart from the high energy hump on the spectrum for A^+ ions upon Mo. The reason for the latter will be discussed below (section 4-3 B (v)).

For the case of A^+ ions incident upon a Ni target, the calculated position of the elastic peak is quite low, only about 19% of the incident beam energy, and so the spectrum shown in Figure 4.21 A for A^+ ions upon Ni is probably a fusion of a low energy peak, similar to that observed in the spectrum for a Mo target at about 10% of the incident beam energy, with the elastic peak. The resolution of the analyser was apparently insufficient to separate these, but the high energy scattered particles (with energies up to about 50% of the incident beam energy) are probably associated with the low energy peak rather than with the elastically scattered particles.

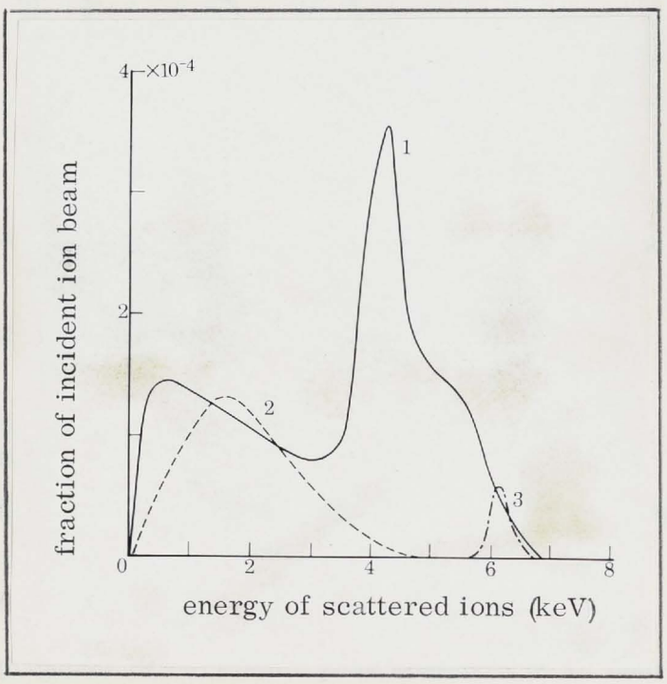

Figure 4.21 A

Energy spectra of positively charged particles scattered at 90 ± 3.7° from various targets bombarded by argon ions:

(1) A^+ ions on Mo at 9.2 keV;

(2) A^+ ions on Ni at 9.1 keV;

(3) A^+ ions on Pt at 9.0 keV.

Figure 4.21 B compares present results with argon ions with those of Panin[34]. As in the case of nitrogen ions, Panin found a peak at half the energy of the elastic peak, which he attributed to doubly charged ion, A^{++}, elastically scattered from the target. Also, as in the case of nitrogen ions,

he observed a sharp increase in scattering with positive charge at low energies. Detailed examination of the spectrum obtained in the present work (indicated by the dots) failed to find any trace of a peak at half the energy of the elastically scattered A^+ peak.

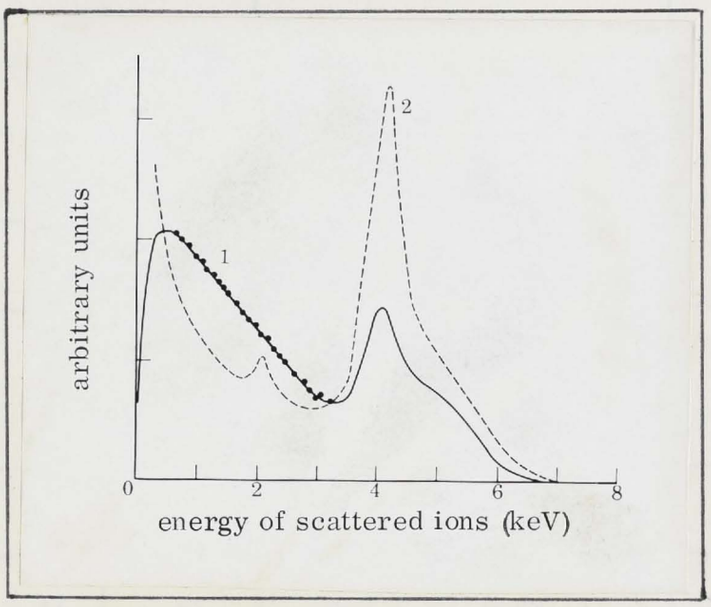

Figure 4.21 B

Energy spectra of positively charged particles scattered at 90^o to beam direction:

(1) Ar^+ on Mo at 9.2 keV, target bright yellow heat. Experimental points are shown over part of spectrum.

(2) Ar^+ on Mo at 10.0 keV, target red hot, according to Panin[34].

B. Discussion

(i) The presence of the elastic peak observed in all heavy ion spectra is easily explained in terms of hard sphere classical 2-body collisions. These are described by equations (1.25) and (1.26), Chapter I. Table 4.1 shows that, for heavy ions, the observed elastic peak always occurs at or very close to the calculated value of $\frac{M - m}{M + m}$ for scattering at right angles. (M and m are the masses of the target and incident particles respectively). Data for light ions are also included in the table for completeness, and it is noteworthy that the peaks for these ions, although broader, occur approximately at the values expected for ions scattered elastically without inelastic energy loss.

(ii) The positive spectra for scattering of heavy ions from Pt are all very simple, consisting only of ions with energies at or close to the elastic peak. A remarkable feature of all the positive spectra of ions scattered from Pt, is the complete absence of ions with energies less than about half of the incident

TABLE 4.1

ION		TARGET		ENERGY AT PEAK OF DISTRIBUTION AS FRACTION OF BEAM ENERGY, W	ENERGY FOR ATOMIC SCATTERING AT 90° $\frac{M-m}{M+m}$ W
Species	Mass m	Material	Mass M		
H^+	1	Mo	96	0.90	0.98
H^+	1	Ni	59	0.81 *	0.97
H^+	1	Pt	195	0.93 *	0.99
D^+	2	Pt	195	0.95	0.98
He^+	4	Mo	96	0.83	0.92
He^+	4	Pt	195	0.95	0.96
C^+	12	Pt	195	0.86	0.89
N^+	14	Ni	59	0.63	0.62
N^+	14	Mo	96	0.73	0.75
N^+	14	Pt	195	0.92	0.87
O^+	16	Pt	195	0.85	0.85
Ne^+	20	Mo	96	0.66	0.66
Ne^+	20	Pt	195	0.81	0.81
Ar^+	40	Ni	59	0.18	0.19
Ar^+	40	Mo	96	0.45	0.41
Ar^+	40	Pt	195	0.69	0.66

* Average for six observations

beam energy. Even the negative ion spectra, Figure 4.19, consist predominantly of ions with energies near the value for single elastic collisions, although there are also considerable numbers of low energy ions in these spectra.

A heavy ion of several keV will have considerably lower velocity than protons and deuterons at the same energy. Thus a heavy ion quickly becomes

neutralized upon entering the lattice of the metal. For a Pt target, at least, all scattered ions observed must have originated from elastic events very close to the surface, i.e., ions which have been back-scattered before they are neutralized by the electrons of the metal. Any low energy incident particles emerging from the metal lattice would have traversed relatively longer paths in the latter and would thus be in the neutral or negative charge states, i.e., have had time to pick up one or two electrons from the metal. For incident noble gas particles, of course, only one electron will be picked up, as they do not form stable negative ions. We thus have a fairly straight forward explanation for the absence of low energy particles in the positive ion spectra from a Pt target. The spectra for A^+ and Ne^+ are particularly sharp, due to the high ionization potentials of their atoms.

Clearly, in view of our discussion above, and in Chapter I, the energy spectra of neutral atoms, for all incident ion species, would be much broader and more intense than the spectra for particles scattered with positive charge, from close to the metal surface. A more detailed discussion has been given in Chapter I, as part of an overall theoretical investigation of ion surface interaction phenomena.

For the case of light ions, we saw in the previous section, that most particles scattered at low incident energies (of a few keV or less) are in the neutral state. In other words, the incident particles have spent sufficient time within the target to become neutralized and very few will emerge with either positive or negative charge. We are not surprised, therefore, to deduce from our heavy ion data that most scattered particles are also neutral. In Figure 4.16 the trends for nitrogen ion scattering are seen to be approximately the same as for lighter ions, i.e., there is a marked increase in ρ_m as the incident ion beam energy is reduced. Our discussion in Chapter II, section 2-2 C, indicated that the proportion of neutrals scattered probably remains high for incident beam energies up to several keV for nitrogen and up to energies as high as 40 keV for argon.

(iii) The most difficult feature of the heavy ion spectra to explain satisfactorily is the presence of the low energy peak in the spectra of ions scattered with positive charge from Mo and Ni targets. Any proposed explanation must explain the following facts, observed under the conditions of the present experiments:

(a) The absence of the peak from the spectra of light ions, e.g., from hydrogen, deuterium and helium spectra.

(b) The absence of the peak from all spectra taken from a Pt target.

(c) The absence of the peak from the spectra of particles scattered with negative charge.

(d) The increase of the low energy peak relative to the elastic peak, as the temperature of the target is increased.

(e) The occurrence of the peak at about 10% of the incident beam energy.

Property (d) is shown in Figure 4.22. There is quite a pronounced change in the relative heights of the low energy and elastic peaks with target temperature and also, it may be implied from spectra (3), (4) and (5) for N^+ ions on Mo with the surface conditions of the target.

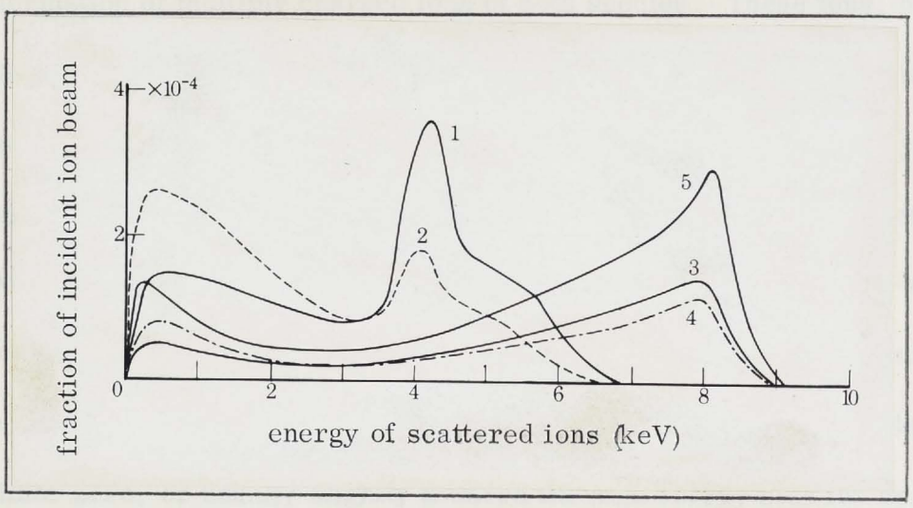

Figure 4.22

Effect of heating upon the energy spectra of positively charged particles scattered at 90 ± 3.7^{o} from a molybdenum target bombarded by argon and nitrogen ions:

(1) Ar^+ ions at 9.2 keV, Mo target heating current 8 amps, dull red heat;

(2) Ar^+ ions at 9.2 keV, Mo target heating current 16 amps, white hot;

(3) N^+ ions at 11.2 keV, Mo target heating current 8 amps, dull red heat;

(4) N^+ ions at 11.2 keV, Mo target heating current 16 amps, white hot;

(5) N^+ ions at 11.2 keV, Mo target heating current reduced to 8 amps for 2 hours.

While the low energy peak has been observed by several researchers, there is still no satisfactory explanation of it. The contention of Smith[36] and Panin[34] that it consists of sputtered metal ions, requires more substantiation than is provided by these workers.

In the following discussion several hypotheses are advanced which could provide possible explanations for the low energy peak. The origin of the peak can only be definitely settled by further experiments, preferably employing momentum as well as energy analysis of the ion spectra under heavy particle bombardment.

In our discussion in Chapter I, we saw that the collision of a heavy ion (or atom) with a heavy atom at intermediate energies, involves a considerable degree of interpenetration of the electron atmospheres. The relative motion of the nuclei will supply energy for auto-ionization of the outer electrons of the quasi-molecule thus formed and this may result, as shown by Russek[15], in the formation of multiply charged ions of both species. These ions, being multiply charged, would appear in the ion spectra with an apparent energy below half that of elastically scattered ions, as the electrostatic analyser will focus all particles with the same energy to charge ratio onto the collector at a given focussing field. The loss of energy in the ionization process would, however, also shift the elastic peak towards lower energies by an amount $\overline{Q}$ (see Chapter I), whereas the above table shows that the shift of the elastic peak is either zero, or usually slightly towards the high energy side for heavy incident ions.

Also, the spectra presented in the present report show no peaks corresponding to particles scattered with double or triple charge, althought these were observed by Panin, who worked with contaminated surfaces (apparently). This is an important argument against attributing the low energy peak to multiply charged ions.

It is difficult to explain the apparently COMPLETE absence of any low

energy peak for spectra taken from a Pt target in the current work, in view of its presence for other targets. It is interesting that a low energy peak was observed for another Pt target employed in another program of experiments, which will be briefly referred to in the appendix. The only difference in the relevant experimental conditions was that the latter target was indirectly heated to a bright red heat and the actual experiments were performed on the target at room temperature, whereas all present observations with Pt were made on a red hot target. It seems, therefore, that the low energy peak is somehow correlated with the condition of the target surface - especially its temperature - during experimentation. In the case of the present observations, the target temperature was quite high and thus, upon the basis of the variations observed in Figure 4.22, the low energy peak should be considerably more pronounced than for a cold surface. Instead, the reverse is the case, and no peak at all is observed in the present work.

We will now discuss the suggestion that the low energy peak is composed of sputtered target ions. Platinum ions, being considerably heavier than molybdenum and nickel ions would have a greater probability of being neutralized at the target surface and so fewer platinum ions would occur in the spectra from this metal. In addition to the greater probability of neutralization for platinum ions at low energies, it is possible that the interpenetration of the electron shells is much smaller than for Mo and Ni, by virtue of the higher Z_2 value for Pt. The smaller interpenetration would further reduce the relative intensity of the low energy peak, as the probability of auto-ionization is decreased. On the other hand, we have noted that auto-ionization cannot be a very prominent process at the beam energies under consideration, as there is a complete absence of doubly or triply charged ions in the spectra.

The results presented in Chapter II must also be considered while discussing the possible origins of the low energy peak. Our results there clearly indicated that the main contributions to the total apparent scattering

coefficient came from back scattering (approximately Rutherford or screened Coulomb in form) of incident particles and tertiary emission from the collector caused by these back-scattered particles. The coefficient "R" certainly does NOT come from sputtering of target ions, as proposed by Van Wijngaarden et al.[30] It is possible that some sputtering of target particles as ions does occur for the heavier incident ions, but their current to the collector must be quite small compared to the current of back-scattered ions. The R(E) functions for ALL target ion combinations follow the same general trends with the velocity of the incident ion and not the incident ion mass being the principal factor determining R(E) for a given target. Again, this does not support the sputtering hypothesis.

It must also be pointed out that the energy of the peak in question is always close to 10% of the incident particle energy and this is well above what would be expected from any current sputtering theory - Thompson[33].

The writer and his fellow researchers have suggested a possible mechanism contributing to the low energy peak[37], although it is highly doubtful that it provides the complete explanation. A scattered primary particle may eject a charged metal ion from the surface by a second collision with the target atoms. Consider, for example, the case of A^+ ions incident upon a Mo target with an energy of about 10 keV. The A^+ ions will be scattered from a Mo atom with mean energies of about 4 - 5 keV and there will be an appreciable probability of the scattered A^+ ions making a collision with another Mo atom before escaping from the metal. (The fact that such multiple collisions occur for Mo and Ni targets will be discussed in more detail in the following sub-section). These Mo atoms, some charged, will be ejected in the 90^o direction (relative to the incident beam) with mean energies of about 1 keV, which corresponds with the position of the low energy peak. It should be pointed out that this process is not the same as direct sputtering which, we noted above, is a rather improbable explanation of the low energy peak. Directly sputtered target

particles have such low mean velocities that very few would emerge in the charged state (see section 1-3, Chapter I, for a fuller discussion). If we call the process outlined above "secondary sputtering" for convenience, we see that its magnitude is closely correlated with the amount of back-scattering, and so it is not incompatible with the conclusions reached in Chapter II.

For light incident ions the mass ratio $\mu \gg 1$ and "secondary sputtering" is effectively absent, because of the very small amount of energy transferred to the target - property (a) above. The property (b) - no low energy peak for a Pt target - could be a combination of both the higher energies of the scattered A^+ ions (which reduces the probability of a second close collision with a metal atom on the way out of the target) and the lower mean energies of the "secondary sputtered" Pt ions (which would have greater probability of being neutralized on its way out of the target). Property (c) follows from the inability of metals to form stable metal ions, and could be due to the increased probability of a sputtered metal ion escaping with its charge from a higher temperature target, owing to decreased probability of capturing one of the more energetic electrons on its way out of the target. Property (e), of course, follows from the hypothesis itself.

The above hypothesis thus provides an explanation for the origin of the low energy peak, but it is by no means the only possibility, and an alternative hypothesis is that the low energy peak does, in fact, consist principally of the incident ion species and not of target ions. While the writer feels that this is very probable, he is unable to propose a detailed mechanism which could explain the presence of such a clearly defined group of low energy scattered ions of the incident species. In our discussion in section 1-2, Chapter I, we saw that a particle travelling through the metal lattice will oscillate between the various possible charge states. For elastically scattered particles, comprising the elastic peak observed in all heavy ion spectra, the incident ion does not penetrate far enough into the metal to lose its charge, i.e., to become neutralized.

However, we saw that most back-scattered particles do, in fact, penetrate a finite distance into the metal and thus become neutralized prior to emerging from the metal. At sufficiently low velocities, some of the back-scattered neutrals, especially if they are in metastable states, may lose their captured electron and so emerge in the charged state, giving rise to the low energy peak. The de-excitation process possibly occurs at the surface or in close proximity to it, by an Auger type process (see section 1-4, Chapter I). The great majority of scattered particles will, of course, emerge as neutrals at low energies.

Observations employing mass analysis of the positive ion spectra will undoubtedly settle the problem of the origin of the low energy peak, in the near future.

(iv) The rapid increase in scattering of ions as neutrals at lower incident ion energies (Figure 4.16) is probably a general feature of ion scattering when the ionization potential of the bombarding atom species exceeds the work function of the target surface. Then the neutrals have little probability of losing an electron at the surface, although we saw in (iii) that the possibility of a small number (enought to account for the low energy peak in the positive ion spectra) doing so cannot be ruled out. In the case of scattering of alkali ions from metal surfaces, with work function greater than the ionization potential, the proportion of scattered IONS increases rapidly to values of the order unity. e.g., curve 'E' in Figure 4.16 was obtained by Brunée for the scattering of Cs^+ ions on W as positive ions[38]. At very low bombarding energies, of about 40 eV, Veksler[39] found a maximum in the scattering of alkali ions of about 0.9 to 0.95, followed by a rapid decrease as the energy was reduced further. This suggests that a maximum may occur in the ρ_m curves in Figure 4.16, at energies lower than attained in the present observations

(v) In Table 4.2 the values of E_{max}, the maximum energies of the scattered ions from Mo and Ni targets, E_{calc}, the calculated values of the scattered ion

energy for elastic scattering, and E_{peak}, the observed values of the energies at the peaks of the distributions are tabulated. While the values of E_{peak} and E_{calc} are in reasonable agreement, E_{max} is considerably higher in all cases. The higher energy particles (those with energies exceeding E_{peak}) are those which have undergone multiple scattering through two, three, or more collisions. While for each individual scattering event the scattering angle, θ_i, is less than 90^o, their sum is 90^o. i.e:

$$\sum_{i}^{n} \theta_i = 90^o , \qquad (4.7)$$

where n is the total number of collisions undergone by the scattered particle. Snoek and Kistemaker[17 a] pointed out that the incident ion can lose less energy through a sequence of elastic collisions satisfying equation (4.5), than by a single collision through 90^o.

The high energy hump on the spectrum for A^+ scattered from Mo occurs at 9.2 keV (Figure 4.21) and is probably due to ions which have been scattered twice. (In (iii) the possibility of double collisions explaining the low energy peak in the positive ion spectra for heavy ions from Mo and Ni targets, was discussed). The centre of the hump occurs at about 0.6 of the incident beam energy, whereas calculation shows that, for two scattering events with scattering angles 45^o each, the scattered ion energy will be about 0.7 of the incident beam energy. Such a two-scattering hypothesis for explaining the high energy hump is quite feasible.

Alternatively, the hump could result from the incident A^+ ion interacting simultaneously with more than one target atom. At very low ion energies the bi-particle collision picture may require revision, or at least the possibility of collisions involving more than two particles simultaneously cannot be as lightly dismissed as many researchers in this field believe. In the present case, the effective mass of the scattering centre would be 240 a.m.u., or 2.5 Mo atoms.

TABLE 4.2

Ion	Energy	Target	E_{peak} (keV)	E_{max} (keV)	E_{calc} (keV)	$\frac{E_{max}}{E_{calc}}$
Ar^+	9.1	Ni	1.65	5.0	1.75	2.85
Ar^+	9.2	Mo	4.2	7.0	3.77	1.86
Ne^+	9.2	Mo	6.05	7.2	6.07	1.19
N^+	11.6	Ni	7.35	8.7	7.15	1.22
$*N_2^+$	11.6	Ni	3.6	4.8	3.57	1.34

* N_2^+ is assumed to be equivalent to $2N^+$ at half energy.

APPENDIX I

ASPECTS OF THE APPARATUS

A. Beam Generation and Focussing

The experimental apparatus is illustrated in Figure A.1 and details of the radio-frequency ion source are shown in Figure A.2. As this is a scientific, rather than a technical report, our discussion will be generally limited to factors which have direct bearing upon the measurement or interpretation of the scientific data.

The working gas was admitted to the source by a Granville-Phillips valve which gave a regular and reproducible gas flow. The discharge was viewed through a direct vision spectroscope, as a purity test, before measurements were performed with extracted ion beams. Whenever the working gas was changed, it was necessary to flush the source and acceleration sections out with the new gas, usually to a few hundred microns. The source operated satisfactorily for about 1,500 hours with light gases before corrosive sputtering of the extraction canal began to affect the extracted ion currents. With argon and other heavy working gases, the operating time of the source was much reduced.

The theory of operation of r.f. ion sources has been extensively covered in the literature[40]. The source used for the present observations was of conventional design, employing inductive coupling. The discharge space proper, contained a minimum of metal to minimize positive ion recombination (thus the silica disc and the pinch in the source walls). No attempt was made to incorporate steady transverse or longitudinal magnetic fields into the source design. The operating pressure in the source was estimated to be about 20 - 25 microns and provided ample ion beam currents for the purposes of the present work. For example, with hydrogen as the working gas, focussed beams of H^+, H_2^+ and H_3^+ of $\sim 2 \times 10^{-7}$ amp, 5×10^{-8} amp and 2×10^{-8} amp respectively, were readily obtained for 10 - 50 keV energies.

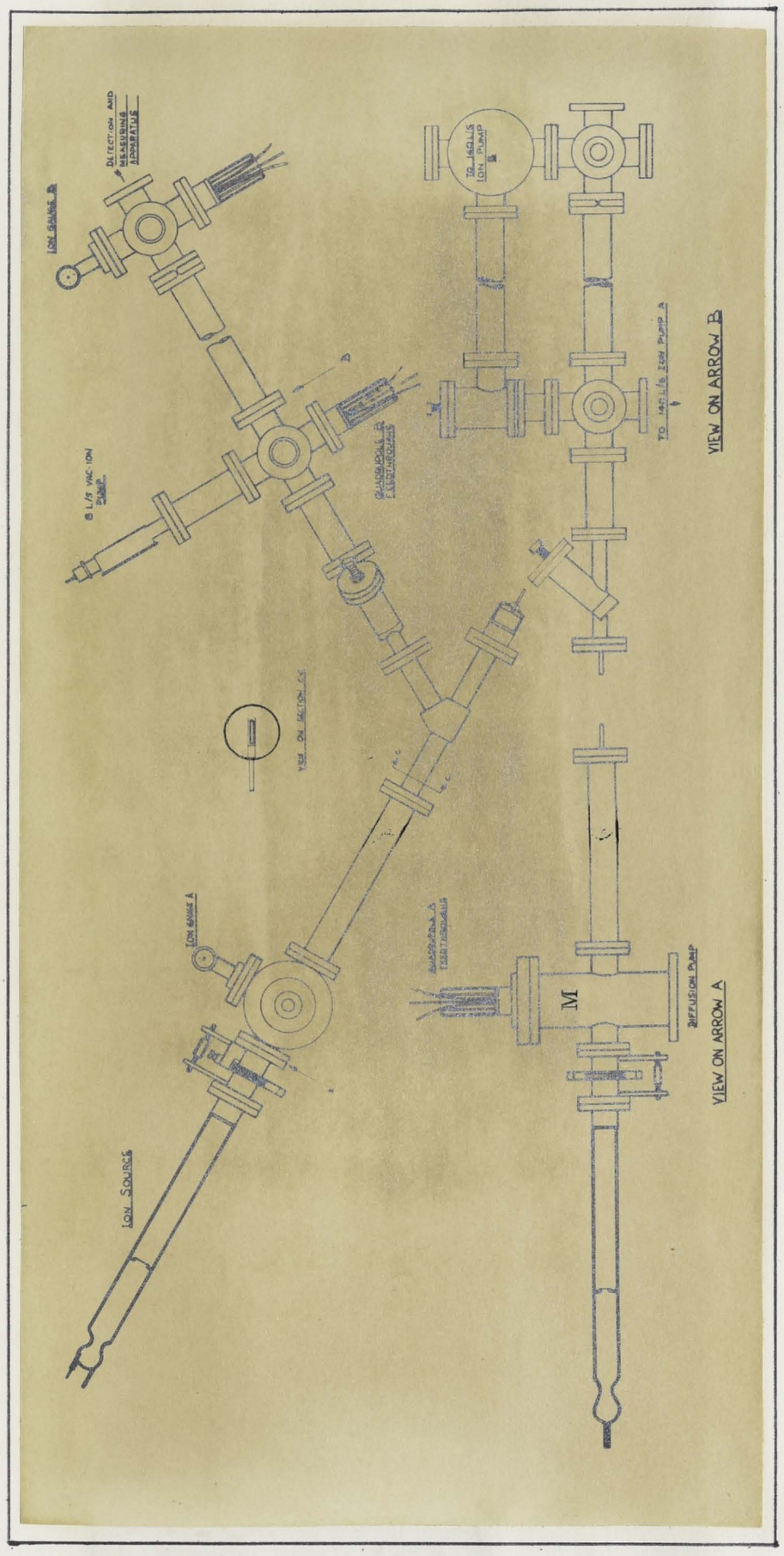

Figure A.1

Vacuum system showing principal components.

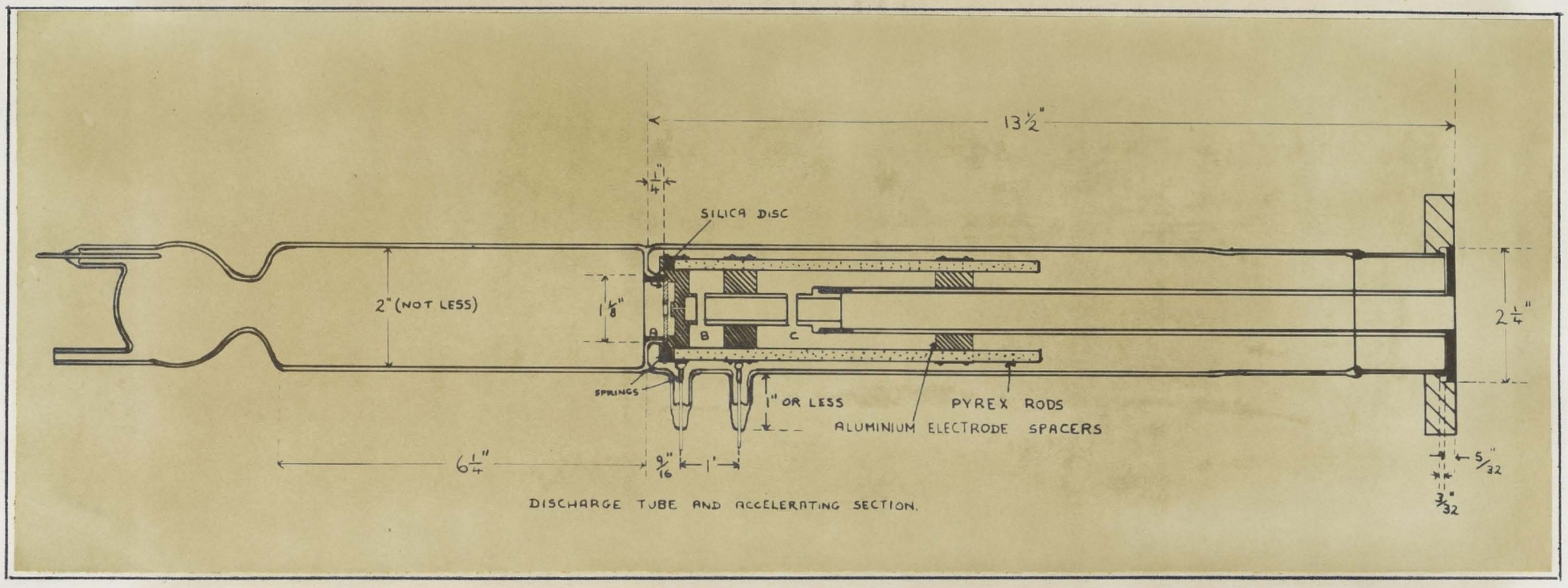

Figure A.2

Details of R-F ion source.

The length of the extraction canal relative to its diameter, was somewhat higher than for optimum current extraction[41]. However, this was offset by the smaller gas consumption and equilibrium pressures in the system. Even so, the pressure in the manifold chamber, M, was still quite high, exceeding 10^{-5} torr. The estimated working gas consumption for hydrogen was about 14 cc/hour at atmospheric pressure, under operating conditions. Positive ions extracted from the discharge tube were focussed and then accelerated using cylindrical co-axial electrodes. The joint acceleration discharge sections were joined to the rest of the system via a flexible bellows arrangement, to facilitate accurate beam (or electrode) alignment.

The electrical layout for the operation of the ion source and the ion optical elements is shown in Figure A.3. The various power supplies, spark suppressor units and by-pass capacitances, etc., are shown in the diagram, which is largely self-explanatory. The maximum voltage employed was 60 kV, this being determined by the gap widths and insulation-to-earth of the various sections of the high voltage apparatus. The 100 megohm resistance chain, R, prevented electrical breakdowns across the acceleration gap, and it was necessary to take into account the voltage drop across the chain, when calculating the ion beam energy. The latter was given by:

$$E_o = e(V_{ext} + V_{acc} - v)$$

$$= e(V_{ext} + V_{common}) , \qquad (A1)$$

where V_{ext} was the extraction voltage relative to "common", V_{acc} the acceleration voltage relative to ground, v the voltage drop across the resistance chain and V_{common} the voltage of "common" relative to ground. The extraction canal was at "common" as shown in Figure A.3.

The beam emerging from the canal was converged by the cylindrical lens arrangement to a point several centimetres past the accelerating gap (referring to Figure A.1). The beam emerging from the ion source assembly

was diverging by about 5^{o} maximum.

Most of the diverging beam leaving the ion source assembly, entered an electrostatic quadrupole placed a little past M, but before the bending magnet. Another identical quadrupole was placed at the appropriate position in the second arm of the system, past the bending magnet, to again focus the diverging beam, this time from the bending magnet, onto the target. The construction of the quadrupole is shown in Figure A.4, the electrical connections to them being shown in Figure A.3. The quadrupoles were triplets with provision for steering as well as focussing the ion beam. The detailed theory of quadrupoles has been given by Enge[42]. The triplet (three element) quadrupoles were chosen because of their strong focussing action over a wide range of image and object distances in both directions. While the $\frac{E_o}{V_q}$ ratio (V_q being the potential difference between any two diagonally opposite electrodes of the quadrupole) was quite low, about 130, this was no disadvantage for medium energy ion beams, e.g., for a 20 keV ion beam. V_q was about 150 volts. This is close to the value of 170 volts estimated from the tabulated data of Enge.

The focussing action of the quadrupoles was checked visually by quartz plates placed at the approximate focal points during system fabrication. The lenses gave a bright focus of about 1 mm diameter at the centre of the plates with a diffused penumbra of more irregular shape and several mm across surrounding the central focus. The area of beam bombardment of the target was about 1 mm^2 and with a typical beam current of 2×10^{-7} amps, this gave a beam intensity of about 20 microamps/cm^2.

The 60^{o} bending magnet was carefully calibrated before the commencement of systematic experimental work, to ensure accurate ion beam identification. The magnet was originally designed for light ion work and the maximum energy A^{+} ions which could be deflected onto the target was about 10 keV, a serious limitation for these heavier ions.

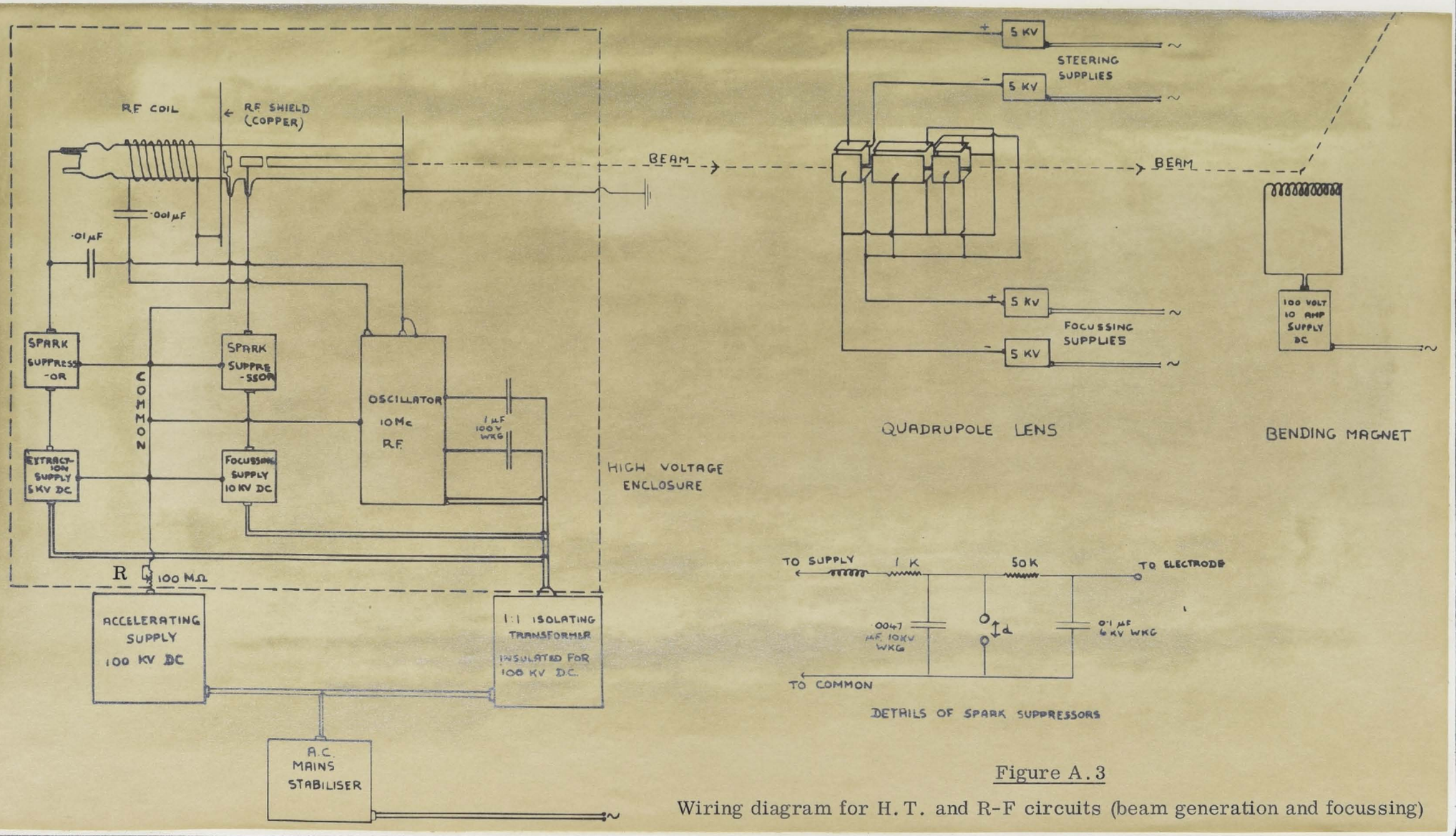

Figure A.3

Wiring diagram for H.T. and R-F circuits (beam generation and focussing)

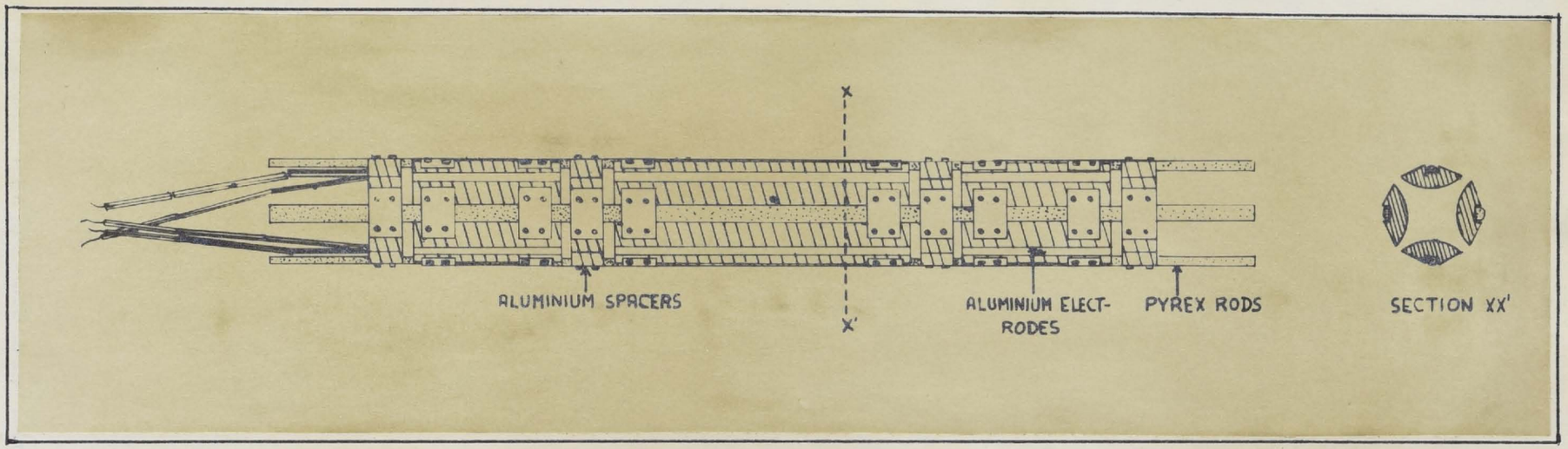

Figure A.4

Construction details of electrostatic quadrupoles.

B. The Vacuum System

The two most important features of the vacuum system were differential stage pumping and the use of ion pumps in the final two stages.

The several differential stages (see Figure A.1) were necessary in view of the relatively high operating pressure (about 20 microns) in the discharge tube and the necessity of keeping the pressure and contamination level in the detection chamber, as low as possible under working conditions.

The first differential pumping stage was that between the extraction canal of the source and the bending magnet, the latter constituting a sufficiently high impedance to be regarded as an "aperture" from a pumping stand point. This stage was pumped by a diffusion pump, suitably baffled and trapped, of speed 150 litres/sec.

Past the bending field were two further differential pumping stages, each pumped individually by a 140 litres/sec Varian ion pump. The final stage (detection chamber) was pumped down originally via the by-pass, rather than through the small $\frac{1}{8}$" hole in the direct beam path (see Figure A.1).

The table shows the ~~resid~~ equilibrium pressures in the various differential stages, and also in the backing line, both under residual and working conditions. All units are in torr.

	Backing Line	Manifold Stage	1st Ion Pumped Stage	2nd Ion Pumped Stage (Target Chamber)
NO Gas fed in	$2-3 \times 10^{-3}$	5×10^{-8}	2×10^{-8}	8×10^{-9}
~~No~~ gas fed in	$10-11 \times 10^{-3}$ (Pirani Gauge)	2×10^{-5} (Ionization Gauge)	8×10^{-8} (Ionization Gauge)	$1-2 \times 10^{-8}$ (Ionization Gauge

The relatively high pressure in the manifold differential pumping stage and the considerable length of this section (about 40") give charge-changing collisions an appreciable probability of occurring in this section. However,

the bending magnet sorts out the various charge states and subsequent charge-changing events are negligible.

To help ensure clean conditions in the detection chamber, the latter was baked, or outgassed, to temperatures of about 250 - 300^{o}C for several hours, prior to each experimental run. This precaution was necessary, as unsaturated hydrocarbons are readily adsorbed on metal surfaces at low pressures, and can appreciably affect the surface characteristics for both hot and cold surfaces. To obtain carefully controlled experimental conditions, it was necessary for the target to be free of all adsorbed foreign particles and the composition of the background gas to be known. The background gas consisted of both the residual gas and the material conveyed into the target chamber by the ion beam, under operating conditions.

Despite stringent precautions, it was found impossible to completely eliminate hydrocarbons from the target (detection) chamber. This was evidenced by mass spectra taken at regular intervals. The spectra shown in Figure A.5 are typical of the background gas in the isolated target chamber with:

(a) The target at a moderate red heat, with a background pressure of about 2×10^{-8} mm, subsequent to bombardment by several ion species, and

(b) The target flashed to a bright white heat at about 6×10^{-8} mm.

The background pressure in (a) consisted mainly of H_2, H_2O and N_2 with assorted hydrocarbons, e.g., peaks in the spectrum correspond to the radicals: C^+, CH_2^+, CH_3^+, CH_4^+, CH_5^+, $C_2H_2^+$, $C_2H_3^+$, $C_2H_4^+$ and $C_2H_5^+$. Oxygen was not present, probably because of the high pumping speed of the ion pump for this "active" gas. From spectrum (b) we see that the increase in pressure upon heating the target, arose mainly from the desorption of H_2O and N_2. However, CO_2, O_2 and HO^+ (possibly) and several hydrocarbons were also desorbed from the target, showing how the target can accumulate hydrocarbons, even at a red heat. Hydrogen and helium were not desorbed, despite previous bombardment by these ions. A small amount of neon, from previous Ne^+ bombardment was, however, present in

spectra (b). These spectra were taken using an A.E.I. quadrupole mass spectrometer, model 150 A.

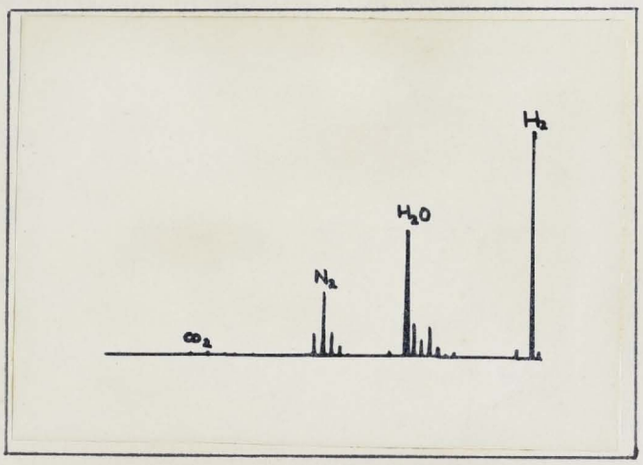

Figure A.5 (a)

Residual mass spectrum with target at red heat (pressure $\sim 2 \times 10^{-8}$ mm).

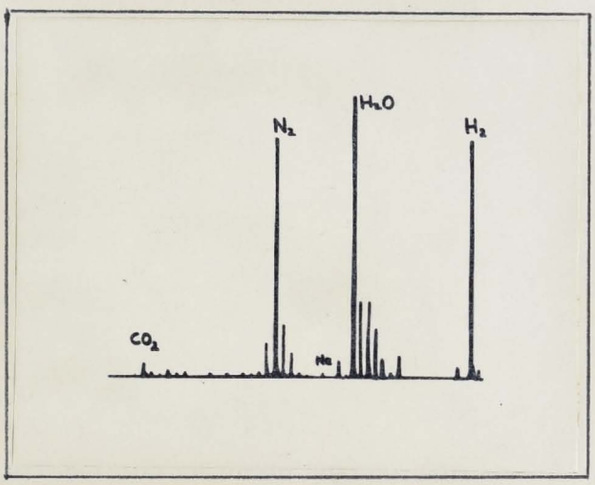

Figure A.5 (b)

Residual mass spectrum with target flashed to white heat (pressure $\sim 8 \times 10^{-8}$ mm).

The subject of surface cleanliness and its relationship to experimental data was discussed at some length both in Chapter II and Chapter IV. In these chapters, it was shown that a target can be deemed "clean" after it had been maintained at a red heat in a vacuum for several days and periodically flashed to a red heat. For such a surface the electron coefficient γ was independent of temperature and the energy spectra for ions and electrons were reproducible to within a few per cent, under given experimental conditions. In Chapter IV,

we noted that the low energy peak observed in the positive ion spectra of several targets possibly originated from carbon, or other impurities, on the target surface. These probably originated from within the bulk of the target, rather than from the environment.

All flange seals past the bending magnet were made with gold rings, except those on the ion pump flanged manifolds, which were con-flats. The gold rings were sufficiently malleable to give vacuum tight seals at moderate bolt torque, and their performance was unaffected by baking the vacuum system to about 150^{o}C for several hours. Whenever it was necessary to bring the system up to atmospheric pressure, e.g., for changing the target, the system was kept filled with dry oxygen-free nitrogen gas, through a controlled leak until the completion of the operation. Over weekends and vacational periods, the target chamber section of the apparatus was isolated from the remainder of the system by closing the isolating valve. The latter was usually only opened during the actual course of experiments in order to minimize the seepage of diffusion pump oil vapout into the target chamber. These measures helped to maintain good, clean vacuum conditions and guaranteed reliable experimental results.

In addition to the problem of hydrogen contamination, if proper cleanliness criteria are not met, a metal surface will adsorb a certain amount of the residual gas. A metal surface has about 10^{15} lattice sites/cm^2. At 10^{-8} mm background pressure, each site is struck by bombarding residual gas atoms about once every 50 seconds. The adsorbed molecules, however, re-evaporate from the surface at a rate determined by the surface temperature and the heat of desorption, so that an equilibrium is established. The fraction of the surface covered at any instant is less than 10% if the condition

$$\frac{\Delta H}{kT} < 30 , \qquad \text{(A2)}$$

where ΔH is the heat of desorption and T is the absolute temperature.

Condition (A2) is easily satisfied for the bulk of the experimental data presented in this report, as the target is usually kept at red heat.

APENDIX II

ANGULAR MEASUREMENTS OF ELECTRON AND ION EMISSION

The experimental data presented in the main text of this report has been for fixed angles of incidence of the beam upon the surface (this being 45^{o} in Chapter II and 15^{o} in Chapters III and IV, the angles being measured from the normal to the target surface), or fixed angles of observation (90^{o} in Chapters III and IV). A supplementary series of experiments on angular distributions has just been concluded, as this report goes to press, and for completeness several results, which have some bearing upon the subject matter of the report, are briefly discussed. A paper is being prepared for publication which will describe the results of this program of experiments in much greater detail.

A. The Dependence of the Total Emission Coefficients, γ' and R, upon the Angle of Incidence

Figure A.6, an oscilloscope trace, shows the variation of γ' with the angle of incidence, for a 30 keV proton beam incident upon the 100 face of a monocrystalline Pt target. The value of the collector current (and hence γ' as the beam can be assumed to have remained constant over the few seconds taken to perform the experiment) is proportional to the vertical co-ordinate while the angle of incidence is proportional to the horizontal co-ordinate (1 cm $\equiv 14^{o}$). To achieve these conditions the oscilloscope sweep was applied externally by a signal proportional to ϕ, the angle of incidence. The signal was obtained by tapping off a d.c. voltage source with a potentiometer, a terminal of which rotated as the target was rotated about an axis normal to the incident beam. The signal to the collector surrounding the target was, of course, applied directly to the vertical plates of the oscilloscope.

The centre of the trace, where the emission is a minimum, is for normal incidence, i.e., $\phi = 0$. If we denote the emission at normal incidence by γ'_{o}, then to very good accuracy, we have:

$$\gamma' = \gamma'_o \sec \phi \ . \qquad \text{(A3)}$$

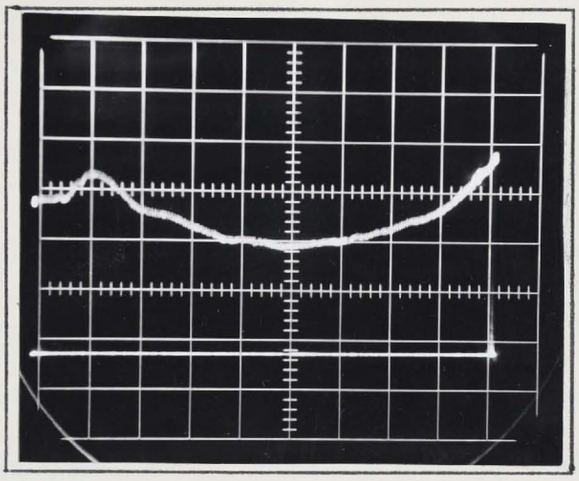

Figure A.6

A secant type variation would be expected as increasing the angle of incidence ϕ brings the incident ion path in the target closer to the surface of the target, so that the secondary electrons have a shorter path length to the surface, i.e., at a given depth, d, the ion path along which electrons are formed, is proportional to d sec ϕ (Figure 1.2, Chapter I). Thus the assumption made in Chapter III about the form of $\gamma - \phi$ variation was correct.

The asymmetry in the curve at about -56^{o} was probably due to the beam striking the edge of the crystal. The axis of rotation of the target may not have been precisely normal to the incident beam direction.

The minor fluctuations superimposed on the sec ϕ variation were a result of the phenomenon of channelling. This is a broad topic attracting considerable current interest from many researchers and it suffices to say here that channelling arises from the influence of the ordered arrangement of the metal atoms in a monocrystalline target upon the motion of the incident ions and upon their energy loss per unit penetration into the crystal. The maxima in the $\gamma(\phi)$ curve can be related to the directions along which the crystal lattice has the greatest transparency, i.e., those directions with the smallest values of the Miller indices.

Results for the variation of R with ϕ are shown in Figures A.7, A.8 and A.9. These are respectively for 30 keV, H^+, H_2^+ and H_3^+ ion bombardment of the 100 face of a Pt crystal. The main variation is of the form ,

$$a + b \sin \phi,$$

where a, b are constants, but with maxima and minima due to channelling superimposed upon it. The relative magnitude of the channelling is much greater than for electron emission. The central minimum occurs slightly off the centre of the trace as, in this case, the trace commenced a little to the left of the graduated scale. Measured from the central minimum, the ion scattering maxima occur at about $\pm 10^o$, $\pm 34^o$, $\pm 48^o$, and the minima at 0, $\pm 19^o$, $\pm 38^o$, $\pm 52^o$. The maxima and minima for the electron emission (Figure A.6) also occur at about these angles, although the fluctuations are too small for accurate determination.

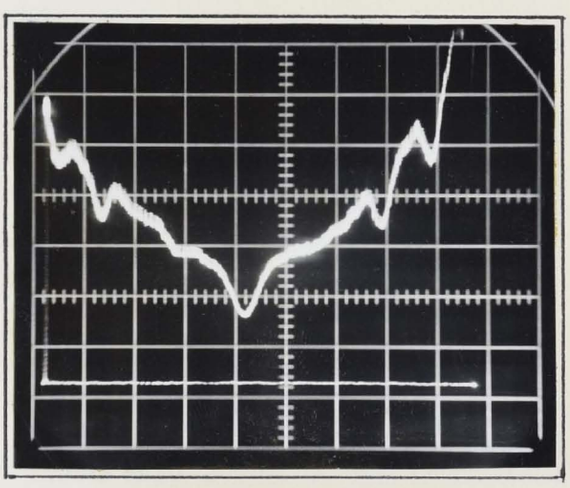

Figure A.7

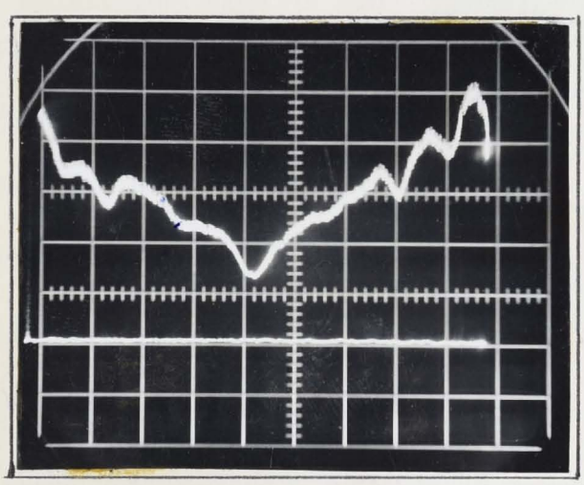

Figure A.8

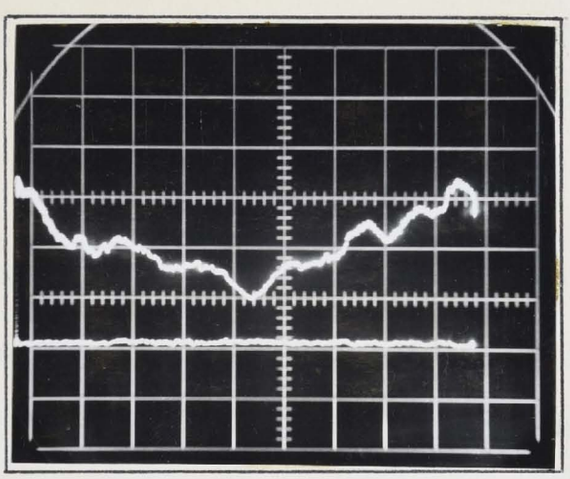

Figure A.9

Detailed interpretation of the traces will not be attempted here. However, electron diffraction showed that the <100> direction was actually 2^{o} off normal to the crystal surface and the axis of rotation of the crystal was inclined 14^{o} to the <010> direction on the crystal face. Clearly the traces show:

(i) The symmetry of a monocrystalline lattice structure relative to the major crystallographic directions (the <100> direction in this case).

(ii) The importance of channelling in the interpretation of all experimental data taken with monocrystalline targets.

Figure A.10 shows the R - ϕ variation for incident A^{+} ions upon the 100 face of a Pt monocrystal, for 10 keV incident beam energy. The channelling is not nearly as pronounced as for hydrogen ions, but maxima are apparent at $\pm 28^{o}$ and minima at 0^{o}, $\pm 35^{o}$. Figure A.11, for un-degassed target, shows only the monotonic variation and, indeed, channelling was only observed for properly degassed (clean) surfaces. The R - ϕ function for A^{+} ions is again of the $a_1 + b_1 \sin \phi$ form observed for hydrogen ions, and is similar for both degassed and un-degassed surfaces. (a_1, b_1 are the appropriate constants.) Some difference in the form of the R - ϕ might be expected in view of the difference in the penetration ranges of A^{+} and H^{+} ions at the same incident beam energy. Nielsen[5], for example, showed that the range decreases roughly as $Z_1^{-1} v$ for $\mu \gg 1$, where v is the incident particle energy. The much more pronounced effect of channelling for H^{+}, compared to A^{+} ions, is a manifestation of the much greater penetration of the former, along the channelling directions in this case.

B. Variation in the Shape of the Energy Distributions of Scattered Ions with the Angle of Incidence and the Angle of Scattering

In the following discussion θ and ϕ refer to the angle of scattering and the angle of incidence respectively. As detailed discussion will be given

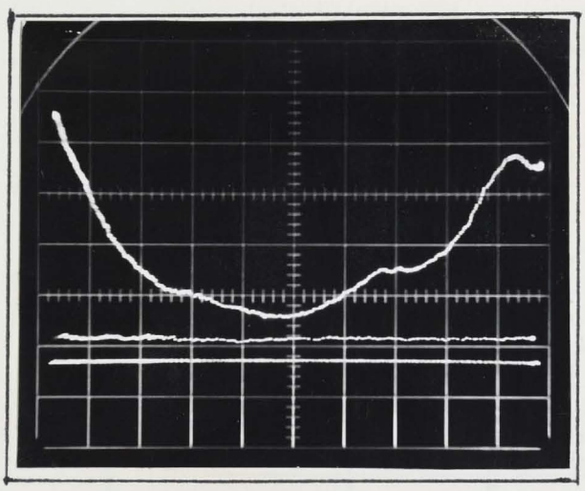

Figure A.10

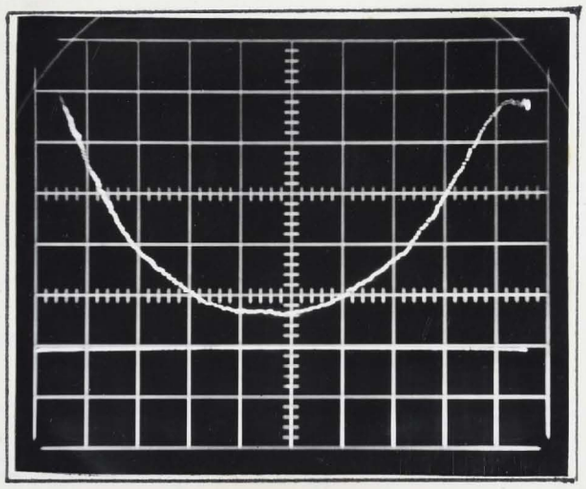

Figure A.11

in a paper being prepared for publication, only some representative data is presented here. The target is polycrystalline in all cases, unless otherwise specified.

Figure A.12 shows the variation in the shape of the spectra as θ is varied, keeping $\phi = 15^{o}$, and for an incident beam energy of 20.7 keV. From equation (1.34), Chapter I, it is clear that the broadening of the spectra with increasing θ is a consequence of increasing penetration depth. The broadening is accompanied by a steady shift in the positions of the peaks towards lower increases as θ increases. The results for incident N^{+} ions, shown in Figure A.13, are similar to those for H^{+}, although not as pronounced.

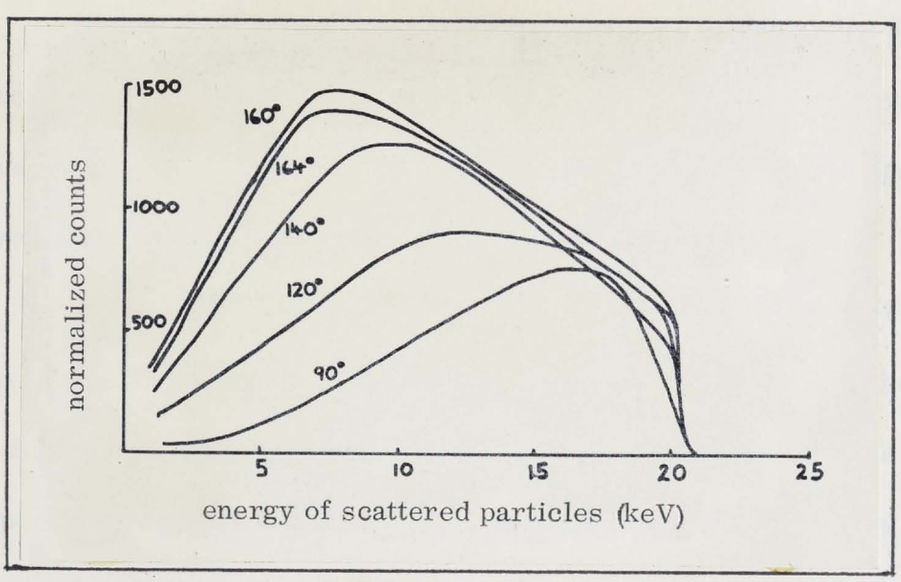

Figure A.12

Variation in shape of spectra as θ is varied, for $\phi = 15^{o}$. Incident protons at 20.7 keV.

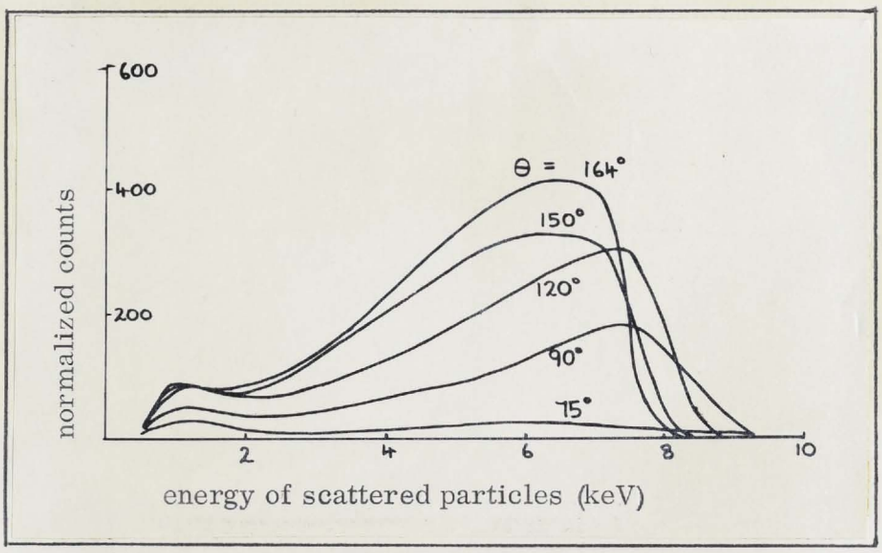

Figure A.13

Variation in shape of spectra as θ is varied, for $\phi = 15^{o}$. Incident N^{+} ions at 10.9 keV.

The fact that the change in shape of the energy spectra is a consequence of changing penetration depth, i.e., of the inelastic energy losses in the target, especially for hydrogen ions, as calculated from equation (1.34) substantiates the general discussion given in Chapters I and IV. For $\theta = 90^{o}$ and $\phi = 15^{o}$ (the conditions employed in Chapter IV) equation (1.34) and the corresponding energy spectrum in Figure A.12 give a penetration depth of about 10^{-7} cm, for 10 keV protons.

Figure A.14 shows how the energy spectra broaden as the angle of incidence increases, again as a consequence of increasing mean penetration depth (equation (1.34)). However, the effect (broadening and shift of the peak) is not as pronounced as when the angle of scattering is varied.

Figure A.15 shows some angular distributions of scattered protons from the platinum target. They are modified cosine in form. On the other hand, our deductions and discussion in Chapters I and IV indicated that the distributions for particles scattered without charge are approximately Rutherford in form. Measurements on angular distributions of scattered atoms are clearly required to clarify this matter.

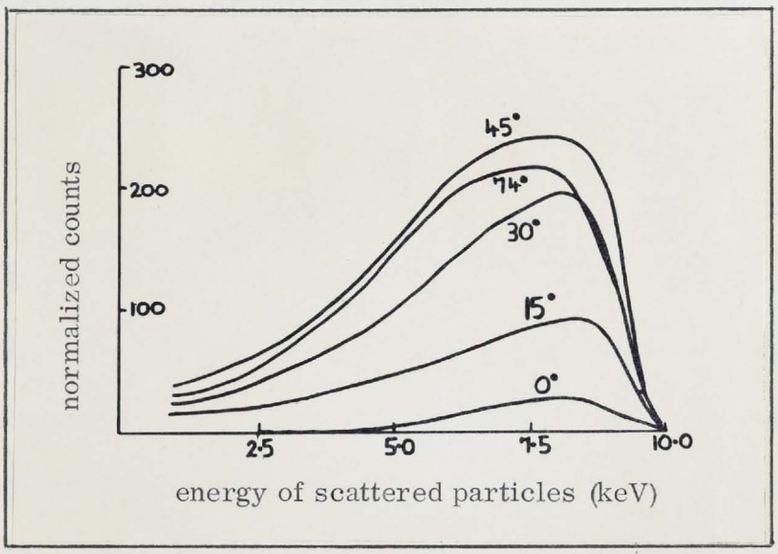

Figure A.14

Variation in shape of spectra as ϕ is varied, for $\theta = 90^{o}$. Incident protons at 9.9 keV.

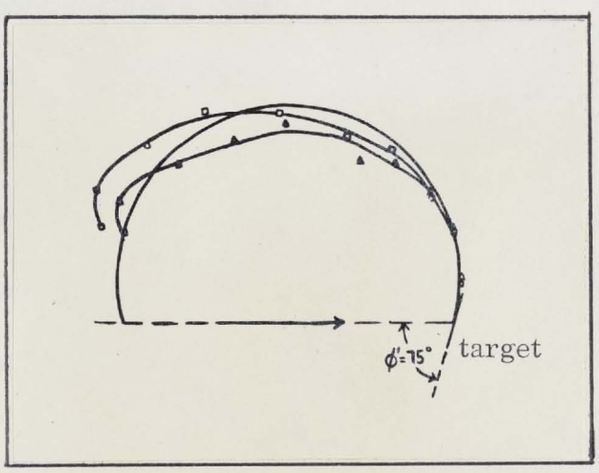

Figure A.15

Angular distributions of scattered protons from the platinum target.

—— cosine

□ H^{+}, 10.1 keV.

△ H^{+}, 20.7 keV.

The N^{+} spectra, Figure A.13, contain a low energy peak, although this was absent from the spectra presented in Chapter IV. This would seem to suggest that the low energy peak is correlated with the target surface conditions as, for the present results, the target was indirectly heated using a tungsten filament and some carbon from the latter may have been inadvertently evaporated onto the target. The presence of some contamination is also evidenced

by the rather broad N^+ spectra and by the failure of the peaks to fall exactly at the values predicted for bi-particle collisions. On the other hand, the failure to detect any ions at very low energies, or at "half energy" (Chapter IV) indicates that the contamination was probably insufficient to appreciably affect the angular distributions.

Figures A.16 to A.19 indicate some results obtained from the 100 face of a platinum monocrystal. They are included here for completeness and detailed discussion is not attempted. One notes, however, that:

(i) The energy spectra of scattered protons all contain pronounced fluctuations imposed upon a general variation which peaks at about 5 keV scattered ion energy in all cases. The mean energies of scattered particles are clearly much less than for a polycrystalline target.

(ii) The shapes of the energy spectra have a very complicated dependence upon the angles θ, ϕ. As one of these is kept fixed and the other one is varied, the proportion of high energy scattered ions in the spectra changes sharply. The latter is a minimum along the orientations of maximum channelling.

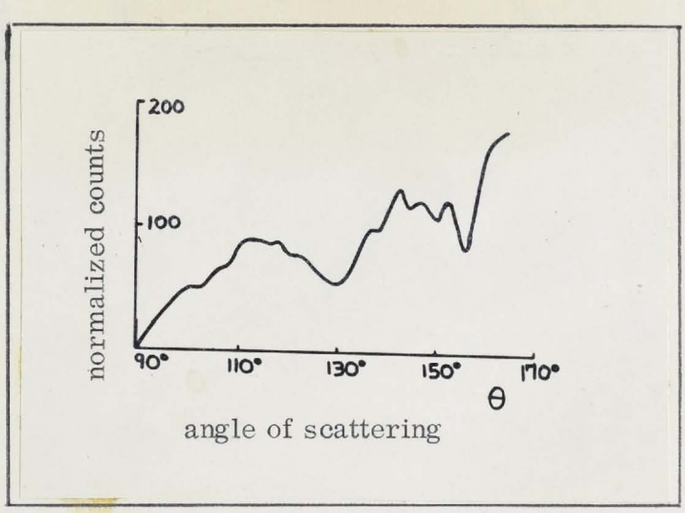

Figure A.16

Number of particles scattered from 100 face of Pt with 15 keV energy as a function of θ, for $\phi = 90^{\circ}$. Incident protons at 20 keV.

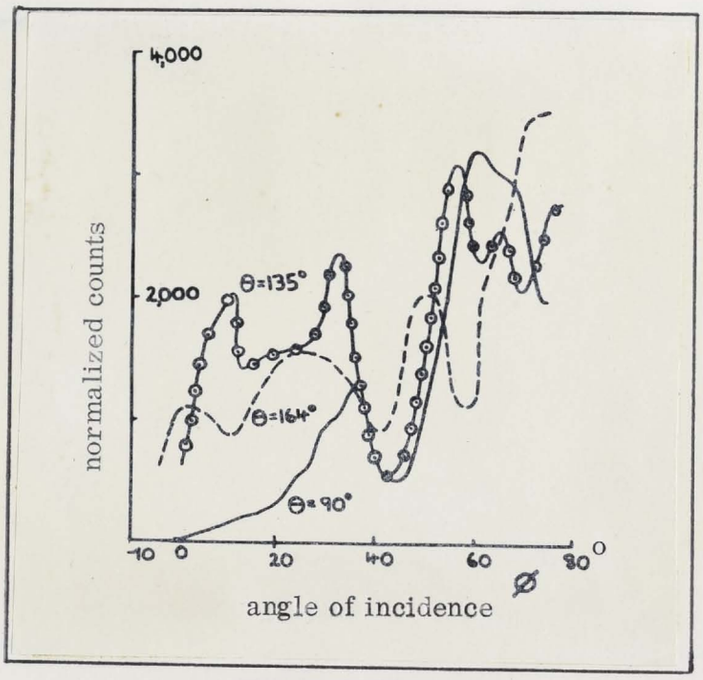

Figure A.17

Number of particles scattered from 100 face of Pt with 15 keV energy for various values of θ, as a function of ϕ. Incident protons at 20 keV.

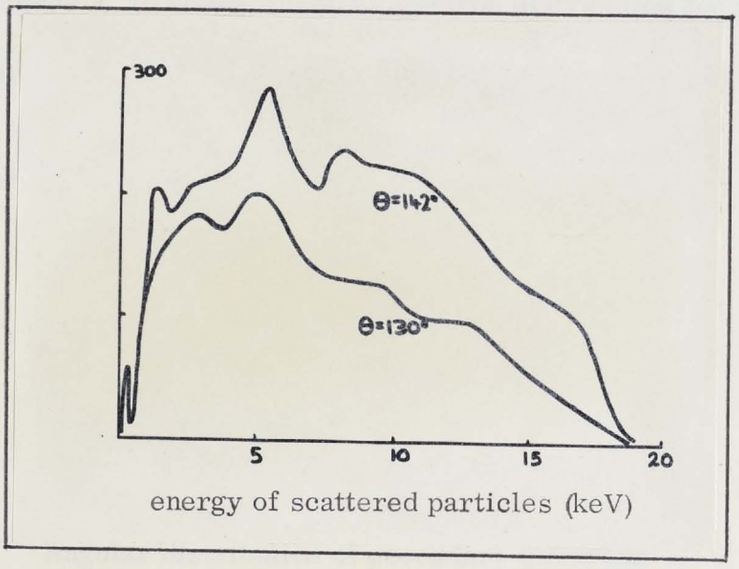

Figure A.18

Energy spectra at selected values of θ for $\phi = 90^{\circ}$. Protons on the 100 face of Pt at 19.5 keV.

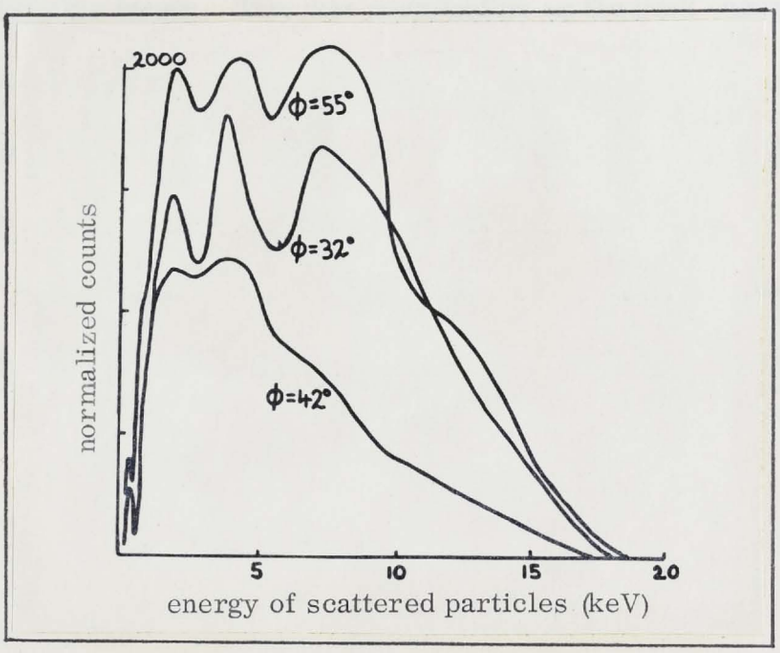

Figure A.19

Energy spectra at selected values of the angle of indicence for $\theta = 45^{o}$. Protons on the 100 face of Pt at 20 keV.

C. The Angular Distributions of Secondary Electrons

Figure A.20 shows a typical electron distribution for H^{+} incident upon polycrystalline Pt at 20 keV. The angle of incidence was 45^{o} in this case.

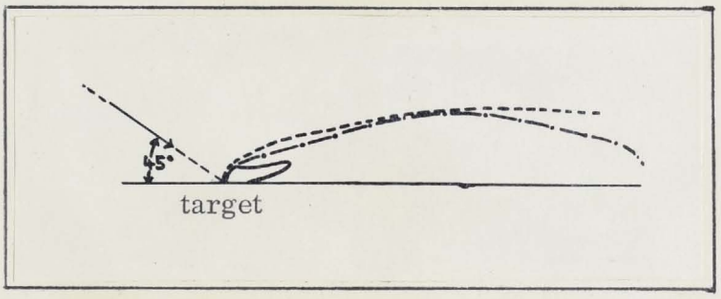

Figure A.20

Angular distribution of secondary electrons for protons on polycrystalline Pt at 20 keV incident energy.

—— measured distribution

---- $\text{cosec}^{4}\ \phi/2$ distribution

-·-·- measured distribution corrected for cosine effect.

Again detailed discussion is not attempted here, but one sees that the distribution is far from uniform and has a strong forward component. The distribution was taken by setting the electrostatic (127^{o}) analyser voltage to the peak of the energy distribution and then changing θ, the analyser position

relative to the target. This was permissible as the peak energy of the energy distributions and the shapes of the energy distributions of the secondary electrons did not change appreciably with θ. The distribution in Figure A.20 thus contains no contribution from scattered negative ions.

As the shape of the electron energy distributions is the same as obtained in Chapter III, using a 180^{o} spherical analyser, none is reproduced here.

APPENDIX III

CALIBRATION FACTOR OF SPHERICAL ANALYSER EMPLOYED IN CHAPTERS III AND IV

Referring to Figure 3.1, Chapter III, let q be the charge on the inner hemisphere, radius a. Then the charge on the outer hemisphere, radius b, must also be q for a steady field between the hemispheres.

The potentials on the hemispheres are (taking $V_\infty = 0$)

$$V_a = \frac{q}{a} , \tag{1}$$

$$V_b = \frac{q}{b} . \tag{2}$$

The potential difference between the hemispheres is:

$$V_o = V_a - B_b$$

$$= \frac{q}{a} - \frac{q}{b}$$

$$= q \frac{(b - a)}{ab} . \tag{3}$$

Consider a particle of charge e moving in a circular path, radius c, between the hemispheres. Then it follows a path along which the voltage is:

$$V_c = \frac{q}{c} ,$$

and the field is

$$E_c = \frac{q}{c^2} . \tag{4}$$

But if the particle has energy V in electron volts, then

$$\frac{2eV}{c} = E_c e , \tag{5}$$

and so from (4) and (5)

$$q = 2V.c . \tag{6}$$

Hence (3) becomes:

$$V_o = V \times \frac{2c(b - a)}{ab} . \tag{7}$$

Substituting the values a = 1.750" = 4.445 cm, b = 2.125" = 5.398 cm and c = 1.933" = 4.909 cm into (7), gives:

$$V_o = 0.3907 \text{ V}$$

or,

$$V = 2.56\, V_o . \qquad (8)$$

Thus the particle energy in electron volts is obtained by multiplying the potential differences between the hemispheres by 2.56.

REFERENCES

(Note: All Russian references refer to the English translation)

(1) N. Bohr - Mat. Fys. Medd. Dan. Vid. Selsk, 18, 8 (1948).

(2) F. Seitz - Disc. Farad. Soc., 5, 271 (1949).

(3) J. Lindhard - Dan. Vid. Selsk. Mat. Fys. Medd., 28, 8 (1954);
J. Lindhard and M. Scharff - Dan. Vid. Selsk. Mat. Fys. Medd., 27, 15 (1953);
J. Lindhard and A. Winther - Dan. Vid. Selsk. Mat. Fys. Medd., 34, 3 (1964);
J. Lindhard and M. Scharff - Phys. Rev., 124, 128 (1960).

(4) H. Gombas - Handbuch der Physik, 36. Springer-Verlag.

(5) K. Nielsen - "Electromagnetically Enriched Isotopes and Mass Spectrometry, p. 63. Butterworths, London (1956).

(6) E. Datz - Methods of Experimental Physics, 7B (1968).

(7) H.A. Bethe - Ann. Physik, 5, 325 (1930).

(8) G.M. McCracken and N.J. Freeman - U.K.A.E.A. Preprint CLM, p.195 (1969).

(9) E.S. Mashkova et al. - Soviet Physics-Doklady, 13, 663 (1969).

(10) K. Morita, H. Akimune, T. Suita - Proc. Phys. Soc. Jap., in preparation.

(11) K. Morita, H. Akimune, T. Suita - Jap. Jn. Appl. Phys., 7, 916 (1968).

(12) See reference (8) and also: G.M. McCracken and N.J. Freeman - Physics Letters, 28, 415 (1969).

(13) R. Behrisch - Canad. Jn. Phys., 46, 527 (1968).

(14) J.A. Weinman and J.R. Cameron - Rev. Sci. Instr., 27, 288 (1956).

(15) O.B. Firsov - Soviet Physics - J.E.T.P., 9, 1076 (1959);
A. Russek and M.T. Thomas - Phys. Rev., 109, 2015 (1958);
A. Russek and M.T. Thomas - Phys. Rev., 114, 1538 (1959);
J.B. Bulman and A. Russek - Phys. Rev., 122, 506 (1961);
A. Russek - Phys. Rev., 132, 246 (1963).

(16) G. Morgan and E. Everhart - Phys. Rev., 128, 667 (1962).

(17a) C. Snoek and J. Kistemaker - Advances in Electronics and Electron Physics, 21 (1965).

(17) M.W. Thompson and R.S. Nelson - Proc. Roy. Soc., A 259, 458 (1961);

M.W. Thompson and R.S. Nelson - Phil. Mag., 7, 2015 (1962).

(18) R.C. Bradley, A. Arking and D.S. Beers - J. Chem. Phys., 33, 764 (1960).

(19) Y.M. Fogel - Soviet Physics - Uspekhi, 10, 17 (1967).

(20) O.C. Yonts et al. - Jn. Appl. Phys., 31, 447 (1960);

O. Almen et al. - Nucl. Instr. and Methods, 11, 257 (1961);

P. Rol et al. - "Electromagnetic Separation of Radioactive Isotopes", Springer-Verlag;

M. Guseva - Soviet Physics - Solid State, 1, 1410 (1959).

(21) N. Laegrend and G.K. Wehner - J. Appl. Phys., 32, 365 (1961);

D. Rosenberg and G.K. Wehner - J. Appl. Phys., 33, 1842 (1962).

(22) E.S. Parilis and L.M. Kishinevski - Soviet Physics - Solid State, 3, 885 (1960).

(23) E.S. Parilis and L.M. Kishinevski - Soviet Physics - Bull. Acad. Sci. (U.S.S.R.), 26, 1422 (1963).

(24) S.V. Izmailov - Soviet Physics - Solid State, 1, 1415 (1960);

S.V. Izmailov - Soviet Physics - Solid State, 1, 1425 (1960);

S.V. Izmailov - Soviet Physics - Solid State, 3, 2046 (1962).

(25) O. Von Roos - Z. Physik, 147, 210 (1957).

(26) E.J. Sternglass - Phys. Rev., 108, 1 (1957).

(27) S.N. Ghosh and S.P. Khare - Phys. Rev., 125, 1254 (1962);

S.N. Ghosh and S.P. Khare - Phys. Rev., 129, 1638 (1963).

(28) U.A. Arifov - "Interaction of Atomic Particles with the Surface of a Metal". Atomic Energy Commission (Washington, D.C.) Transl. No. AEC-tr-6089 (1963).

(29) H.D. Hagstrum - Phys. Rev., 104, 317 (1955);

H.D. Hagstrum - Phys. Rev., 104, 672 (1956).

(30) A. Van Wijngaarden et al. - Canad. Jn. Phys., 47, 411 (1969).

(31) R.C. Abbott and H.W. Berry - Jn. Appl. Phys., 30, 871 (1959).

(32) M. Kaminsky and G. Goodwin - 25th Annual Conference on Physical Electronics, M.I.T., p.213 (1965).

(33) M.W. Thompson - Phil. Mag., 18, 377 (1968).

(34) B.V. Panin - Soviet Physics - J.E.T.P., 15, 215 (1962).

(35) P.H. Rose - Nucl. Instr. and Methods, 11, 49 (1961).

(36) D.P. Smith - Jn. Appl. Phys., 38, 340 (1967).

(37) E.R. Cawthron, D.L. Cotterell and M.L. Oliphant - Proc. Roy. Soc., to be published.

(38) C. Brunnee - Z. Phys., 147, 161 (1957).

(39) V.I. Veksler - Soviet Physics - J.E.T.P., 11, 235 (1960).

(40) V.J. Kowalewski et al. - Nucl. Instr. and Methods, 5, 90 (1959); H.P. Eubank - Rev. Sci. Instr., 25, 10 (1954).

(41) N.N. Petrov - Soviet Physics - Technical Physics, 31, 249 (1961).

(42) E. Enge - Rev. Sci. Instr., 32, 662 (1960).